Study of Σ-Nucleus Potential by the (π^-, K^+) reaction

Pranab Kumar Saha

Doctor of Philosophy

Abstract

In order to study the Σ-nucleus potential, we carried out an experiment at the K6 beam line of the 12-GeV proton synchrotron in High Energy Accelerator Research Organization(KEK) using the superconducting kaon spectrometer(SKS) system. In the present experiment, for the first time we measured inclusive (π^-, K^+) spectra on CH_2, Si, Ni, In and Bi targets with reasonable statistics covering a wider excitation energy region. We extracted the information on the Σ-nucleus optical potential from the analysis of the spectral shape. The CH_2 target was used to calibrate the excitation energy scale(horizontal axis) from the elementary process, $p(\pi^-, K^+)\Sigma^-$. The C spectrum was also able to be extracted from the CH_2 target. The SKS, which has a wider momentum acceptance and good energy resolution was helpful to obtain a good statistics data keeping a good energy resolution. The calibration of the energy scale was done successfully with a precision of ± 0.1 MeV. The angular distribution of the elementary cross section was found to be consistent with the previous bubble chamber data. All the inclusive spectra were found to be very identical in shape from the Σ^- binding energy threshold to around 90 MeV excited regions. The mass number dependence of the cross section was obtained from the ratio of the cross section. Compared to the eikonal approximation, present experimental data showed a rather weak mass number dependence. A Monte Carlo simulation was done for the quasi-free Si spectrum where no final state interaction of Σ^- to the residual nucleus was considered. The simulated spectrum could not reproduce the observed spectral shape. The strength of the observed spectrum was found to be much suppressed, particularly, near the binding energy threshold. We compared the observed Si spectral shape to the theoretical spectra calculated by using two types of phenomenological potential in the framework of DWIA. One is based on the one boson exchange potential(OBEP) describing the two-body YN interaction, which represents an attractive Σ-nucleus potential, and the other one is obtained from the Σ^--atomic X-ray data, which represents a repulsive Σ-nucleus potential. None of the potential could reproduce the observed spectral shape. In particular, the peak position of the observed spectrum was found to be much shifted towards the higher excitation energy from both of the calculated spectra. Energy dependence of the elementary cross section was found to be very sensitive to the spectral shape. Taking into account this effect, another DWIA calculation was done for Si. The spectral shape was found to be significantly changed from that of the previous calculation by using the same Σ-nucleus potential in both calculation, but still different from the observed one. Then a detail analysis was done to reproduce the observed spectral shape using Woods-Saxon type potentials. A strong repulsive potential of which depth of the real part(V_Σ) > 90 MeV with a moderately absorptive imaginary part(W_Σ) was favorable in reproducing the observed spectral shape.

Contents

List of Figures

iv

List of Tables

Chapter 1

Introduction

1.1 Nucleus to Hypernucleus

A nucleus is a central core of an atom that contains most of its mass, positively charged and consists of one or more nucleons (protons or neutrons), where a hypernucleus is the implant of a different type of baryon(s) (Λ, Σ, Ξ, $\Lambda\Lambda$) into an ordinary nucleus. Upto now about 35 hypernuclear species of single strangeness system (S=-1) together with double strangeness system (S=-2) have been discovered.

So far the nucleon-nucleon (NN) interaction has been studied extensively and many phenomenological NN potentials based on the one-boson-exchange (OBE) mechanism describe successfully the NN force in the middle to long range. However, the short range repulsive force (hard-core) could not be explained by those models which was revealed from the phase shift analyses. It was then thought to be understood in terms of the quark picture. The origin of hard-core was visualized by the quark cluster model(QCM) as occurring by the one-gluon-exchange mechanism between quarks. It has been revealed that quarks play an important role in the short range region of the NN interaction in contrast with the role of the one-boson-exchange in the middle to long range.

A hypernucleus is a good tool to investigate the two-body YN interaction for a unified understanding of the general baryon-baryon interaction (i.e. nuclear force) in terms of meson exchange forces and, ultimately in terms of the quark picture. Many theoretical works have been done recently to extend the knowledge of the nuclear force into other constituents of the baryon octet introducing a hyperon to it. One of the main goal of these studies is to construct a unified model which describes the interaction between the constituents of the baryon octet at low energy. Experimentally, one way is to study the baryon-baryon scattering. But, mainly due to hyperon's short life time it is hard to accumulate hyperon scattering data in the same level of NN data both in quality and quantity. Therefore, studies of hypernuclei are vital to investigate the baryon-baryon interaction in extended flavor space.

1.2 Physics Motivation

The history of hypernucleus study started with the investigation of the Λ hypernucleus after its discovery nearly fifty years ago. As a result, our understanding about Λ hypernucleus spectroscopy is relatively in advanced stage. For example, high resolution magnetic spectrometer system and/or a germanium gamma-ray detector array made it possible to resolve the state split by the ΛN spin dependent interaction, such as the spin-orbit and spin-spin forces [1, 2, 3]. The (π^+, K^+) spectra reflecting the Λ major shell structures even in heavy nuclear systems like, $^{89}_{\Lambda}$Y or $^{208}_{\Lambda}$Pb are observed clearly (figure 1.1). As a result, the binding energies of Λ hypernuclei can be well reproduced by a simple Woods-Saxon type single particle potential of which depth is 28 MeV [4].

On the other hand, our knowledge about Σ-nucleus potential is very limited both in quantity and quality. For example, only qualitatively we know that the real part of the potential seems shallow and the imaginary part seems absorptive. However, we do not know the real part is attractive or repulsive and even the finite value of the imaginary part. The main cause is due to insufficient (and rather poor) experimental data, as mentioned in details in the next section. ΣN interaction is closely related to ΛN interaction through mixing as the Σ's mass differs only about 80 MeV from Λ's. Recently, a role of strangeness in a high density matter of neutron star is being intensively discussed. The presence of hyperons such as Λ or Σ and also K^- play a significant role by softening the nuclear equation of state at high density (figure 1.2, [5]). Abundance of hyperons in a neutron star is thus very important in determining the maximum mass and radius of neutron stars. In addition, they also play a significant role in understanding a formation-scenario and a thermal and structural evolution-scenario of neutron stars [6]. Particularly, the interaction of Σ^- is interesting since Σ^- is a hyperon expected to appear first in dense nuclear matter due to it's formation mechanism.

In order to reveal the Σ-nucleus potential, new experimental information has been desired. We therefore carried out an experiment, KEK-PS E438, 'Study of Σ-nucleus potential by the (π^-, K^+) reaction in heavy nuclei' where we measured the inclusive (π^-, K^+) spectra with reasonably high statistics on medium to heavy nuclear targets.

2
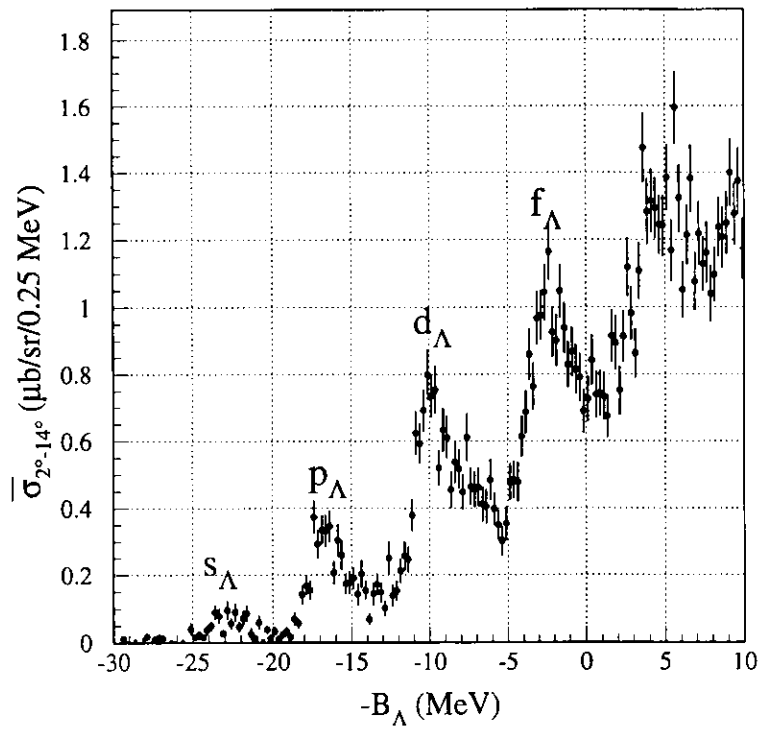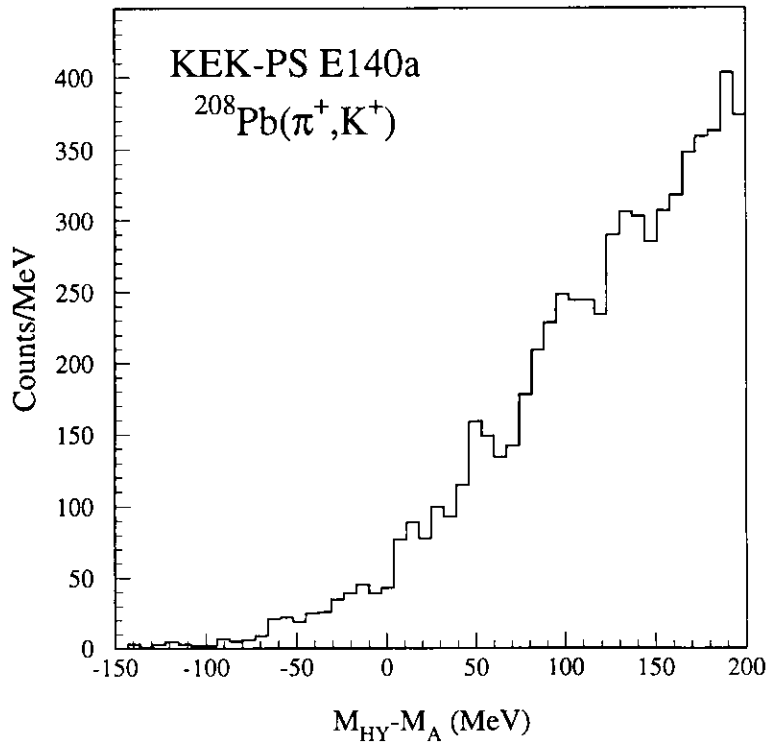
Figure 1.1:Λ-major shell structures from low-lying upto highly-excited states observed even in heavy nuclear systems like, $_\Lambda^{208}$Pb(up) or $_\Lambda^{89}$Y(down) in KEK [1, 2].
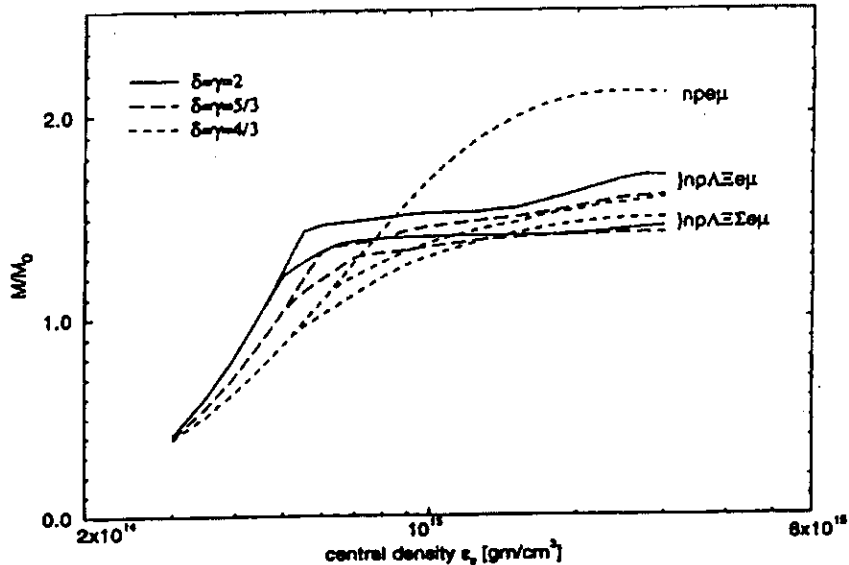
Figure 1.2: Neutron stars mass vs. central density mass-sequences for high density matter with all hyperon species and with only Λ's and Ξ's but no Σ's (for a repulsive Σ-nm interaction). See Ref.[5] in details.

1.3 Historical Background

Study of Σ-hypernucleus started around late 1970's which was a bit late compared to Λ-hypernuclei study and after a long investigation of the later one. At that time a series of Λ-hypernuclear experiments [7, 8, 9] using in-flight (K^-, π^-) strangeness exchange reaction gave details of the Λ-nucleus interactions which led to a deeper understanding of the Λ single-particle properties inside the nuclear medium. However, the spin-orbit splitting was found very small comparing the observed $^{12}_{\Lambda}C$ and $^{16}_{\Lambda}O$ spectra in contrast to that of normal nuclei [7]. So the much attention was then paid for the spin-orbit splitting in a Σ-hypernucleus where the Σ-nucleus interaction was discussed mainly by using some Σ-N scattering data obtained in old bubble chamber experiments, although they were very limited in accuracy as well as in statistical quality compared to the very precise data on NN system. Moreover, the measured energy range were also very limited (figure 1.3). The short life time of Σ's made it difficult to have high intensity Σ beams at low energy. So the measurements on spin-dependent forces were almost impossible.

On the other hand it was also quite natural to attempt the Σ hypernuclear spectroscopy by the same (K^-, π^-) reaction as it was quite successful in Λ hyper-

4
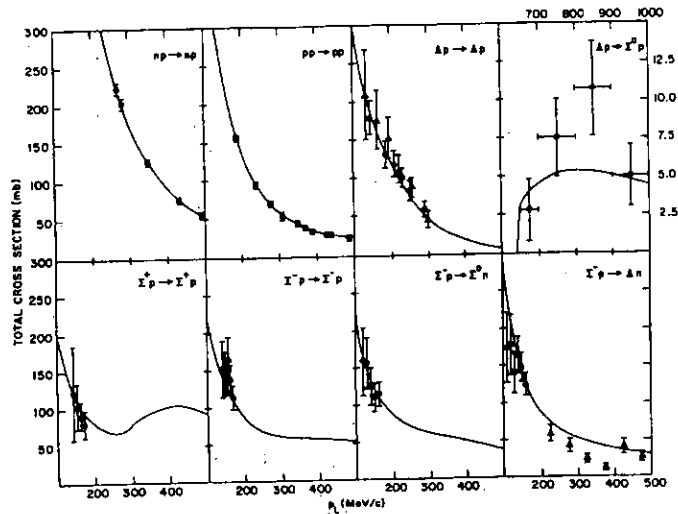
Figure 1.3: Total cross sections for baryon-baryon scattering and reactions as a function of incident lab. momentum [10].

nuclei. The first report came out by Saclay-Heidelberg Collaboration claiming the possible existence of narrow Σ hypernuclear states by the (K^-, π^-) reaction on ^{9}Be target using incident kaon momentum of 720 MeV/c (figure 1.4, [11]). They claimed two narrow peaks($\Gamma < 8MeV$) above the Σ binding threshold. Similar claim was also reported 2 years later in $^6_\Sigma$H hypernucleus [12] and again in 1984 about $^{12}_\Sigma$C and $^{12}_\Sigma$Be by Saclay-Heidelberg Collaboration [13]. Both cases peak widths were much narrower ($\Gamma < 5MeV$) than the first observation. It generated much theoretical and experimental excitement as it was quite unexpected as well as difficult to explain such narrow excitations since width of Σ in nuclei was believed to be much broader (about 25 MeV) [14].

Many theoretical models were later proposed in order to extensively explain the existence of those narrow Σ hypernuclear states by a combined effect of Pauli suppression and the spin-isospin selectivity of the $\Sigma N \rightarrow \Lambda N$ process [15, 16]. However, the Pauli Blocking effect was shown playing only a moderate role in reducing Σ widths but the major contribution was shown due to the polarization of the medium by the spin-isospin interactions for the $\Sigma N \rightarrow \Lambda N$ transition [17]. Later at BNL at attempt was made to solve this problem searching for the Σ hypernuclear states both above and below the Σ emission threshold using the in-flight $(K^-, \pi^\pm)$ reaction on different light nuclear targets like ^{1}H, ^{2}H, ^{6}Li and ^{9}Be with high statistics [18]. Direct comparison of both $(K^-, \pi^\pm)$ spectra on ^{9}Be with the previously reported one [11] showed no such kinds of narrow peak either below or above the Σ^+ or the Σ^- production threshold (figure 1.5). Spectra on other targets also did not indicate any such kinds of structure. But, those experiments gave no information to put forth on the $\Sigma - N$ and/or Σ-nucleus potential. As a result, the sign of V_Σ cannot be determined reliably as well as the size of the well depth for neither V_Σ nor W_Σ is known accurately.

5
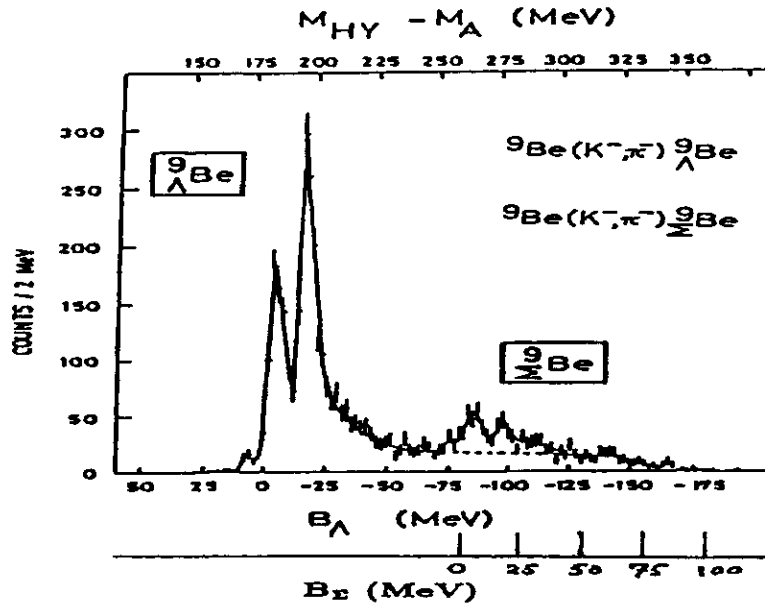
Figure 1.4: Narrow Σ hypernuclear states observed together with Λ hypernuclear spectra from the (K^-, π^-) reaction on ^{9}Be at a kaon momentum of 720 MeV/c. The spectrum is plotted as a function of the transformation energy $M_{HY} - M_A$. Λ and Σ binding energy scale, B_Λ and B_Σ, respectively, are also shown for comparison [11].
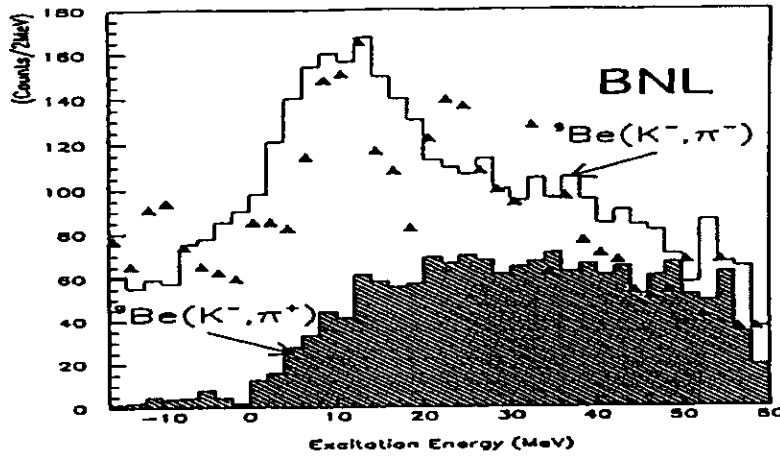
Figure 1.5:(K^-, π^-) and the (K^-, π^+) (shaded) hypernuclear mass spectra on ^{9}Be with high statistics measured at BNL [18]. The triangles are the previously reported data on ^{9}Be(K^-, π^-) at CERN (figure 1.4, [11]) shown for comparison.

6

Another source of the information on the Σ-nucleus potential was the Σ^--atomic X-ray data [19, 20, 21] where the strong interaction effects had been observed in the X-ray spectra of atoms formed with Σ^- hyperon over a wider mass number region across the periodic table. When an exotic atom is formed by capturing Σ^- hyperon into an atomic orbit around a nucleus, the X-rays emitted by the way of Σ^- cascades down towards the atomic ground state. Due to the strong interaction between Σ^- and the nucleus, the energy and the widths of the atomic states differ from those calculated with electromagnetic interaction only (figure 1.6). A naive analysis based on a Σ-nucleus optical potential linear to the nuclear density to fit the energy shifts, widths and yields of the Σ^- atomic levels suggested an attractive ($V_\Sigma < 0$) and absorptive ($W_\Sigma < 0$), and its central depth was given approximately by $-(25 \sim 30)$ MeV and $-(10 \sim 15)$ MeV, respectively (label Batty in figure 1.7, [22]). Later, the same authors reported a strongly repulsive V_Σ and strongly absorptive W_Σ by taking the iso-vector term into account (label Batty DD in figure 1.7.)
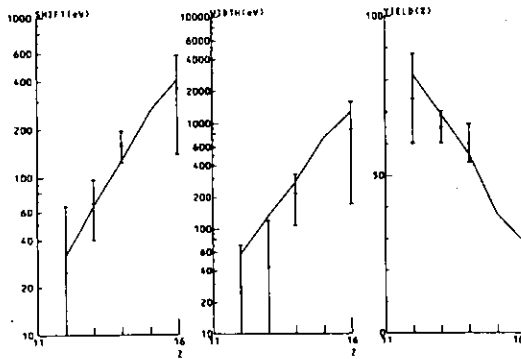
Figure 1.6:Example of energy shifts, widths and yields for Mg, Al, Si and S in a measurement of Σ^--atom X-rays [20]. The lines show the calculated values obtained using the scattering length $0.35 \pm i\, 0.19$ fm.
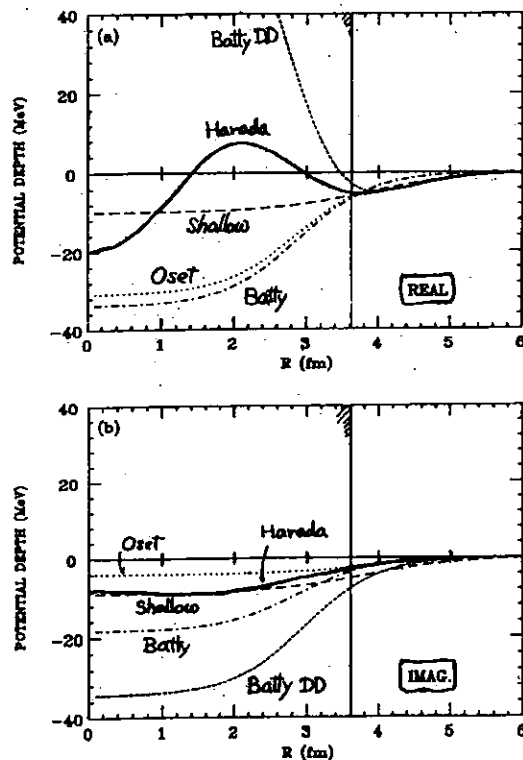
Figure 1.7:
Various Σ^--nucleus potential calculated for ^{28}Si [23]. Above is the real part of the potential and below, the imaginary part.

Figure 1.7 shows the calculated several types of Σ single-particle potential for the $\Sigma - {}^{28}$Si system from the Σ^--atomic X-ray data by several authors. The folding potential based on the YN one boson exchange potential(OBEP) is also shown together [23]. Clearly seen in the figure that atomic data are sensitive only to the tail region of the potential. As a result, various shapes of the potential in the nuclear-central region were obtained.

Another calculation of Σ-nucleus potential was also made by Yamada and Yamamoto by a combined analysis of Σ^- atomic data and ${}^4_\Sigma$He hypernucleus where the density dependent effective YN interaction was calculated and folded with finite nucleus in the local density approximation [24]. Their calculation is shown in the figure 1.8. So whether the real part of the Σ-nucleus potential is strongly repulsive or weekly attractive is still an open question.
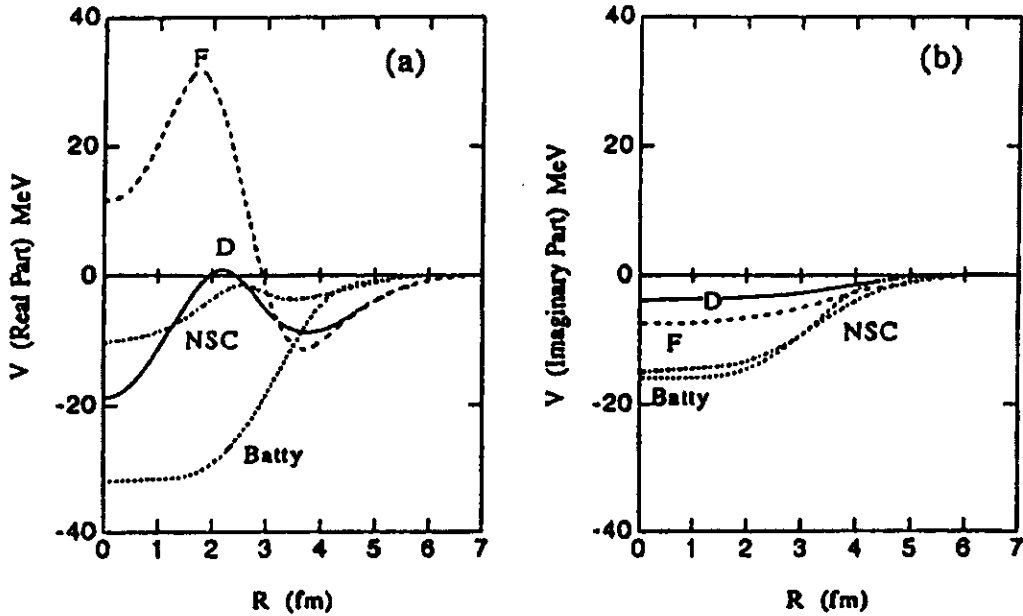
Figure 1.8: Calculated Σ^--^{28}Si potential by Yamada and Yamamoto [24]. D, F and NSC represent Nijmengen OBEP Model-D, F and the Soft Core based potential, respectively. Calculated potential from the Σ^--atomic X-ray data by Batty is shown for comparison.

On the other hand, the observation of ${}^4_\Sigma$He bound state by the in-flight (K^-, π^-) reaction at BNL (figure 1.9, [25]) was one of the great success confirming of any bound state of hypernuclei containing Σ hyperon which was first claimed in KEK using $(K^-_{stopped}, \pi^+)$ reaction [26]. This makes us expect to open the spectroscopy of Σ hypernuclei that can contribute to the study of ΣN effective interaction. Existence of this bound state in ^{4}He was also predicted in theory by Harada et al. in 1990 [27]. According to their theory, a strong isospin-dependence of the ΣN

8

interaction plays an important role in populating rather a narrow bound state.
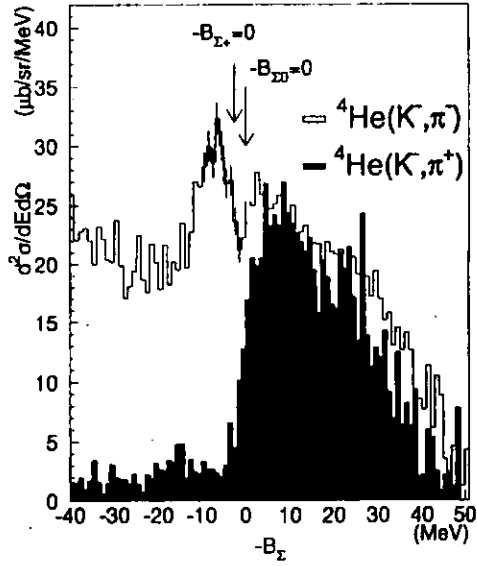
Figure 1.9: Excitation energy spectra of ^{4}He(K^-, π^+) and ^{4}He(K^-, π^-) at P_K = 600 MeV/c and θ_K = 4° [25].
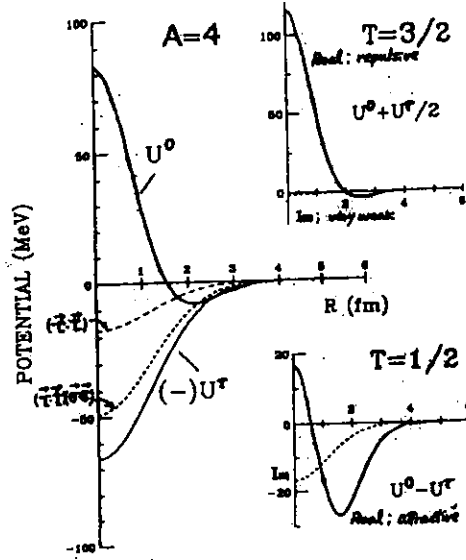
Figure 1.10:Σ-nucleus potential for A = 4 system [23, 27] .

The calculative potential is shown in figure 1.10 and is generally expressed as

$$U = U_0 + U_\tau \cdot \frac{(\sigma_\Sigma \cdot \mathbf{T_t})}{A}.$$

(1.1)

where A is the mass number. The first term, U_0 is an isospin independent part and the second term is isospin dependent, so-called Lane term. In the case of ^{4}He(K^-, π^-) reaction, both T = 1/2 and T = 3/2 states can be populated. T = 1/2 state is attractive while the T = 3/2 state is strongly repulsive. So for T = 1/2$state$, $U = U_0 - U_\tau$ and for T = 3/2 state, $U = U_0 + \frac{1}{2}U_\tau$. As a result of the cancellation between U_0 and U_τ in T = 1/2, the potential has a weak attractive pocket near the core nucleus surface, which suppresses the conversion width for the bound state. While, no bound state was expected for the ^{4}He(K^-, π^+) reaction which populates only T = 3/2 state as also in the experimental observation. The only observation of bound state Σ-hypernucleus mentioned above may be very special in light nuclear system but still we do not know the Σ single-particle potential. Thus the new data on heavy nuclear system is necessary where U_0 term in equation 1.1 becomes dominant and the Lane term becomes recessive.

Nevertheless, many other attempts were made experimentally by that time using (K^-, $\pi^\pm$) or ($K^-_{stopped}$, π^-) reactions in light nuclear systems ($A \leq 16$).

9

Unfortunately, almost all of them did not succeed to observe any narrow bound Σ hypernuclear state for those systems. However, an analysis made with the inclusive $(K^-_{stopped}, \pi^+)$ spectrum on ^{12}C was quite suggestive to investigate the Σ-nucleus potential. Namely, ^{12}C$(K^-_{stopped}, \pi^+)$ spectrum measured in KEK gave a limitation to the Σ-nucleus optical potential, which was, the real part, U_Σ(in their notation) > -12 MeV and the imaginary part, $W_\Sigma < -7$ MeV through their study on the shape of the spectrum in unbound region (figure 1.11, [28]).
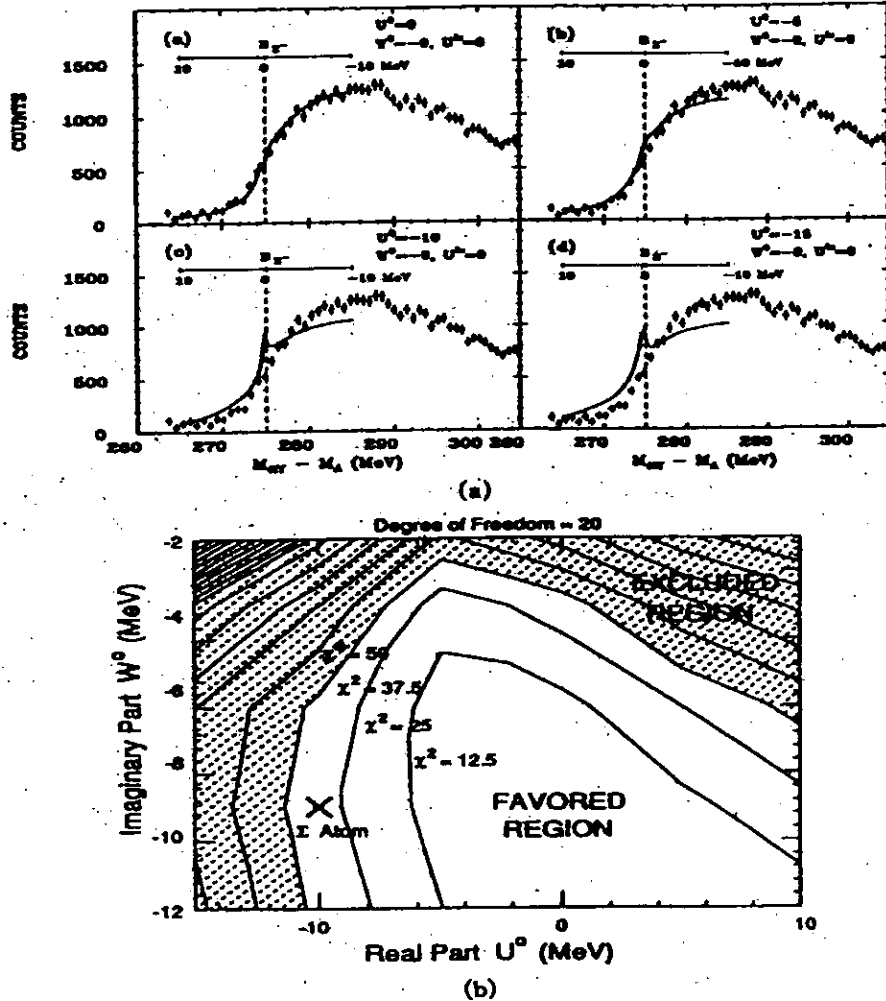
Figure 1.11:Inclusive ^{12}C(K^-, π^+) spectrum and the results of full DWIA calculation [29, 30].
(a) Calculated spectra with the real part $U_\Sigma = 0$, $-5, -10$, -15 MeV and the imaginary part $W_\Sigma = 9$ MeV are overlaid.
(b) Contour plot showing the allowed region of U_Σ and W_Σ.

Recently, it is demonstrated that the (π^-, K^+) spectrum is found to be sensitive to the Σ-nucleus potential [31], where two types of potential are considered in the calculation, which are derived phenomenologically (figure 1.12). One is based on the one boson exchange potential (OBEP) describing the two-body YN interaction (Nijmegen Model D (ND) equivalent) and the other one is obtained from the Σ^--atomic X-ray data with assuming the non-linear potential shape with respect to the nucleon density distribution. The calculated (π^-, K^+) spectrum on Si based on the former potential is denoted as 'ND' and the latter as 'atom' in figure 1.13.

The potential 'ND' represents an attractive real part and moderately absorptive imaginary part where the 'atom' represents a strongly repulsive real part and deeply absorptive imaginary part. Naturally, seen from the figure 1.13, the response of the spectra both above and below the binding threshold are different and opposite from each other. Experimental observation is needed to compare with and so as to discriminate them.

In KEK-PS E438, we thus proposed to measure the inclusive (π^-, K^+) spectra mainly in heavy nuclear systems with high statistics in order to extract the Σ single-particle potential [32].

Another way of Σ-nuclear spectroscopic study named as Coulomb-assisted hybrid bound state (CAHBS) may be observed as a narrow peak for the medium nuclear system, which was mentioned first by Yamazaki et al [33]. Later, in heavy nuclear system Akaishi et al [34] also figured out the possibility to observe the CAHBS as a narrow peak by using (π^-, K^+) reactions. Obviously, CAHBS could provide invaluable information on the Σ-nucleus potential if it exists and can be the next step of our present study.

1.4   Inclusive (π^-, K^+) spectrum

In the present experiment, we have measured the inclusive (π^-, K^+) spectra on CH_2, silicon, nickel, indium and bismuth targets near the Σ^- production threshold. Since the (π^-, K^+) spectrum reflects the low energy Σ-nucleus scattering, the analysis of the spectrum shape would give the Σ-nucleus optical potential. The framework of the Distorted Wave Impulse Approximation (DWIA) has been often applied to calculate the inclusive spectra ([35, 52], for example). The differential cross section of the (π^-, K^+) reaction in terms of DWIA can be expressed as

$$\frac{d^2\sigma}{d\Omega dE} = \beta \cdot \left(\frac{d\sigma}{d\Omega}\right)_{ele} \cdot S(E) , \tag{1.2}$$

where β is the kinematical factor, $\left(\frac{d\sigma}{d\Omega}\right)_{ele}$ is the Fermi-averaged differential cross section for the elementary process $(\pi^- + p \rightarrow K^+ + \Sigma^-)$, and $S(E)$ is the strength
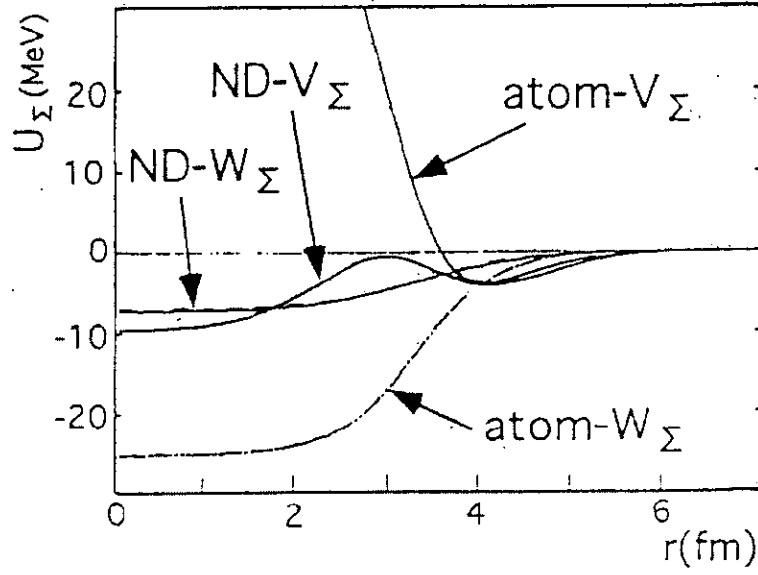
Figure 1.12: Real parts, V_Σ and imaginary parts, W_Σ of typical potentials, 'ND' and 'atom', for ^{28}Si.
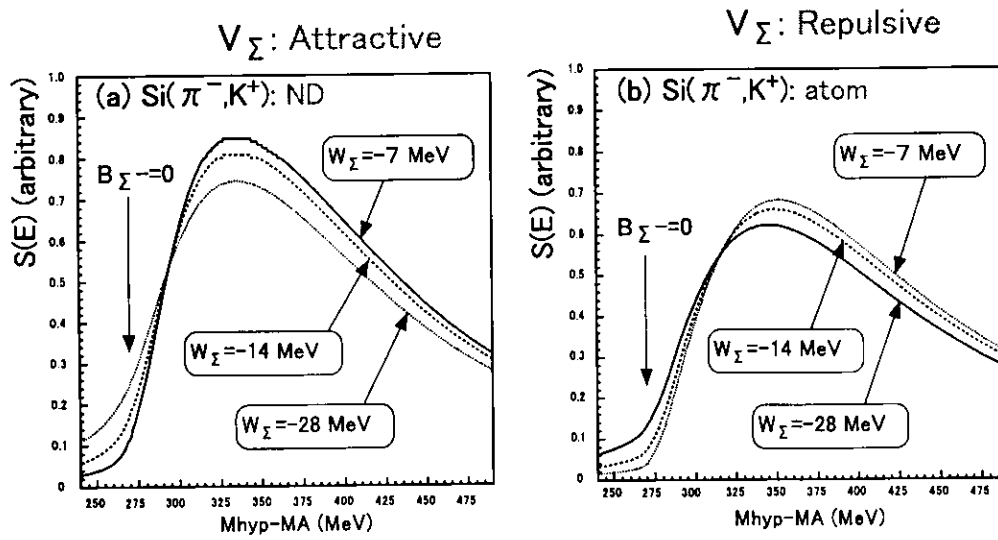
Figure 1.13: Calculated (π^-, K^+) spectra on Si bu using two typical potentials and when the imaginary potential depth is changed artificially in both cases [31].

function. A gross feature of the spectrum is described by $S(E)$ in this formalism, where the strength function $S(E)$ can be expressed as

$$S(E) = \frac{-1}{\pi} Im \sum_{\alpha\alpha'} \int dr \int dr' f_\alpha^+(r) G_{\alpha\alpha'}(E; r, r') f_{\alpha'}(r') \qquad (1.3)$$

Here, $f(\alpha)$ is the form factor characterized with the distorted wave of the incident and outgoing particles and the residual nuclear state as in equation 1.4. $G_{\alpha\alpha'}$ is the Green function for the Σ-nucleus system in the coupled channels description. $f(\alpha)$ and $G_{\alpha\alpha'}$ are usually expressed as

$$f_\alpha(r) = \chi^{(-)*}(R)\chi^+(R) < \alpha|\psi_N(r)|i > \qquad (1.4)$$

$$R = (M_c/M_{hy})r \qquad (1.5)$$

and

$$G_{\alpha\alpha'}(E; r, r') = < \alpha|\psi_\Sigma(r) \frac{1}{E - H - i\eta} \psi_\Sigma^+(r')|\alpha' > \qquad (1.6)$$

If H can be described with a single-particle optical potential U_Σ, G is given as a solution of the following equation,

$$(\frac{\hbar^2}{2\mu}\Delta + E - U_\Sigma)G(E; r, r') = -\delta(r - r') \qquad (1.7)$$

Therefore, $S(E)$ is respondent to U_Σ.
Further description of the Green's function method is presented in appexdix A.

1.5 Present experiment

The present experiment was carried out at the K6 beam line of KEK 12-GeV Proton Synchrotron (PS) with the SKS spectrometer system. SKS, which has a wide momentum acceptance, satisfies our experimental requirement well so as to obtain high-statistics data. The elementary process of

$$\pi^- + p \rightarrow K^+ + \Sigma^- \qquad (1.8)$$

was used to produce a Σ^- hyperon which we denote here by $p(\pi^-, K^+)\Sigma^-$. The incident pion momentum was chosen to be 1.2 GeV/c. As shown in figures 1.14 and 1.15 the elementary production cross section decreases rather smoothly according to the incident beam energy, while the recoil momentum of the produced Σ^- rapidly decreases to $\sim$ 400 MeV/c at around 1.2 GeV/c. Rapid change of recoil momentum makes the spectrum analysis complicated. Larger recoil momentum requires wider momentum acceptance for the kaon spectrometer. Therefore, we compromised between the yield and sensitivity to select beam momentum 1.2 GeV/c as an optimum.

The calibration of the energy scale is one of the key point of the present experiment as the shape and yield of the spectrum near the binding threshold is most
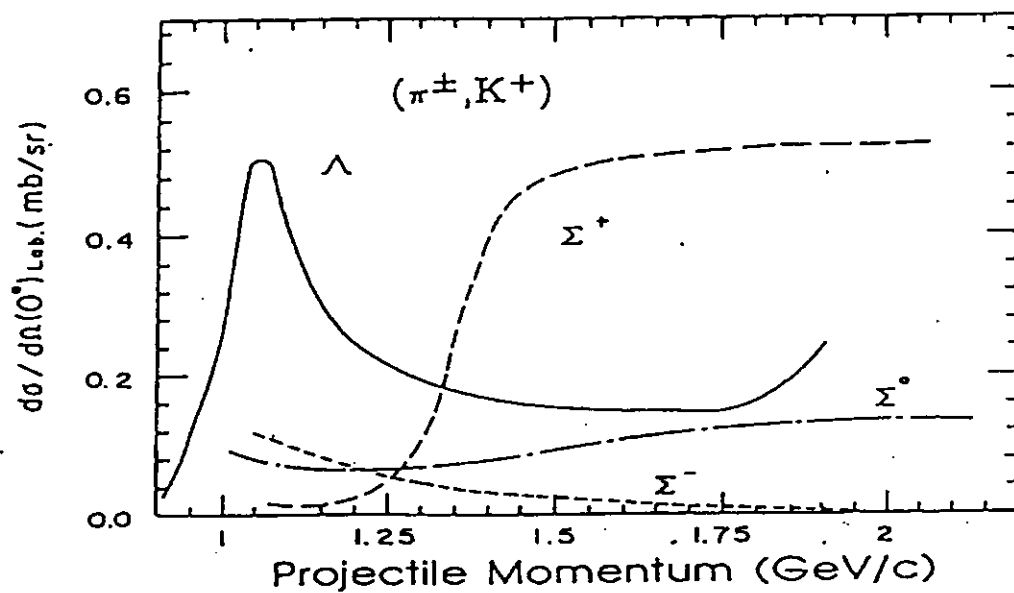
Figure 1.14: Cross section of the elementary process, $\pi N \rightarrow KY$, as a function of the projectile momentum [36].
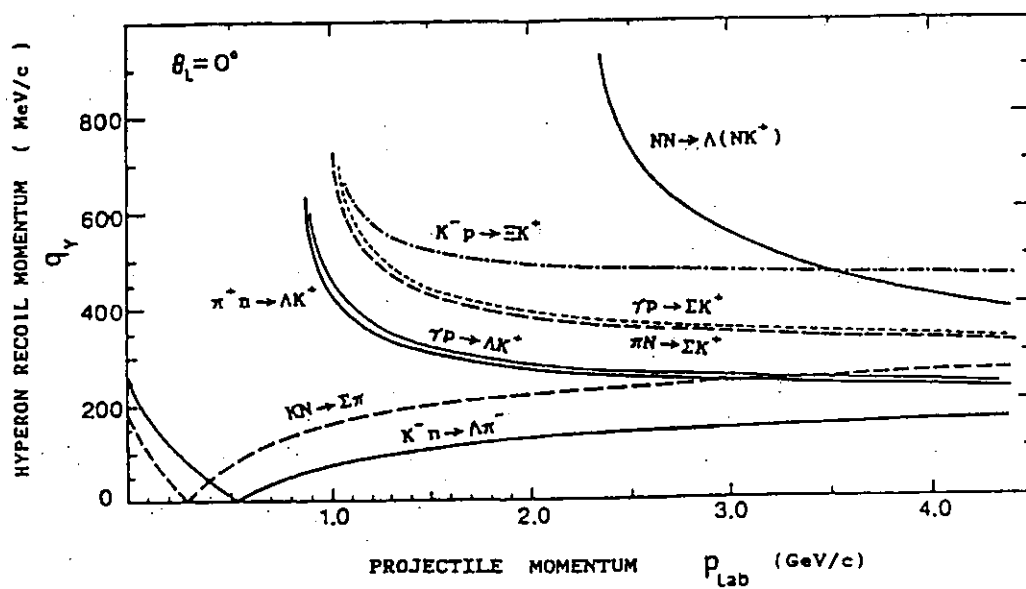
Figure 1.15: Momentum transfer in $\pi N \rightarrow KY$ reactions as a function of projectile momentum [36].

14

sensitive to the Σ^--nucleus potential. In order to calibrate the energy scale so as to determine the Σ^- binding energy threshold with high precision, we put a CH_2 target 25 cm upstream from the scattering target. We could always monitor the energy scale from the elementary process, $p(\pi^-, K^+)\Sigma^-$ throughout the experiment. The intrinsic momentum resolution of SKS is already achieved to be ~ 2 MeV in FWHM in previous experiment, which is very much helpful to check the sensitivity of the imaginary part of the potential, because a bad resolution may cause a spectrum to smear out. However, as the imaginary part, W_Σ is expected to be less than -7 MeV [22], putting CH_2 target together with the scattering target would not affect the present purpose. The mass-number dependence of the quasi-free Σ^- production cross sections is important to understand the reaction mechanism. Moreover, as discussed earlier in the heavy nuclear system where neutrons dominate in number, the iso-vector term may appear in the Σ^--nucleus folding potential, since the Σ^--p potential is different from the Σ^--n one. In order to cover a wide mass-number region we used CH_2, silicon, nickel, indium and bismuth targets.

The present thesis is arranged by the following order.
The experimental setup and the obtained data summary are discussed in chapter 2. Detail procedures of data analysis together with energy scale calibration are described in chapter 3. Experimental results are presented in chapter 4. Discussions on the present results, comparison of the Si spectrum to the Monte Carlo simulation as well as comparison with theoretical spectra are presented in chapter 5. Conclusion is in chapter 6. A brief description of the Green's function method is presented in Appendix A. (π^+, K^+)quasi-free spectra on CH_2 and Si targets were also measured in the present experiment. Observed spectra on C and Si are presented in the appendix B. In Appendix C, procedure of the eikonal approximation is described. A brief description of the Monte Carlo simulation is given in Appendix D. Inclusive (π^-, K^+) spectra are presented as tables in Appendix E.

Chapter 2

Experimental Setup

2.1 Overview

The present experiment was carried out at the 12 GeV proton synchrotron(PS) in High Energy Accelerator Research Organization(KEK) by using the K6 beam line together with the Superconducting Kaon Spectrometer(SKS) system.

As the beam momentum of negative charged pion was fixed to be 1.2 GeV/c, K6 beam line was the most suitable place to have good pion beam in this momentum region. In addition, the large acceptance(100 msr) of SKS together with good momentum resolution of 0.1%(FWHM) in a momentum range of 1 GeV/c was one of the unique choice of this experiment mainly in terms of statistics as well as in momentum resolution. The experimental setup consists of mainly two parts: The beam line spectrometer system, in order to measure the incident beam momentum and the SKS spectrometer system for that of scattered particles. Figure 2.1 shows the whole experimental setup of the present experiment (KEK-PS E438).

The detail description of the whole experimental setup is organized as follows: The design of K6 beam line is described in section 2.2. Beam spectrometer is mentioned in section 2.3 and the scattered particle spectrometer is in section 2.4. Trigger type is in section 2.5 and the data-acquisition system is in section 2.6. Experimental targets and the details of data summary are presented in section 2.7.

2.2 K6 beam line

The K6 beam line is located at the north counter hall of KEK 12-GeV proton synchrotron(PS) which is a general-purpose high-intensity beam line. It supplies mass-separated secondary beams in the momentum region of around 1 GeV/c. Figure 2.2 shows a schematic diagram of the k6 beam line. The beam line consists of two dipole magnets(D1, D2), ten quadrupole magnets(Q1 - Q10), a sextuple magnet(SX), an electrostatic (DC) separator with two correction magnets(CM1, CM2) and four slits. The name and locations of these slits are specified in table 2.1. The primary proton beam was extracted for ~0.7 second in each 3.0 seconds, synchronized to the KEK 12-GeV PS operation cycle.
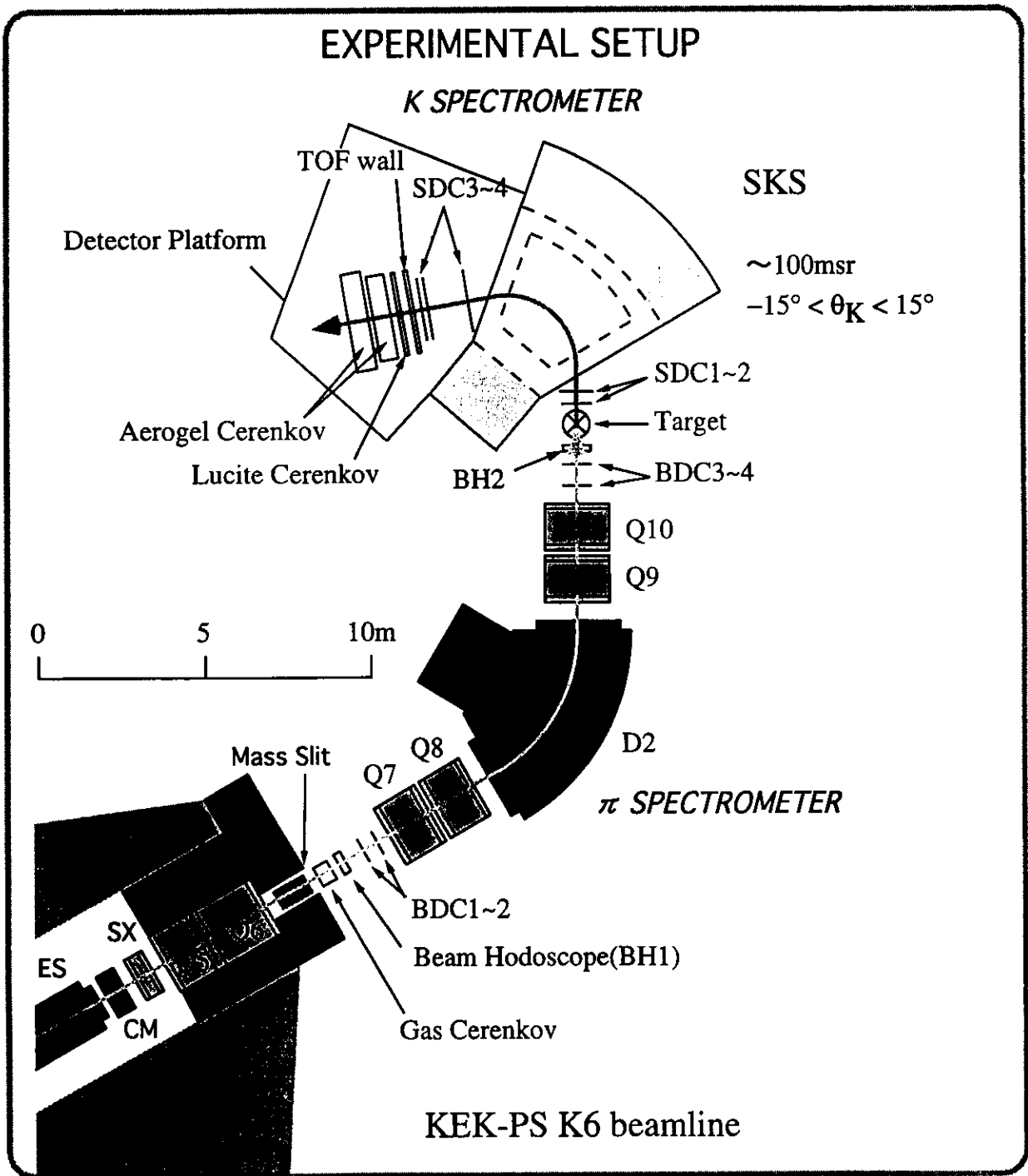
Figure 2.1: Experimental setup of the present experiment(KEK-PS E438)

- Central momentum of the π^- beam spectrometer was 1.2 GeV/c.
- Central momenta of the SKS were 0.63 GeV/c (1.9 T mode), 0.72 GeV/c (2.2 T mode) and 0.78 GeV/c (2.4 T mode).

The production target to produce secondary pion by the primary proton beam was located at the most upstream of the k6 beam line. A platinum rod of $\phi 6 \times 60$ mm^2 was used as the production target. The intensity of primary protons on the production target was typically 1.2×10^{12} protons/spill.

The mass and momentum of the secondary pion was then selected and achromatically focused on the experimental targets. The measured beam size was typically 5.2 mm (horizontal)$\times$8.5 mm (vertical) in rms, as shown in Figure 2.3. In the present experiment, the central beam momentum was set to be 1.2 GeV/c where the threshold momentum of the $p(\pi^-, K^+)\Sigma^-$ reaction is at 1.035 GeV/c. Beam intensity at the experimental targets was adjusted around $1.5 \sim 2.3 \times 10^6$/spill, to avoid detection efficiency drop due to high counting rates as well as to avoid deterioration of the momentum resolution.
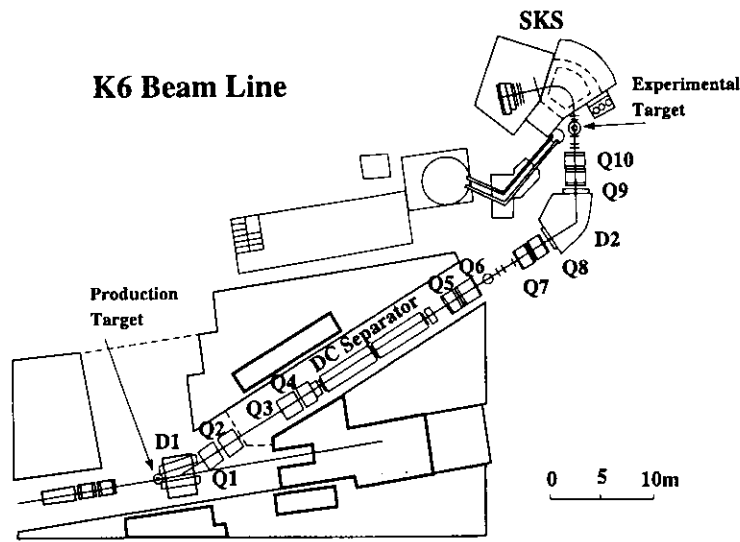
Figure 2.2: K6 beam line

2.3 Beam spectrometer

The beam spectrometer system is the end part of k6 beam line which is used to analyze the beam, particle by particle. Figure 2.4 shows a schematic view of the beam spectrometer. It consists of a QQDQQ magnet system together with four sets of drift chambers(BDC1 $\sim$ BDC4) for the momentum reconstruction and three trigger counters. The trigger counters comprise a Freon-gas Čerenkov counter(eGC) and two sets of segmented scintillation counter(BH1,BH2). In order to maintain a momentum resolution of 0.1%(FWHM) at around 1 GeV/c, a third-order transport matrix was used for the momentum reconstruction. To minimize multiple-scattering effects on the momentum resolution, the $< x \mid \theta >$ term of

18
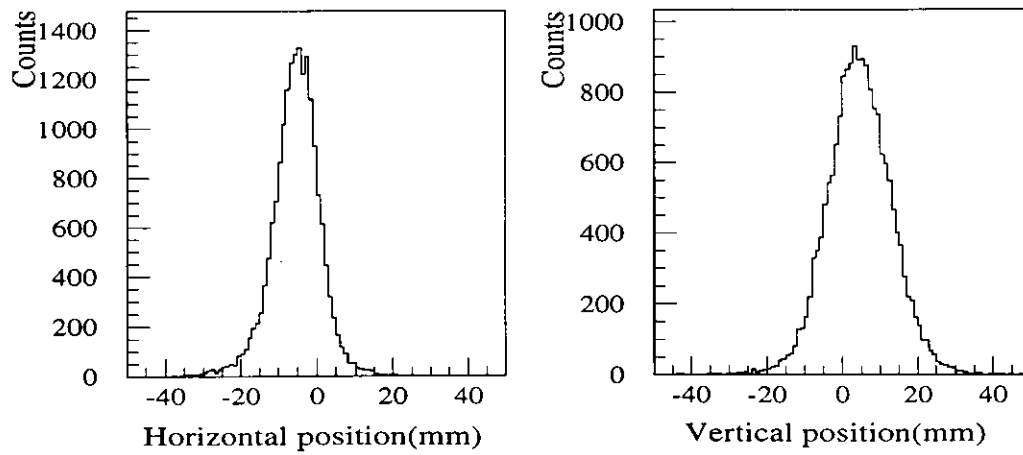
Figure 2.3: Typical beam profile at the experimental target

Table 2.1: List of slits on K6 beam line

name	located between...
acceptance slit	D1&Q1
intermediate focus slit	Q2&Q3
momentum slit	DC&Q5
mass slit	Q6&Q7

Table 2.2: Design specification of the beam spectrometer

momentum resolution	0.1% (FWHM)
momentum bite	±3%
maximum momentum	1.2 GeV/c
bending angle	60°

the transport matrix was tuned to be zero. In addition, the beam pipe in the QQDQQ system was evacuated with a Kapton window of 100 μm thickness, and the tracking chambers were made as thin as possible in substance. The magnetic field of the D2 magnet was monitored during the experiment every spill with a high-precision Hall probe in order to correct its fluctuation in the off-line analysis. Design specifications of the beam spectrometer are listed in table 2.2.
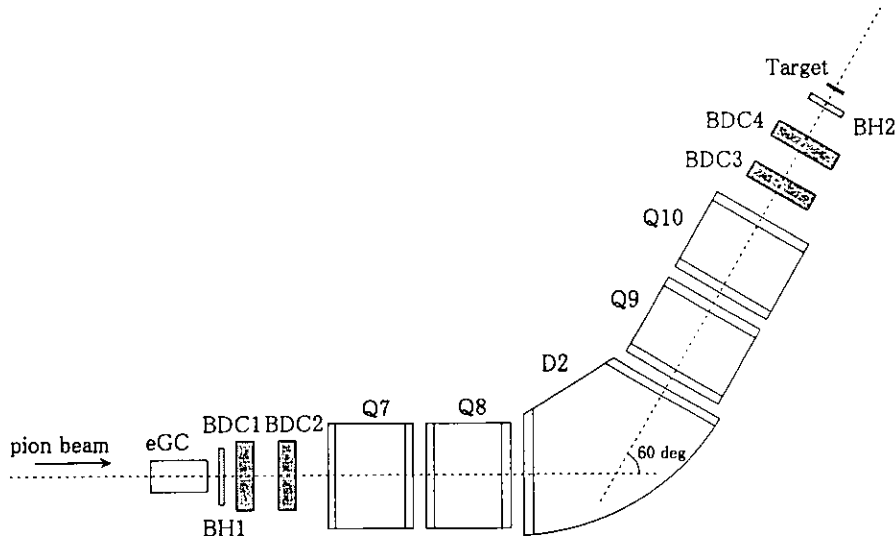
Figure 2.4: Schematic view of the beam spectrometer

2.3.1 Trigger counters

Trigger counters of the beam spectrometer consist of a Freon-gas Čerenkov counter (eGC) and two sets of scintillation counter(BH1, BH2). Specifications of these three trigger counters are listed in table 2.3.

The eGC was located just downstream of the mass slit. The electron contamination in the pion beam was rejected with this counter by a rejection efficiency of better than 99.9%.

The BH1 was a segmented scintillation counter, which was located just downstream of eGC. Figure 2.5 shows a schematic view of BH1. It was segmented into seven vertical pieces of 5 mm-thick plastic scintillator in order to reduce the counting rate. The size of each segment was adjusted so that the single-counting rate in each segment could nearly be equal. To avoid any dead space, each segment was overlapped with its adjacent segments by 0.75 mm. Each segment was equipped with phototubes having three-stage booster on both ends.

20

The BH2 was located just close the the experimental target to define the beam hitting the experimental target. Figure 2.6 shows a schematic view of the BH2 counter. This counter was used as a time-zero counter for timing measurement of the scattered particles. It was segmented into five vertical pieces of 3 mm-thick plastic scintillator. Each segment was equipped with phototubes having three-stage booster on both ends. Since BH2 was placed between the beam spectrometer and the scattered particle spectrometer, it was made as thin as possible in order to minimize the energy-loss straggling in this counter. By requiring timing coincidence between BH1 and BH2, the contamination in the pion beam was rejected sufficiently.
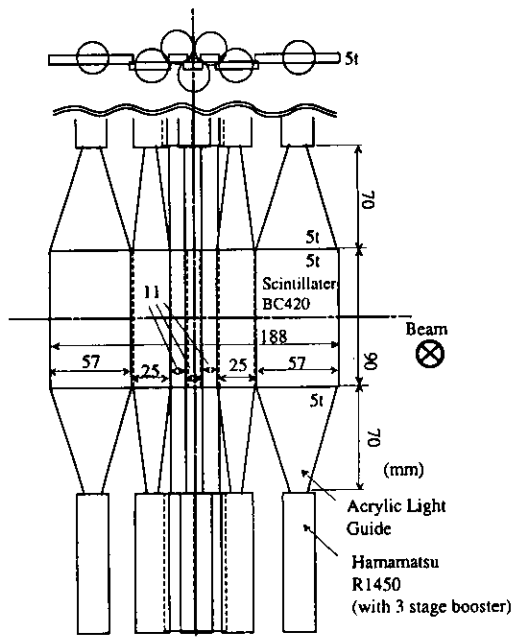
Figure 2.5: BH1 configuration
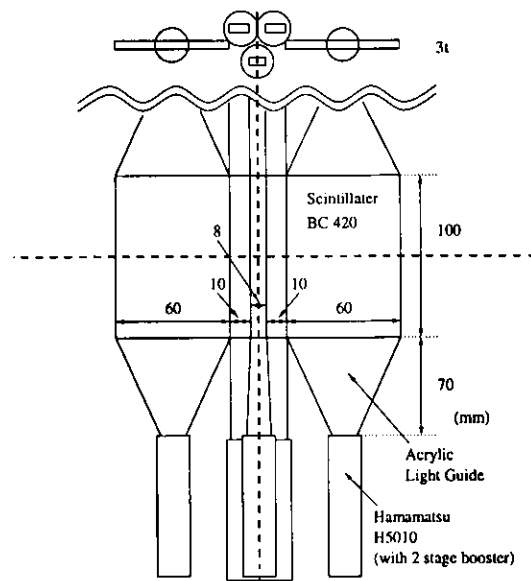
Figure 2.6: BH2 configuration

21

Table 2.3: Specifications of the trigger counters

name	sensitive area (cm)	PMT (Hamamaatsu)	etc.
GC	$\phi 20 \times 29^L$	R1584-02×1	Freon-12, n=1.00245
BH1	$19^W \times 9^H \times 0.5^T$	R1450×14	7-segments, 3-stage-booster
BH2	$14.8^W \times 10^H \times 0.3^T$	R5010×10	5-segments, 2-stage-booster
TOF	$105^W \times 100^H \times 3^L$	R1949×30	15-segments
AC1	$105^W \times 120^H \times 9^L$	R1584-02×18	n=1.06
AC2	$140^W \times 140^H \times 12^L$	R1584-02×20	n=1.06
LC	$140^W \times 140^H \times 4^L$	H1949×28	14-segments, n=1.49

2.3.2 Drift chambers

The properties of the drift chamber are summarized in tables 2.4 and 2.5. The beam line drift chambers, BDC1 $\sim$ 4, had the same plane configuration and cell structure as shown in figure 2.7 and figure 2.8, respectively. In order to operate under high counting rates of several M/spill, the sense-wire spacing was made to be short(5 mm). Furthermore, read-out electronics of the pre-amplifier/discriminators are equipped with two-stage pole-zero cancellation and one baseline restorer. Each chamber has six layers of sense-wire planes ($xx'uu'vv'$), where vertical and $\pm 15°$ tilted-wire planes are denoted by x, u and v, respectively. In each pair plane, the sense-wire position is shifted by a half of a cell size of 2.5 mm in order to solve any left/right ambiguity, as shown in figure 2.8. The sense wire is a gold-plated 12.5 μm-diameter tungsten wire and the field wire is a gold-plated 75 μm-diameter copper-beryllium wire. The cathode planes are made of 7.5 μm-thick kapton, both sides of which are coated with 0.1 μm aluminum and 0.0025 μm chromium for preventing oxidization of the aluminum coating. The gas mixture was $Ar(76\%)+C_4H_{10}(20\%)+Methylal(4\%)$ at atmosphere pressure.
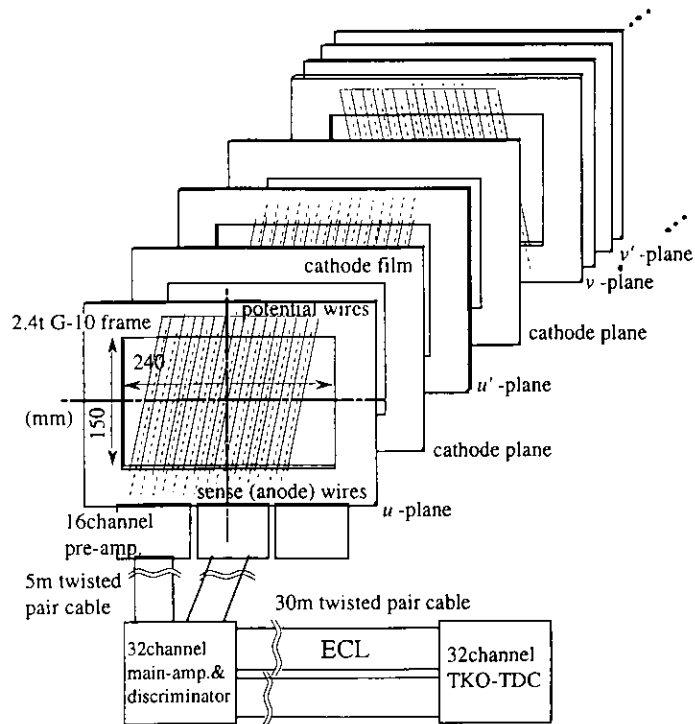
Figure 2.7: Plane configuration of BDCs and SDC1,2
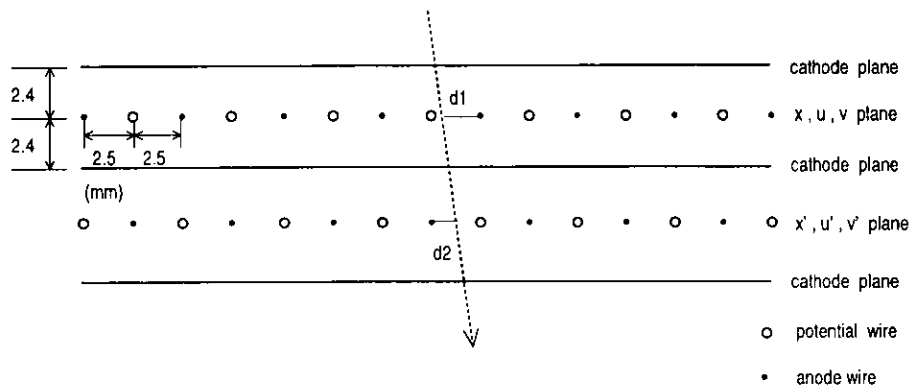
Figure 2.8: Cell structure of BDCs and SDC1,2

23

Table 2.4: Specifications of the drift chambers I

name	area (cm)	drift space (mm)	wires	thickness (in L_R)	resolution (r.m.s. in μm)
BDC1-4	$24^W \times 15^H$	2.5	$xx'uu'vv'$	1.79×10^{-3}	300
SDC1	$24^W \times 15^H$	2.5	$uu'vv'$	1.79×10^{-3}	300
SDC2	$56^W \times 20^H$	2.5	$xx'uu'vv'$	1.79×10^{-3}	300
SDC3	$90^W \times 90^H$	21	$xx'yy'$	0.53×10^{-3}	250
SDC4X	$100^W \times 100^H$	21	$x \times 6$	1.05×10^{-3}	250
SDC4Y	$100^W \times 100^H$	21	$y \times 6$	1.05×10^{-3}	250

Table 2.5: Specifications of the drift chambers II

name	gas	wire material
BDC1-4	Ar 76%+C_4H_{10} 20%	sense: gold-plated tungsten, $\phi = 12.5\mu$m
SDC1-2	+ Methylal 4%(STD)	field: gold-plated copper beryllium, $\phi = 75\mu$m
SDC3	Ar 50% + C_2H_4 50%	sense: gold-plated tungsten, $\phi = 20\mu$m
SDC4	(STD)	field: gold-plated aluminum wire, $\phi = 80\mu$m

2.4 Scattered-particle spectrometer(SKS)

The scattered particle spectrometer known as superconducting kaon spectrometer(SKS) is comprised of a superconducting dipole magnet with four sets of drift chambers(SDC1 $\sim$ SDC4) for the momentum reconstruction and three kinds of trigger counter for the particle identification. The trigger counters comprised of a scintillation counter wall(TOF), two silica aerogel Čerenkov counters(AC1,AC2) and a Lucite Čerenkov counter wall(LC)(figure 2.1).

Design specifications of the SKS are summarized in table 2.6. The characteristic feature of the SKS is to have a good momentum resolution of 0.1%(FWHM) together with a large acceptance of 100 msr at around 1 GeV/c. Simultaneously, it keeps the flight path as short as 5 m for the central trajectory in order to minimize kaon decay-in-flight, and has a powerful kaon identification ability. The SKS enables us to perform the present experiment with a good energy resolution and in high statistics. Figures 2.9 and 2.10 show schematic views of the SKS.

2.4.1 The superconducting magnet

A single sector-shape dipole magnet with a large aperture of 50 cm was adopted in order to realize the specifications mentioned above. The magnet is so large and powerful that the bending angle is as large as 100°. Unlike conventional high-resolution spectrometers used in nuclear physics, the SKS has no well-defined focal plane. The sector-shape gives the SKS an approximate focusing property, which makes the large acceptance possible with the large aperture. Table 2.7 shows design parameters of the superconducting magnet [38, 39].

The scattered-particle momentum was obtained particle by particle by reconstructing a particle trajectory with the Runge-Kutta tracking method using a precisely measured magnetic field map [1]. In order to reduce multiple scattering effects on the momentum resolution, the tracking chambers were made as thin as possible in material, and the spaces along the particle trajectory were filled with helium bags.

In the present experiment, SKS was excited at 1.9 T (210 A), 2.2 T (272 A) and 2.4 T (320 A), correspond to the central momenta of 0.63 GeV/c, 0.72 GeV/c and 0.78 GeV/c, respectively. Table 2.8 shows a relation between the SKS current and momentum of a central trajectory. The magnetic field was monitored with an NMR probe and the field fluctuation was within ±0.003% throughout the beam time.

Table 2.6: Design parameters of the SKS [37].

Momentum resolution	0.1% FWHM at 720 MeV/c
Maximum central momentum	1.1 GeV/c
Momentum bite	±10%
Bending angle	100° for the central trajectory
Solid angle	100 msr
Flight path	∼5 m for the central trajectory
Pole gap	49.75 cm

Table 2.7: Design parameters of the SKS superconducting magnet.

Maximum magnetic field	3 T
Stored energy	10.6 MJ
Conductor	NbTi/Cu
Ampere turns	2.1 MA·T
Maximum current	500 A
Total Weight	280 t
Heat leak at 4 K	5 W
Content of Liq. He	156 ℓ

Table 2.8: SKS current, central momentum and magnetic field

current [A]	central momentum [GeV/c]	central magnetic field [T]
210	0.63	1.9
272	0.72	2.2
320	0.78	2.4
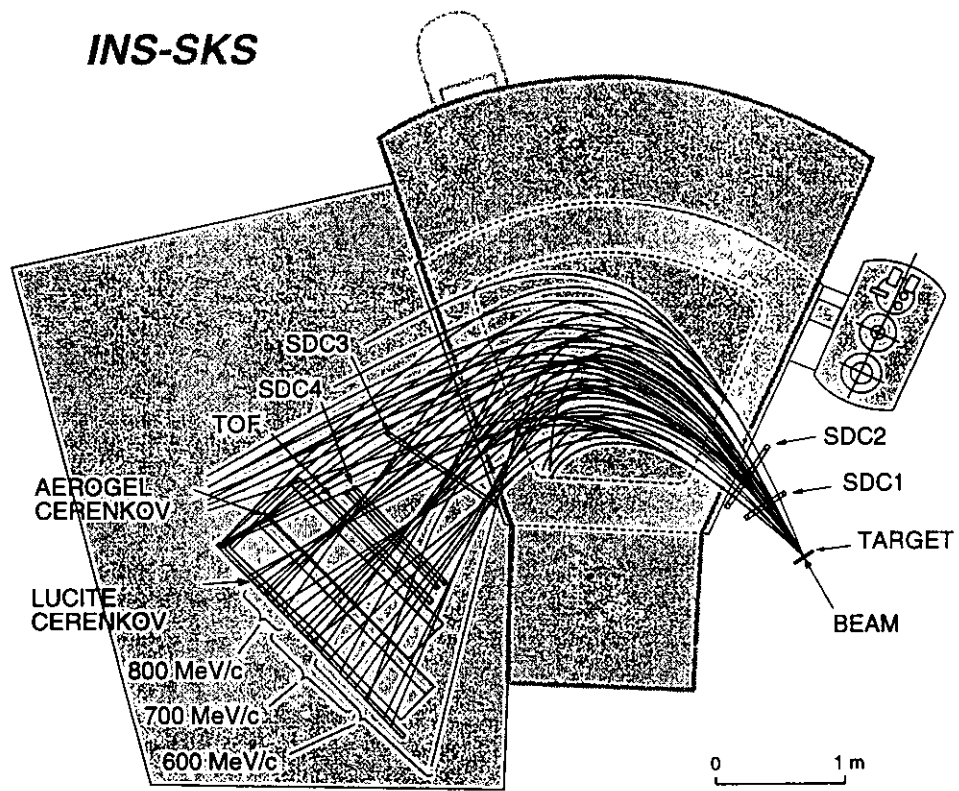
Figure 2.9: Schematic top view of the SKS.
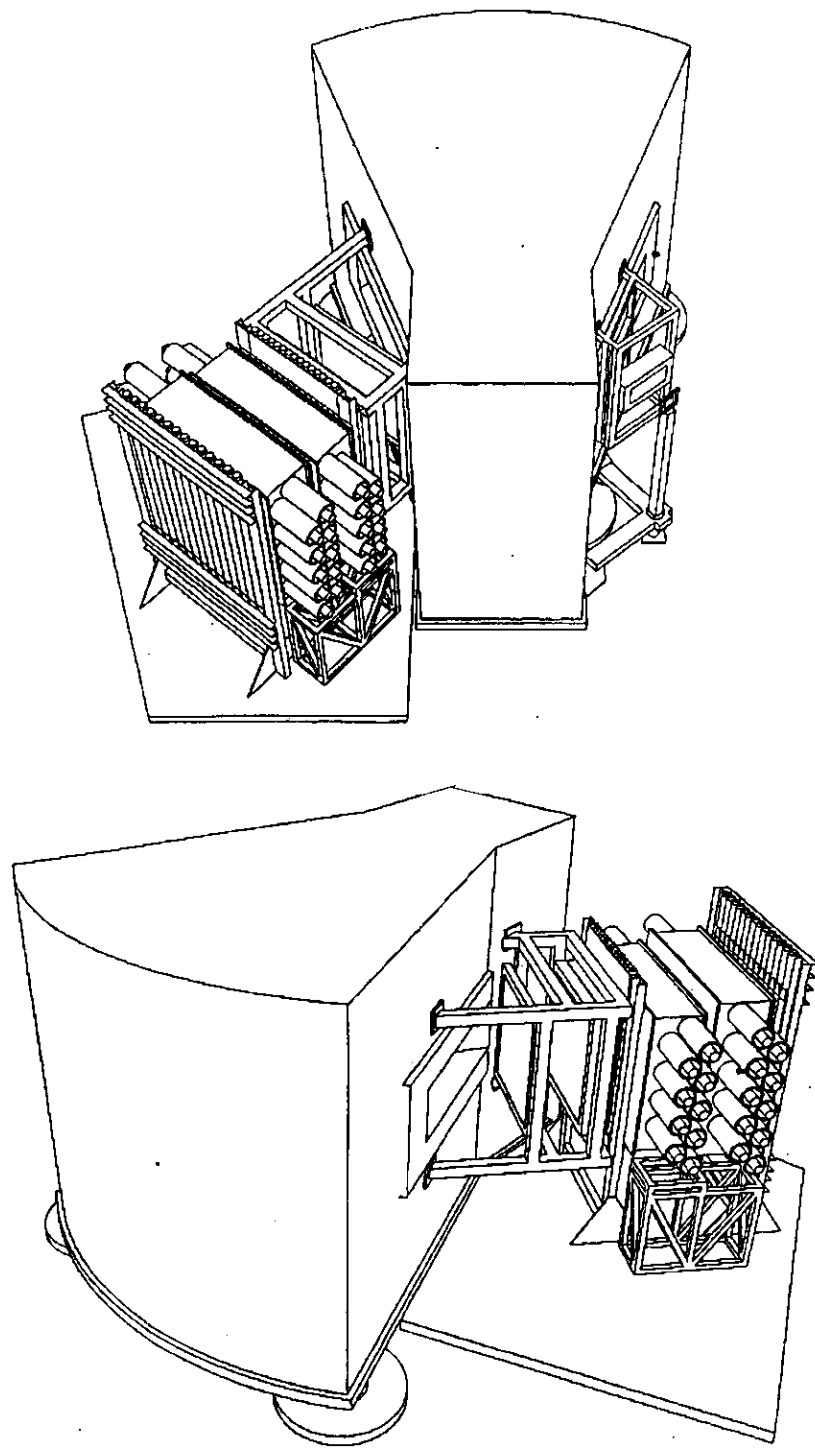
Figure 2.10: Bird's-eye views of the SKS.

2.4.2 Trigger counters

Table 2.3 shows the specifications of the trigger counters. A combination of three kinds of counter in the trigger label selected the scattered pion, kaon and proton. Trigger counters are a scintillation counter wall (TOF), two silica-aerogel Čerenkov counters (AC1, AC2) and a lucite Čerenkov counter wall (LC). TOF is sensitive to the charged particles, AC1 and AC2 are sensitive only to pion and the LC is insensitive to proton.

Table 2.9: Sensitivity of SKS counters for 720 MeV/c particles

Table 2.9 briefly shows the sensitivity of those counters for the scattered particle of momentum 720 MeV/c. Scattered particles were roughly identified by these counters in the data taking stage.

	π	K	p
TOF	○	○	○
LC	○	○	×
AC1&2	○	×	×

○ : sensitive   × : insensitive

The TOF counter was used for the scattered particle identification by measuring the time-of-flight from the reaction point. It was located just behind of the SDC4Y. As shown in Figure 2.11, it is segmented into fifteen vertical pieces of $7\times100\times3$ cm^3 plastic scintillator. Each segment is equipped with fast phototubes on the top and bottom sides. The timing resolution is good enough to separate the scattered pions, kaons and protons.

The LC is a threshold-type Čerenkov counter comprising fourteen vertical pieces of $10\times140\times4$ cm^3 lucite radiators, shown in Figure 2.12. Each segment is equipped with fast phototubes on the top and bottom sides. It was installed just after the TOF counter. A wave-length shifter of bis-MBS was mixed by 10 ppm in weight in the lucite radiator in order to enhance the direction efficiency for pions and kaons with various incident angles. The refractive index of a lucite was 1.49. Proton slower than 0.85 GeV/c were mostly rejected because of the Čerenkov light threshold, as shown in figure 2.14.

The AC1 and AC2 are silica aerogel Čerenkov counters used to veto pion with a threshold of 0.4 GeV/c, as shown in figure 2.14. The refractive index of a silica aerogel was 1.06. They were installed behind the LC wall. Figure 2.13 shows a schematic view of AC1. The structure of AC2 is essentially the same as that of AC1, except for the size. The sensitive area of AC1 is $105\times120\times9$ cm^3 and that of AC2 is $140\times140\times12$ cm^3. To realize uniform efficiency without any dead space over a large sensitive area, we adopted a two-layers counter system. For AC1 (AC2), we used 18 (20) phototubes which were sensitive to single photo-electron.
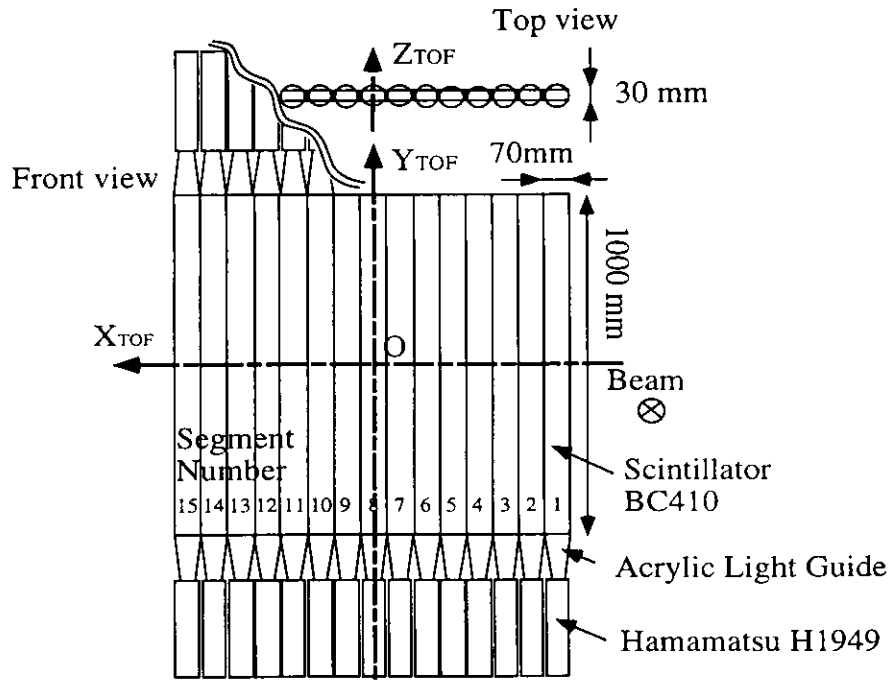
Figure 2.11: Schematic view of the TOF counter.
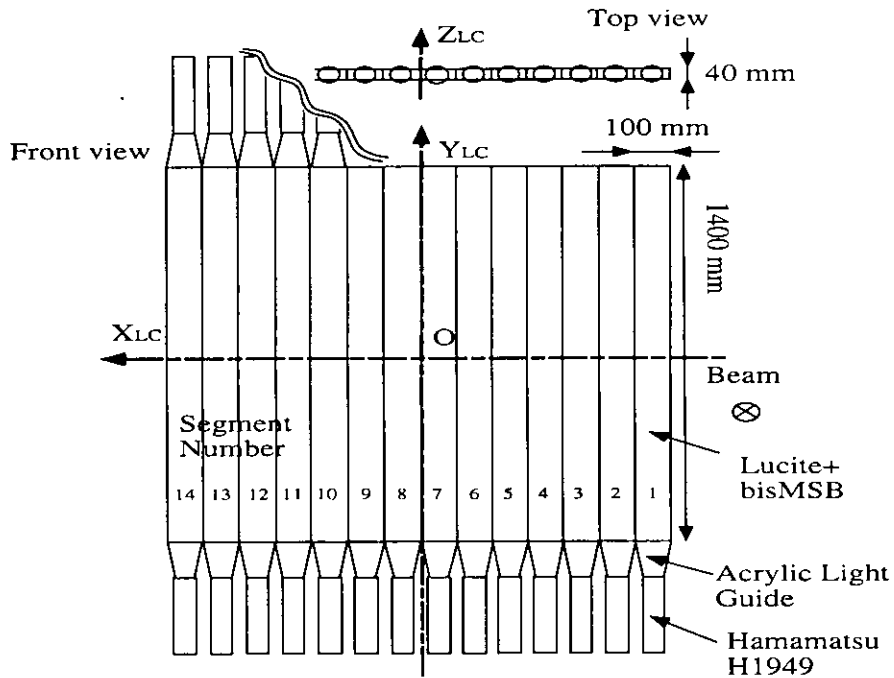
Figure 2.12: Schematic view of the LC counter.
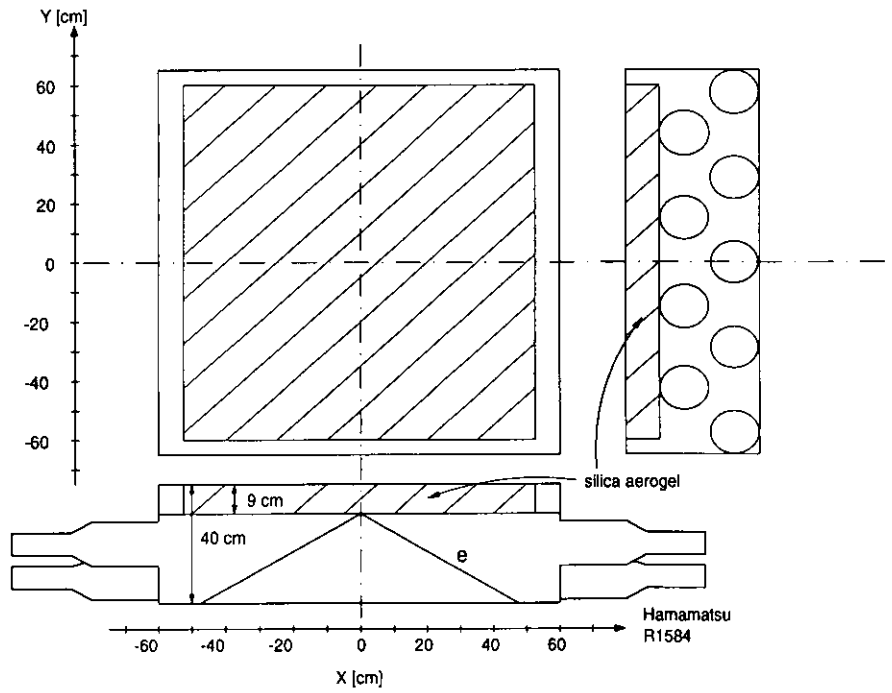
Figure 2.13: Schematic view of AC1.
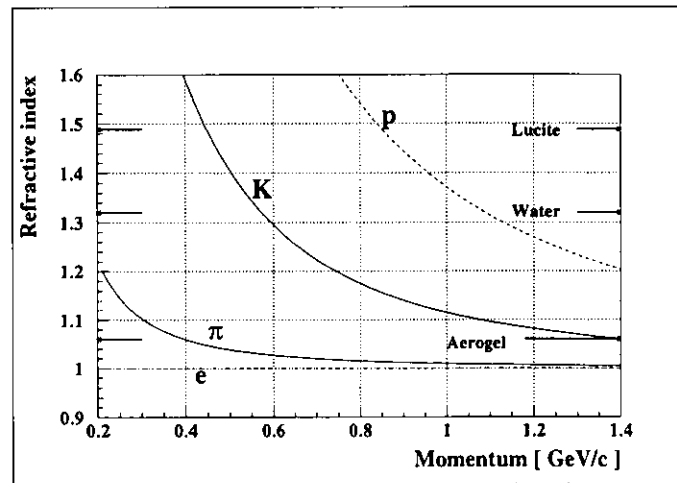
Figure 2.14: Threshold refractive index for Čerenkov radiation as a function of the momentum.

2.4.3 Drift chambers in the SKS

Specifications of the drift chambers in the SKS are listed in table 2.4 together with the beam line drift chambers.

SDC1 and SDC2 were placed at the entrance of SKS. They had the same configuration as BDCs since they were exposed to the beam. The SDC1 had four sense-wire planes(uu',vv') and the SDC2 had six sense-wire planes(xx',uu',vv').

The location of SDC3, SDC4X and SDC4Y were at the exit of SKS. They had a large drift space of ±21 mm, because they were installed at the exit of the magnet and the counting rate there was not so high. The size of the sensitive area of SDC3, SDC4X and SDC4Y was larger for covering the wide angular and momentum acceptance of the SKS. The SDC3 had four sense-wire planes(xx',yy'). In each pair plane, the sense-wire position was shifted by a half of a cell size in order to solve the left/right ambiguity.

The SDC4X and SDC4Y had six anode planes, as shown in figure 2.15. In each cell, the sense wires were staggered alternatively by ±200 μm in order to solve the left/right ambiguity. The staggering of the sense wire can be clearly seen in figure 2.15. Figure 2.16 shows a distribution of $\frac{1}{2}(x_2 + x_4) - x_3$, where x_n means the drift length of the nth plane of SDC4X. The two peaks correspond to the left and right-hand sides of the sense wire. The width of the peak shows the intrinsic position resolution of less than 250 μm in rms. In the off-line analysis, the two outermost sense wires in a cell were not used, because they were noisy due to their incomplete field shapes.

The sense and field wires of SDC3, SDC4X and SDC4Y are a gold-plated 20 μm tungsten wire and a gold-plated 80 μm aluminum wire, respectively. The gas mixture was $Ar(50\%)+C_2H_6(50\%)$ at atmospheric pressure. These properties are summarized in table 2.5.
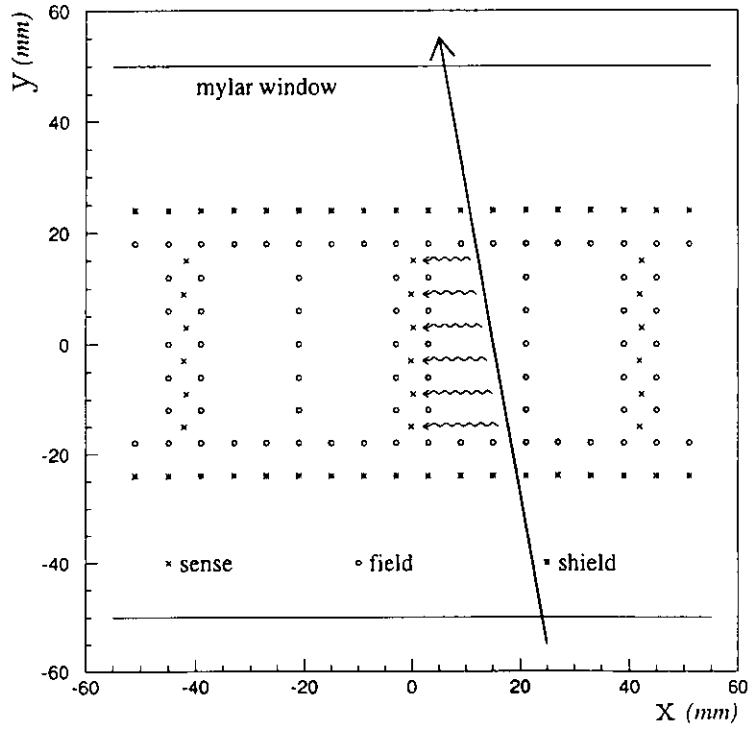
Figure 2.15: Cell structure of SDC4
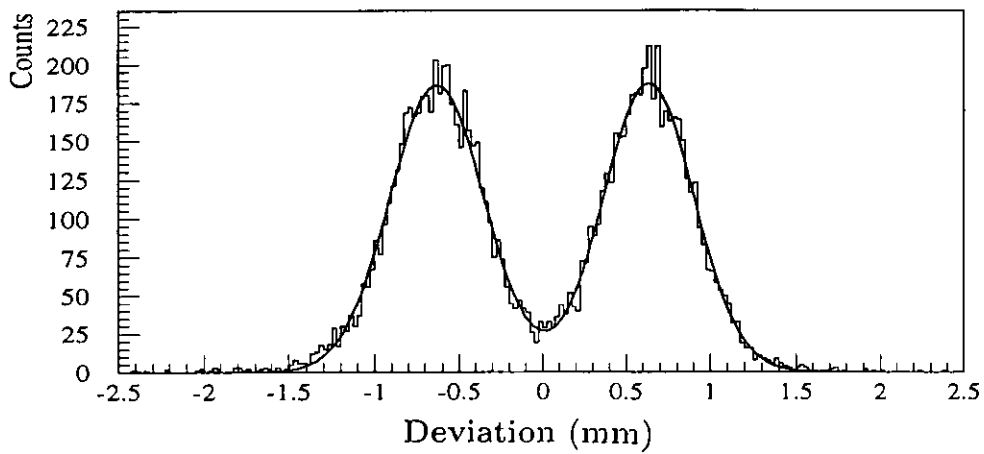
Figure 2.16: Distribution of $\frac{1}{2}(x_2 + x_4) - x_3$ of SDC4X measured for the scattered π^+, where x_n means the drift length of the nth plane of SDC4X.

33

2.5 Trigger

In order to reduce a lot of background particles produced through various pion-nucleus reactions, such as (π,p)X and (π,π)X, whose cross sections are typically a few order of magnitude larger than that of the (π^-,K^+) reaction, a good and powerful trigger system was required. In the present experiment, the (π^-,K^+) trigger was comprised of three kinds of counters in the beam spectrometer(BH1, BH2 and eGC), and three kinds of counters in the SKS spectrometer(TOF, AC1·2 and LC), as shown in figure 2.17.

Data was taken using the following three kinds of triggers mixed at a time:

$$
\begin{aligned}
BEAM &= BH1 \times BH2 \times \overline{eGC}, \\
PIK &= BEAM \times TOF \times LC \times \overline{AC1} \times \overline{AC2}, \\
PIPI &= BEAM \times TOF \times LC.
\end{aligned}
$$

Mean timer modules were used for BH1 and BH2 and had two PMT's at both ends so as to remove the incident-position dependence of the trigger timing. The proton contamination in the beam was rejected by a timing coincidence between BH1 and BH2 with a coincidence width of about 5 nsec.

The *BEAM* and the *PIPI* triggered data were used for calibration and efficiency estimation of the detector system. Mean timer modules were used for TOF and LC and had two PMT's at both ends so as to remove the incident-position dependence of the trigger timing. The *PIK* trigger rate was typically 400 counts/spill for a beam rate of about 1.5 M/spill. Most of these events came from background pions and protons from the target and other materials, such as BH2 and chamber support pillars.

The BH2 timing was used as the STOP signal of TDC's for BDC's, SDC1 and SDC2, while the TOF timing was used for SDC3, SDC4X and SDC4Y because a flight time from BH2 to the exit of the SKS varies according to the flight path and momentum of a particle.
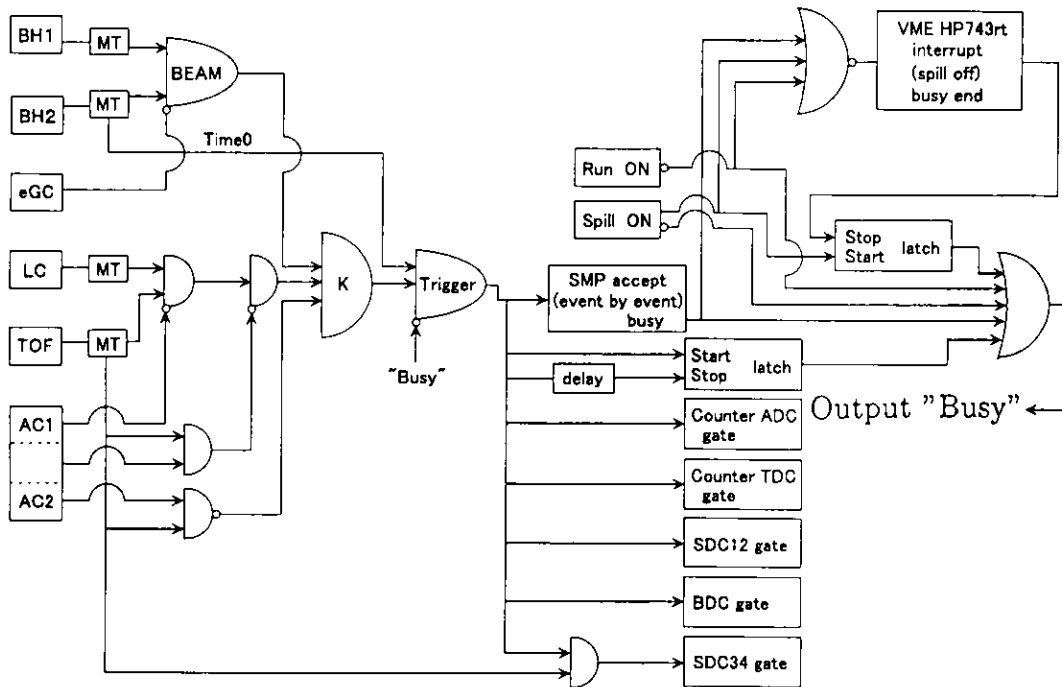
Figure 2.17: Trigger logic diagram.

2.6 Data-acquisition system

Figure 2.18 shows a diagram of the data-acquisition system. Raw signals from the detectors were digitized with TDC and ADC modules in the TKO boxes. The TKO is a standard developed at KEK. In a VME box, six VME-SMP's(Super Memory Partner) were installed. The VME-SMP was an interface module between a TKO bus and a VME bus, and had a local memory which could be access by a CPU module. During a beam spill on, event trigger signals were fed into the ACCEPT input of the VME-SMP's. Then the VME-SMP's read out the data of the TDC and ADC modules and stored them into their local memories. At the spill-end, the stored data are read out by the CPU module(HP743rt) which was the host computer. The CAMAC scalers in one crate were also read out via a VME-CAMAC interface(CES-8216) connected to a K3922 CAMAC crate controller. The data were written on DVD after being processed by the host computer. During the data-taking, most of the data were also transfered to a Linux workstation for an online monitoring. The data-acquisition task in VME was independent of the data-monitoring task in the workstation.
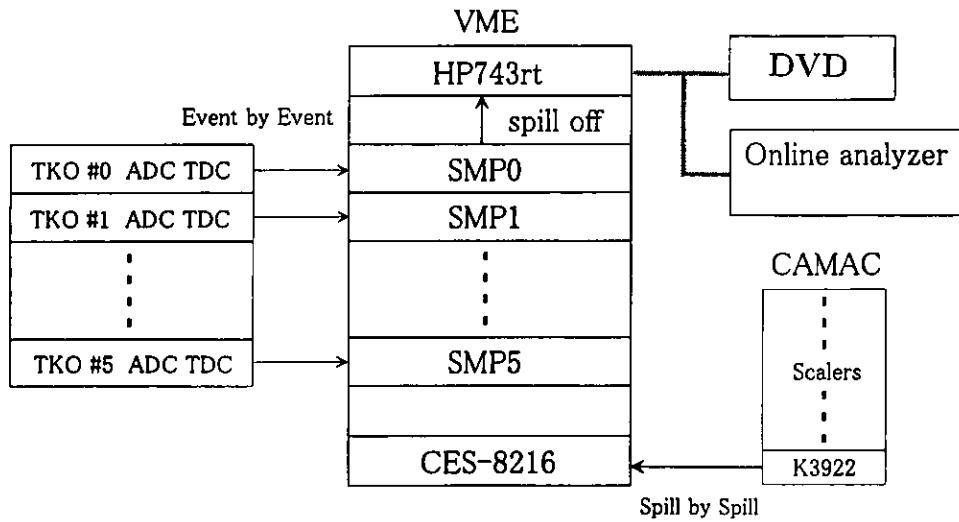
Figure 2.18: Schematic diagram of the data-acquisition system.

2.7 Experimental Targets and Data Summary

Table 2.10 represents all the targets used in the present experiment together with obtained data with specific SKS current setting condition according to the experimental strategy. The data were taken in two separated experimental cycles also mentioned in the table 2.10. Specifications of the targets are summarized in table 2.11.
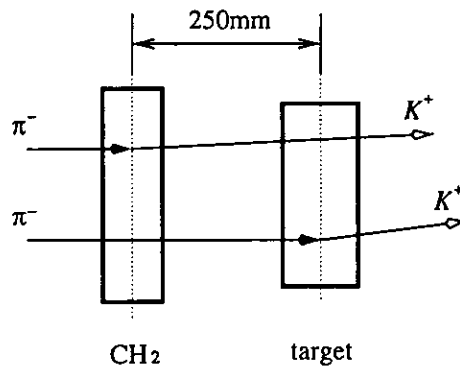
Figure 2.19: A schematic view of the target configuration

Table 2.10: Data summary of E438

(π^-, K^+) data

target(s)	SKS current [A]	irradiated π [$\times 10^9$]	cycle
CH$_2$&Si	210	15.8	Oct., 1999
CH$_2$&Si	210	86.5	Dec., 1999
CH$_2$&Si	272	228.7	Oct., 1999
CH$_2$&Si	272	16.0	Dec., 1999
CH$_2$&Si	320	101.6	Dec., 1999
CH$_2$&Ni	272	252.6	Dec., 1999
CH$_2$&In	272	352.3	Dec., 1999
CH$_2$&Bi	272	225.2	Oct., 1999
CH$_2$&Bi	272	120.7	Dec., 1999
CH$_2$	272	22.5	Oct., 1999
CH$_2$	272	24.8	Oct., 1999
CH$_2$	272	19.8	Dec., 1999
CH$_2$	272	19.6	Dec., 1999

(π^+, K^+) data

targets	SKS current [A]	irradiated π [$\times 10^9$]	cycle
CH$_2$&Si	272	25.3	Oct., 1999

Table 2.11: Specifications of the experimental targets.

target	size [cm]	thickness $\rho\delta x$ [g/cm^2]
CH$_2$	$20.0 \times 10.0 \times 1.0^T$	0.95
C	$8.8 \times 8.7 \times 1.0^T$	1.72
Si	$10.0 \times 7.5 \times 2.8^T$	6.53
Ni	$10.0 \times 10.0 \times 0.8^T$	7.16
In	$10.0 \times 10.0 \times 1.1^T$	7.93
Bi	$10.0 \times 10.0 \times 1.0^T$	9.74

As shown in table 2.10, two targets were placed in tandem where CH_2 target was almost always common to other nuclear targets. The CH_2 target was placed about 250mm upstream from the nuclear target. Figure 2.19 shows a schematic view of the target configuration. The calibration of the horizontal axis to determine the Σ^- binding energy threshold was one of the key point of the present experiment. The CH_2 target in this configuration was used for this purpose by referring the elementary process, $p(\pi^-, K^+)\Sigma^-$. Moreover, we could also monitor the stability of the whole system throughout the experiment by the elementary process both in energy scale mentioned above and in vertical scale(cross section). The detailed description of the calibration procedure is discussed in chapter 3. Moreover, from the CH_2 target we could also extract the C spectrum so as to discuss the mass number dependence of the Σ^- production cross section by the (π^-,K^+) reaction. However, some data were taken by putting only the CH_2 target in the same position in some intervals of the data taking period mainly to check the consistency of the calibration process as well as to check the elementary cross section as the energy-loss straggling in this case is sufficiently smaller. The SKS current setting of 272A could cover the momentum region of around Σ^- binding threshold sufficiently. Moreover, using three different SKS current settings namely, SKS 210A, SKS 272A and SKS 320A, data were taken on CH_2 and Si. These three settings together cover a very wider momentum acceptance of SKS which would enable us to understand the gross feature of the whole spectrum shape more quantitatively. The number of irradiated pions on different experimental target were decided to have almost the same number of yield in the missing mass scale of unbound region.

It is also important to mention here that some data were taken by using the (π^+,K^+) reaction on CH_2 and Si as shown in table 2.10. Beam momentum was fixed as 1.2 GeV/c which was same as (π^-,K^+) data in order to measure the inclusive (π^+,K^+) spectra on C and Si so as to compare the DWIA framework for the (π^+,K^+) reaction in the present experimental condition. The observed (π^+,K^+) spectra are presented in Appendix B.

Chapter 3

Data analysis

3.1 Outline

In this chapter, analysis procedures of the present experiment for the event reconstruction and to obtain the hypernuclear mass spectra from the raw data are described in detail.

The hypernuclear mass (M_{HY}) from the (π^-, K^+) reaction is obtained as a missing mass and is given as follows;

$$M_{HY} = \sqrt{(E_\pi + M_A - E_K)^2 - (p_\pi^2 + p_K^2 - 2p_\pi p_K \cos\theta_{\pi K})} \quad , \qquad (3.1)$$

where E_π and p_π are the total energy and momentum of a pion, E_K and p_K are those of a kaon, M_A is the mass of a target nucleus and $\theta_{\pi K}$ is the scattering angle of the reaction. Thus, we need to measure three kinematic variables, p_π, p_K and $\theta_{\pi K}$ through the momentum reconstruction event by event. The observed inclusive (π^-, K^+) spectra are presented in this thesis as function of the binding energy of the Σ^- hyperon(B_{Σ^-}) and is thus obtained as

$$B_{\Sigma^-} \equiv M_{A-1} + M_{\Sigma^-} - M_{HY} \quad , \qquad (3.2)$$

where M_{A-1} is the mass of a core nucleus at its ground state, and M_{Σ^-} is the mass of a Σ^- hyperon(1197.449 MeV/c^2). Figure 3.1 shows a schematic flow chart of the off-line analysis. First, a good (π^-, K) event was selected from the larger background event in the PIK trigger. An incident π^- was selected by using the time-of-flight between BH1 and BH2. At this stage a scattered K$^+$ was roughly selected by only using the TOF and LC counters information. Then, the π^- momentum and the K$^+$ momentum were reconstructed from the track information of BDC's and SDC's, respectively. In the tracking process, first, straight-line track candidates were defined both at the entrance and the exit of the spectrometer system. Then, the combination of the straight-line tracks which gave the least chi-square in the momentum reconstruction was assigned as the best track candidate. A third-order transport matrix was used in the beam spectrometer for the beam momentum construction, while, for the scattered momentum reconstruction in the SKS, a precisely measured magnetic field map was used. Then, the vertex
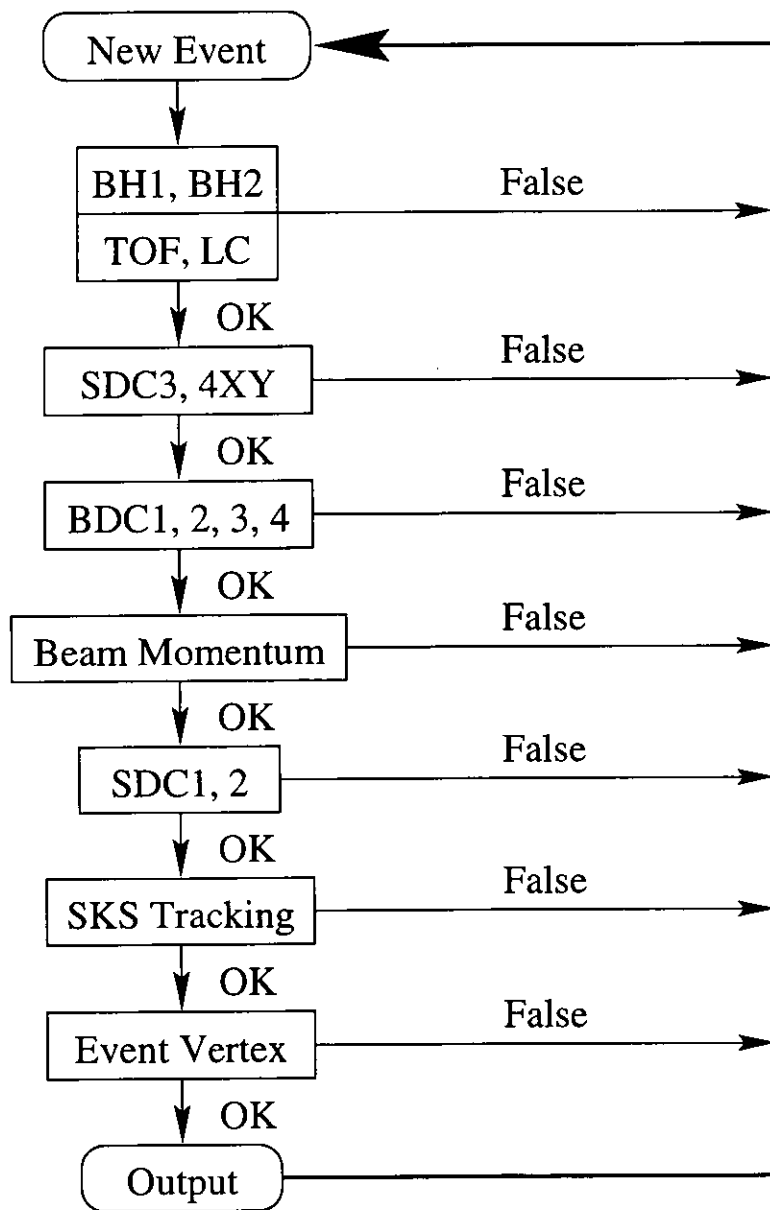
Figure 3.1: Flow chart of a (π^-, K^+) event reconstruction

point where the (π^-, K^+) reaction took place was obtained from the π^- and K^+ trajectories. Finally, by using the time-of-flight information between BH2 and TOF and the reconstructed momentum, identification of K^+ was carried out precisely.

The hypernuclear mass spectra obtained by the present analysis could be characterized in terms of the precision of the horizontal(excitation energy) scale, vertical(cross section) scale and also by the background level. These factors are also discussed in this chapter.

3.2   Beam Momentum reconstruction

As stated earlier, the beam momentum was reconstructed from the BDC's information. The detail procedure is as follows. First, straight tracks were defined locally at the entrance and exit of the QQDQQ system by BDC1·2 and BDC3·4 ,respectively, by using the least-squares method. For multi-hit events, a pair-plane hit condition was required, which was equivalent to solving the left/right ambiguity. Those straight tracks were connected using a third order transport matrix [1]. Then the particle momentum was determined by minimizing the following reduced χ^2 value. The χ^2 value of each track is defined as

$$\chi^2_{K6} = \frac{1}{n-5}\left(\sum_{i=1}^{12} H_i\left(\frac{P_i - f_i(\vec{X}_{in})}{w_i}\right)^2 + \sum_{i=13}^{24} H_i\left(\frac{P_i - g_i(\vec{X}_{out})}{w_i}\right)^2\right),$$

$$n = \sum_{i=1}^{24} H_i,$$

$$H_i = \begin{cases} 1 & \text{if } i\text{-th plane had a hit} \\ 0 & \text{if } i\text{-th plane had no hit}, \end{cases}$$

$$\vec{X}_{out} = \mathcal{M}(\vec{X}_{in}, \delta),$$

where P_{in} and w_i denote the hit position and resolution of the i-th plane in BDC. The estimated positions with the transport matrix at the i-th plane are $f_i(\vec{X}_{in})$ and $g_i(\vec{X}_{out})$, where $\vec{X}_{in}$ and $\vec{X}_{out}$ are the horizontal and vertical positions (x, y) and their derivatives $(\frac{dx}{dz}, \frac{dy}{dz})$ at the entrance and exit of the QQDQQ system. The operator $\mathcal{M}$ denotes the transport matrix which combines the $\vec{X}_{in}$ and $\vec{X}_{out}$. For multi-hit events, the only combination which gave the least χ^2 was chosen. Figure 3.2 shows a typical χ^2 distribution for a 1.2-GeV/c π^- beam. The tracks whose χ^2 were less than 20 were accepted as good events. The accepted region is indicated by the arrow.

Typical momentum distribution for the 1.2-GeV/c π^- beam is shown in figure 3.3. The momentum bite was typically ± 3 %.

41
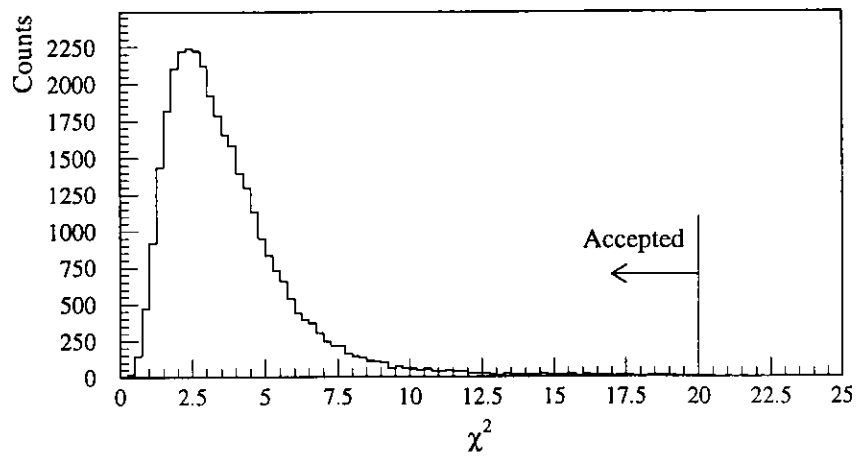
Figure 3.2: Typical distribution of χ^2_{K6} for a 1.2 GeV/c π^+ beam.
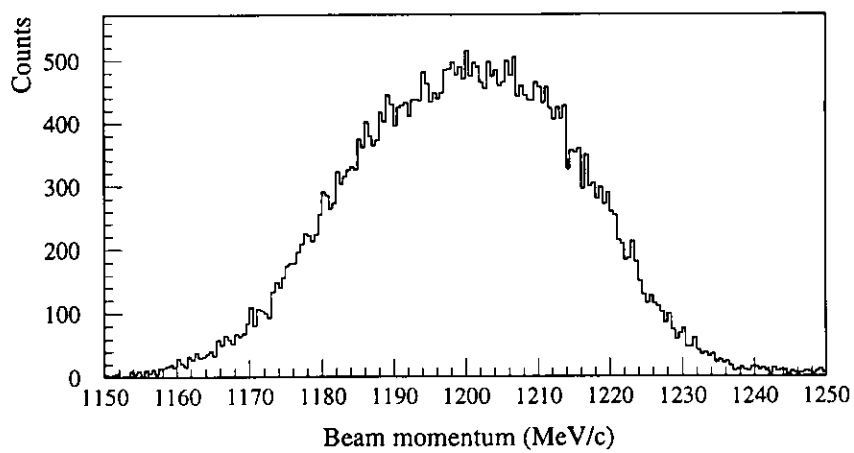
Figure 3.3: Typical distribution of the momentum for a 1.2 GeV/c π^- beam.

3.3 Scattered Particle momentum reconstruction

The momentum of a scattered particle was reconstructed from the SDC data.

Using the least-squares method, straight tracks were defined locally at the entrance and exit of the SKS magnet by SDC1·2 and SDC3·4 , respectively. Since the pair-plane hit condition was no use in case the trajectory had a large angle to the chamber planes, all combinations of the left/right ambiguity were examined in finding the SDC1·2 track. For multi-hit events, all possible combinations were examined, and events whose chi-squares were less than 10 were accepted.

Then, the momentum of a scattered particle was determined by reconstructing a trajectory from the hit positions by the Runge-Kutta tracking method for particle by particle using the measured magnetic field maps [40]. The magnetic field maps had been measured at various current settings with an accuracy of 10^{-4} using high-precision hall probes [1]. The trajectory and momentum were optimized by minimizing the following χ^2 value with iteration. For multi-track events, the only combination which makes the least χ^2 was chosen. The χ^2 value of each track was defined as

$$\chi^2_{SKS} = \frac{1}{n-5} \sum_{i=1}^{n} \left(\frac{x_i^{tracking} - x_i^{data}}{w_i} \right)^2 , \tag{3.3}$$

where n is the number of the chamber planes with a hit, $x_i^{tracking}$ and x_i^{data} are hit positions on the i-th plane in the tracking and the data, respectively, and w_i is the position resolution of the i-th hit plane. The convergence criterion in the iteration is $\delta\chi^2 = (\chi^2_{k+1} - \chi^2_k)/(\chi^2_k) < 10^{-3}$, where k is the number of iterations and χ^2_k is the tracking χ^2 value for the k-th iteration. Figure 3.4 shows a typical SKS χ^2 distribution from the CH_2&$Si(\pi^-,K^+)$ data. In the present analysis, tracks whose χ^2 were less than 60 were accepted as good tracks considering high efficiency and a good momentum resolution as well as sufficient decay background rejection.

3.4 Particle identification in the SKS

The first priority in the off-line analysis was to select the good PIK event from the huge background mainly came from the fast protons which fired LC. The pions were well suppressed in the trigger level by AC1 and AC2. These background particles were roughly identified by using ADC's or TDC's of TOF and LC. In order to reduce the required CPU time in the Runge-Kutta tracking routine , TDC cut of both TOF and LC were applied in the first stage of the off-line analysis.

After the tracking, the mass of a scattered particle M_{scat} was calculated as

$$M_{scat} = \frac{p}{\beta}\sqrt{1 - \beta^2} , \tag{3.4}$$

where β is the velocity of a scattered particle obtained from the time-of-flight and the flight path length between BH2 and TOF, and p is the momentum obtained from the event reconstruction. Figure 3.5 shows a typical mass distribution of

43
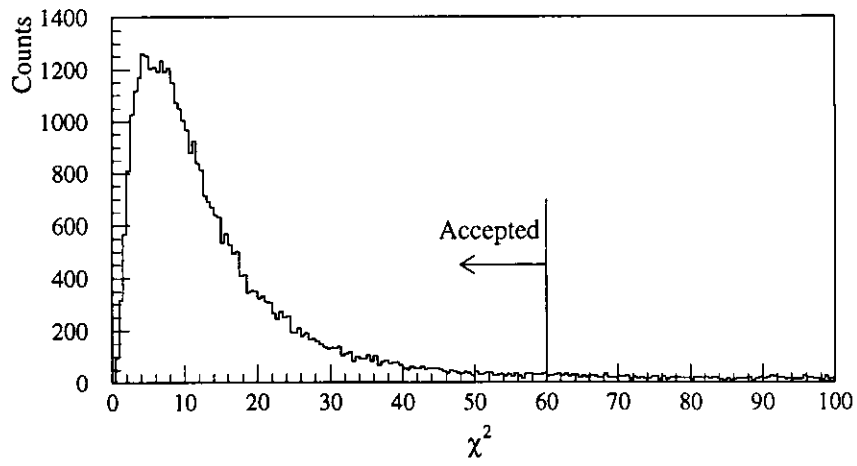
Figure 3.4: Typical distribution of χ^2_{SKS} for the SKS tracking
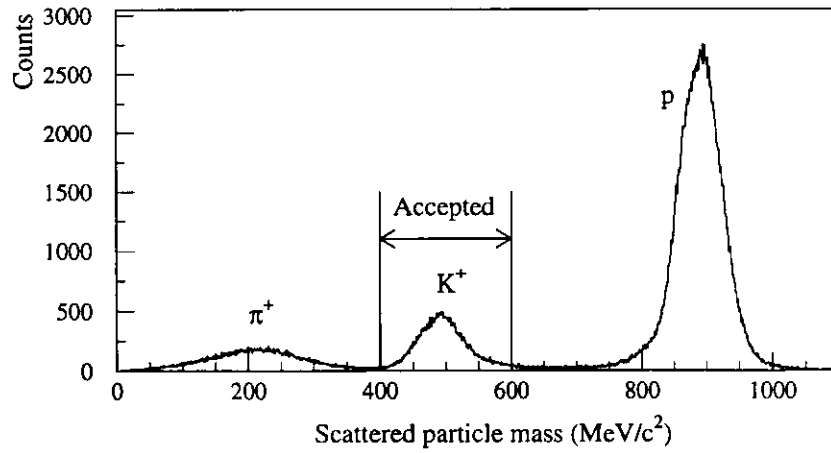
Figure 3.5: Typical mass spectrum of scattered particles from the CH_2&Si data.

44

scattered particles for the $CH_2\&Si(\pi^-,K^+)$ data obtained after a χ^2_{SKS} analysis explicitly. Kaons are clearly separated from the pions and protons.

3.5 (π^-,K^+) event vertex and scattering angle

The scattering angle and event vertex were obtained from a local straight track in BDC3·4 for the incoming pion and a track obtained in the momentum reconstruction of the scattered particle in SKS. The horizontal and vertical angular resolutions in r.m.s. were 0.188° and 0.319°, respectively as shown in figure 3.6. The horizontal resolution was comparatively better than the vertical one due to the special wire configuration of the drift chambers.

Figure 3.7 shows a typical distribution of the scattering angle obtained from the $CH_2\&Si(\pi^-,K^+)$ data. To reject the background events coming from the BH2 counter as well as to improve the Z-projected vertex resolution, we selected the scattering angle greater than 4 degrees as good events as indicated by an arrow in the figure.

Figure 3.8 shows a scatter plot between the Z-projection of the event vertex and the scattering angle without the scattering angle cut from the $CH_2\&Si(\pi^-,K^+)$ data . The Z-axis is defined as the beam direction. It is clearly seen in the figure that the events scattered at the two targets, as well as in the BH2 counter can be clearly identified. However, the Z-vertex resolution around the forward scattering angle region was not good as seen in the figure. Then, by applying the scattering angle cut ($\theta \geq 4°$) the resolution was improved very much as shown in figure 3.9. The arrows indicated in the figure 3.9 were the accepted regions of the CH_2 and Si events in the analysis.
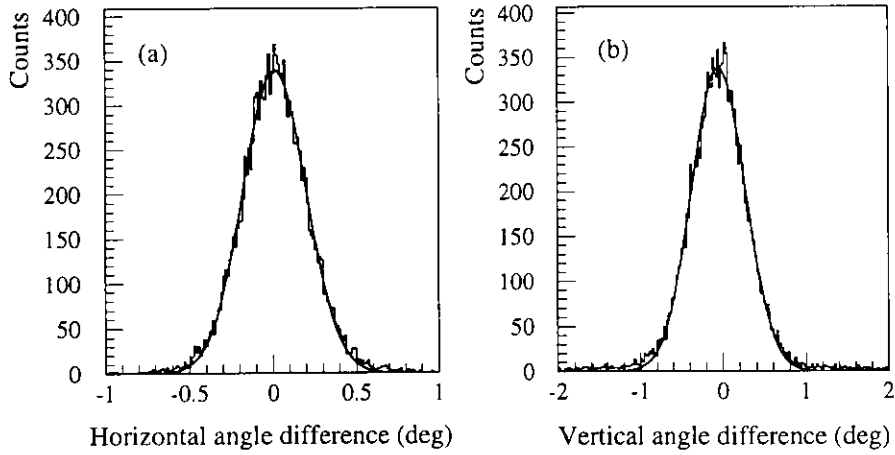
Figure 3.6: Typical horizontal(a) and vertical(a) angular resolutions measured with a π^+ 0.72 GeV/c beam through run without targets. The horizontal angular resolution in rms is $0.188°$ and the vertical one is $0.319°$.
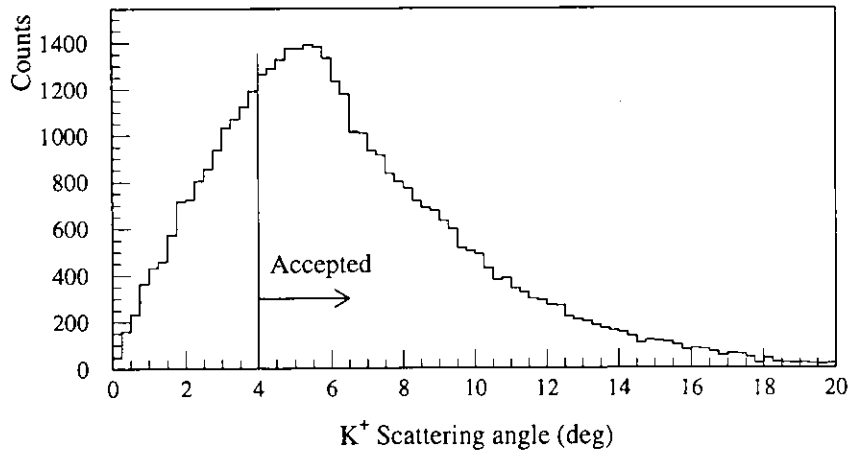
Figure 3.7: Typical distribution of the scattering angle for the $CH_2\&Si(\pi^-,K^+)$ data
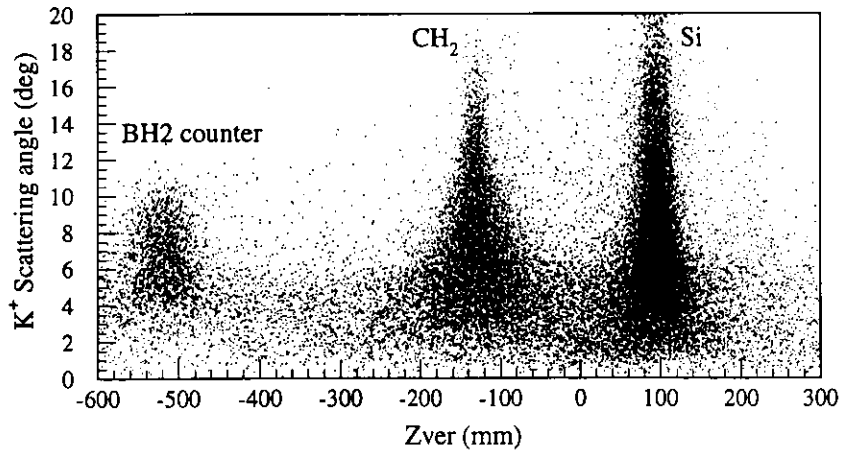
Figure 3.8: Scatter plot between K^+ scattering angle and the Z-projection of the event vertex
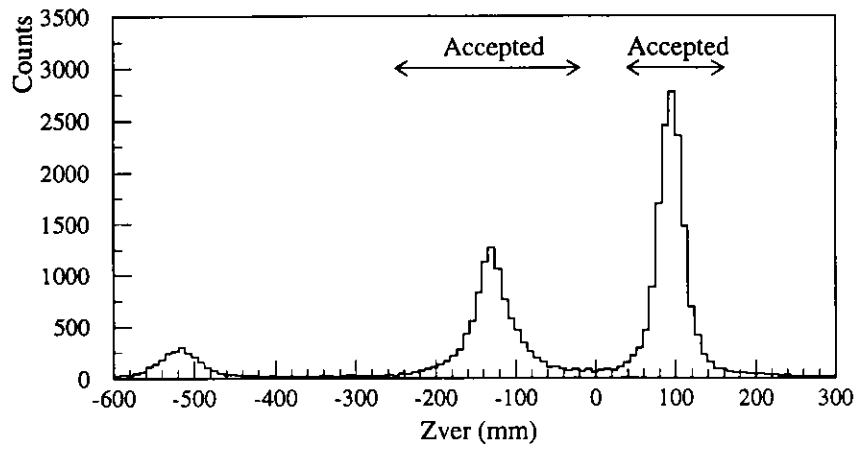
Figure 3.9:Z-projection of the event vertex for the CH2&Si(π^-, K^+) data with a scattering angle cut($\theta \geq 4°$)

3.6 Energy scale calibration

The calibration of horizontal axis is one of the very important point of the present experiment. For that purpose, the elementary process, $p(\pi^-, K^+)\Sigma^-$ from the CH_2 target is used so that elementary peak position stands always at $m_{\Sigma^-} - m_p = 259.177 \pm 0.029$ MeV/c^2 in the missing mass scale [41]. The calibration process mainly consists of two parts:

First, to estimate the momentum loss of incident pions and outgoing kaons in the target(s) beam through runs with and without target was taken with different momenta of π^+ beam and second, correlations between scattered momenta and incident angles are needed to be solve in order to determine the SKS offset values.

3.6.1 π^+ beam through run

In the beam through run, π^+ beam was conducted through the SKS magnetic field both with and without a target. The beam through runs were taken in several periods of the whole experimental cycle mainly when the experimental target was changed as well as in any other change of the experimental condition. Table 3.1 shows such a list of the beam through runs taken in the present experiment. Beam through run with target was taken with each experimental target individually. For the target energy loss estimation, beam through data of momentum 0.72 GeV/c taken with and without a target were used. Another purpose of the beam through runs without a target was to calibrate the hodoscope parameters(ADC's and TDC's) where several beam momenta were chosen to cover the overall region of the SKS counters uniformly to optimize the momentum resolution of our experimental setup.

The beam through run for the 1.2-GeV/c beam could not be carried out because of the limit of the SKS magnetic field.

3.6.2 Target energy loss and straggling

The difference of the beam momentum measured by the QQDQQ spectrometer system and the SKS with a target reflects the energy loss in the target. However, without a target that reflects the momentum resolution of the whole experimental equipment. Beam through data of momentum 0.72 GeV/c with and without target were used for those purposes.

Figure 3.10 shows the momentum difference $dP = P_{K6} - P_{SKS}$ from without(a) and with(b) the silicon target(6.53 g/cm^2) for a 0.72-GeV/c π^+ beam, where P_{K6} is momentum from the beam spectrometer tracking and P_{SKS}, that from the SKS tracking. A fitting with a Gaussian function, figure 3.10(a) gives a value of $\sigma_{dP} = 0.98 \pm 0.01$ MeV/c. The energy loss was obtained as the shift of the centroid.

Figure 3.11 shows a relation between the observed energy loss values and the target thickness where, the obtained values are compared with the calculated mean
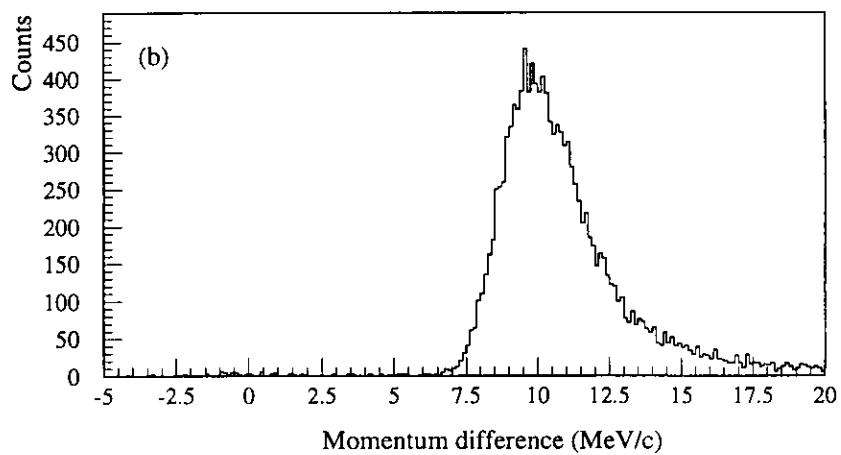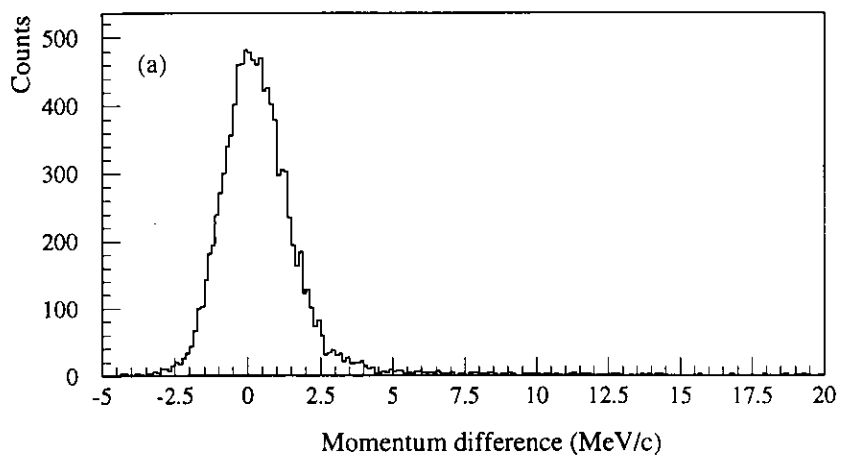
Figure 3.10: Distributions of the momentum difference between the two spectrometers without(a) and with(b) the silicon target(6.53 g/cm^2) for a 0.72 GeV/c π^+ beam. In (b), the centroid is shifted and the width is widen because of the target energy loss and its straggling.

and most probable energy loss values. The mean energy loss is calculated by the Bethe-Bloch formula and the the most probable energy loss is calculated by using Landau's distribution. Experimental mean and most probable energy loss values are obtained from the mean and and peak value of the energy loss distribution. The calculated mean energy loss values are agreed well with the observed mean energy values. Hence, we used mean energy loss values in our analysis.

Energy loss obtained with various targets are summarized in the table 3.2 where different calculations are also shown for comparison.

In case of our calculation for the π^- beam of 1.2 GeV/c and the scattered kaon, the reaction point was assumed at the center of the target. Then, the momentum loss of pion was calculated by scaling the observed momentum loss of 0.72 GeV/c π^+ beam to the ratio of the averaged energy-loss values at the beam momentum(1.2 GeV/c) and the beam through run momentum(0.72 GeV/c). Kaon energy loss in the target was calculated by the Bethe-Bloch formula.

Table 3.1: Beam through data taken in the E438 experiment

	QQDQQ [GeV/c]	SKS [mode]
with targets	0.720	2.2 T
without target	0.720	2.2 T
without target	0.756	2.2 T
without target	0.774	2.2 T
without target	0.792	2.2 T
without target	0.810	2.2 T
without target	0.828	2.2 T
without target	0.684	2.2 T
without target	0.666	2.2 T
without target	0.648	2.2 T
without target	0.630	2.2 T
without target	0.90	2.7 T
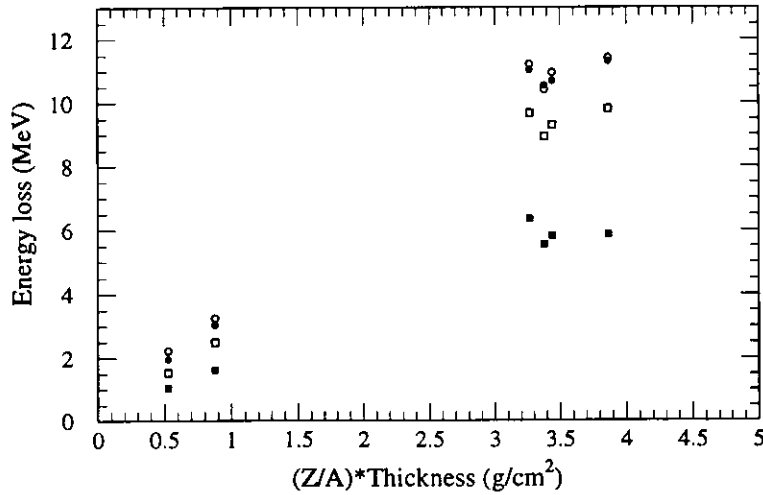
Figure 3.11: $\frac{Z}{A} \cdot \rho dx$ dependence of the energy loss. Empty circles and empty boxes are the observed mean and most probable energy loss, respectively. Black circles and black boxes are those from the calculation. The calculated mean energy loss values were obtained by using Bethe-Bloch formula, which agreed well with the observed mean energy loss values.

Table 3.2: Summary of the energy and momentum loss estimation for 0.72 GeV/c π^+ beam. 'b.thr' indicates the present beam through data. 'ene.loss' means the energy loss in the target, 'mom.loss' is the momentum loss and 'm.p.' is the most-probable loss. The quoted errors are statistical. Calculated mean energy loss values were obtained by using Bethe-Bloch formula [42].

target	ene.loss	(m.p.)	ene.loss	(mean)	mom.loss	(m.p.)	mom.loss	(mean)
	b.thr	calc	b.thr	calc	b.thr	calc	b.thr	calc
	[MeV]	[MeV]	[MeV]	[MeV]	[MeV/c]	[MeV/c]	[MeV/c]	[MeV/c]
CH$_2$	1.55 ± 0.02	1.05	2.24 ± 0.02	1.98	1.71 ± 0.02	1.07	2.27 ± 0.02	2.02
C	2.50 ± 0.02	1.62	3.25 ± 0.03	3.04	2.50 ± 0.02	1.65	3.30 ± 0.03	3.10
Si	9.67 ± 0.10	6.353	11.22 ± 0.11	11.04	9.97 ± 0.10	6.472	11.42 ± 0.12	11.25
Ni	9.30 ± 0.10	5.802	10.95 ± 0.12	10.69	9.60 ± 0.10	5.92	11.14 ± 0.12	10.89
In	8.93 ± 0.10	5.545	10.41 ± 0.11	10.54	9.05 ± 0.10	5.65	10.59 ± 0.11	10.74
Bi	9.80 ± 0.13	5.856	11.41 ± 0.15	11.32	10.00 ± 0.13	5.966	11.61 ± 0.15	11.53

3.6.3 Momentum correction

The expected peak position for the elementary process, $p(\pi^-, K^+)\Sigma^-$ is at 259.177 MeV as explained earlier. The missing mass spectrum for the elementary process in the CH_2 target from a typical CH_2&Si data is shown in the figure 3.12, where target energy loss was not taken into account. As a result, the elementary peak position was not found to the expected position and moreover a small satellite peak can be seen appeared close to the prominent peak. These events were found to be come for larger scattering angles from the CH_2 target which did not pass through the downstream target (here Si) as also can be seen in the figure 3.13(a). As a result, these events from the CH_2 target did not suffered the energy loss like other events which passed through the Si target. At first, these two separate events were identified and different energy loss were taken into account for the corresponding event. Later, in addition to the target energy loss, the measured beam momentum as well as scattered momentum were also corrected by the following ways;

Scattered kaon momentum correction

In order to optimized the energy resolution, in addition to the energy loss effect higher order correlations were removed by looking scatter the plot between missing mass energy from the elementary process and $\frac{dx}{dz}$ or $\frac{dy}{dz}$ of scattered kaon's as shown in figure 3.13, where $\frac{dx}{dz}$ and $\frac{dy}{dz}$ are the derivatives of the horizontal and vertical positions, respectively at the target.

In the SKS, the scattered momentum correction was made with second-order polynomials in $\frac{dx}{dz}$ and $\frac{dy}{dz}$ together with the energy loss correction and can be expressed by the following equation;

$$
\begin{aligned}
P_{SKS}^{cor} \;=\; & P_{SKS}^{track} + dP_{SKS}\sqrt{1.+\left(\frac{dx}{dz}\right)_{SKS}^2+\left(\frac{dy}{dz}\right)_{SKS}^2} \\
& +a\cdot\left(\frac{dx}{dz}\right)_{SKS}+b\cdot\left(\frac{dx}{dz}\right)_{SKS}^2+c\cdot\left(\frac{dy}{dz}\right)_{SKS}+d\cdot\left(\frac{dy}{dz}\right)_{SKS}^2+e
\end{aligned}
$$
(3.5)

where P_{SKS}^{cor} is the corrected kaon's momentum which represents the kaon's momentum at the reaction point. P_{SKS}^{track} and dP_{SKS} are the reconstructed kaon's momentum and the momentum loss, respectively. x, y and z denote the horizontal, vertical and the beam direction at the reaction point, respectively. a, b, c and d are the correlation coefficients and e is the energy offset determined finally. After taking into account the target energy loss correctly and by solving the correlations, the two elementary peaks were found to be combined into one and the peak position was found to be at the expected position (figure 3.13(b)). Values of these coefficients were kept same with all combination of data set and the precision of the energy scale was found to be $\pm$ 0.10 MeV. The obtained elementary peak position for each set of data is presented in section 3.6.4.

Beam momentum correction

The beam momentum was corrected by the the following equation;

$$P_{K6}^{cor} = P_{K6}^{track} - dP_{K6}\sqrt{1. + \left(\frac{dx}{dz}\right)_{K6}^2 + \left(\frac{dy}{dz}\right)_{K6}^2} \qquad (3.6)$$

where P_{K6}^{cor} is the corrected pion's momentum which represents the pion's momentum at the reaction point. P_{K6}^{track} is the reconstructed momentum by the beam spectrometer and dP_{K6} is the estimated momentum loss.
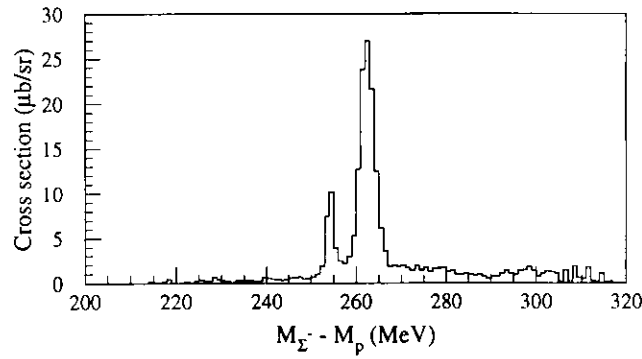
Figure 3.12: Elementary distribution from the CH_2 target (CH_2&Si data) without momentum loss correction. The small satellite peak seen in the figure was from the events with larger scattering angles from the CH_2 target which did not not pass through the Si target. Events from the C target in CH_2 can be seen scattered at the lower part of the histogram.
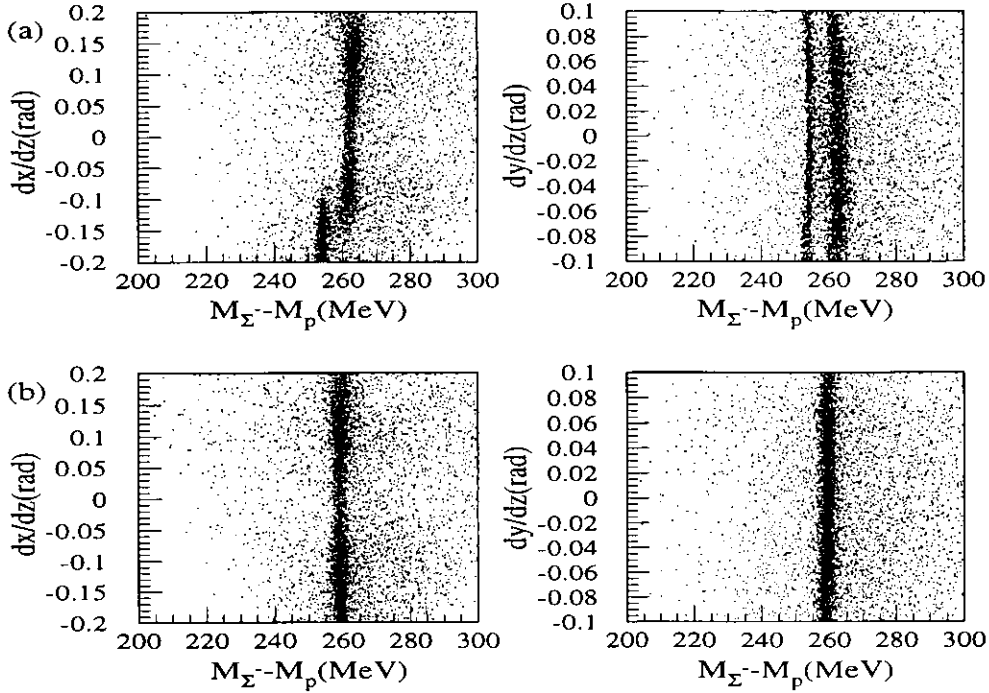
Figure 3.13: Scatter plots between the elementary process($m_{\Sigma^-} - m_p$) and $\frac{dx}{dz}$ or $\frac{dy}{dz}$ of scattered kaons for the CH_2&Si data without(a) and with(b) SKS momentum correction, where $\frac{dx}{dz}$ and $\frac{dy}{dz}$ are the derivatives of the horizontal and vertical positions at the target, respectively.

3.6.4 Result of the energy scale calibration

Combination of all those procedures mentioned above for the energy scale calibration gave calibrated energy scale spectra for the elementary process with all combinations of target(s) setup. In figures 3.14, 3.15, 3.16, 3.17, 3.18 and 3.19 results of the energy scale calibration are shown. In all cases, the scattering angle cut was fixed to be 4° - 8°. The elementary peak position was always obtained to the expected position with all combinations as well as in two data taking cycles. The obtained energy resolution is sufficient to discuss the spectra from all nuclear targets rather fairly even near the Σ^- binding threshold as the depth of the imaginary part of the Σ-nucleus potential is supposed to be more than 7 MeV [28].

The elementary peak position and peak width with all setup are summarized in table 3.3.
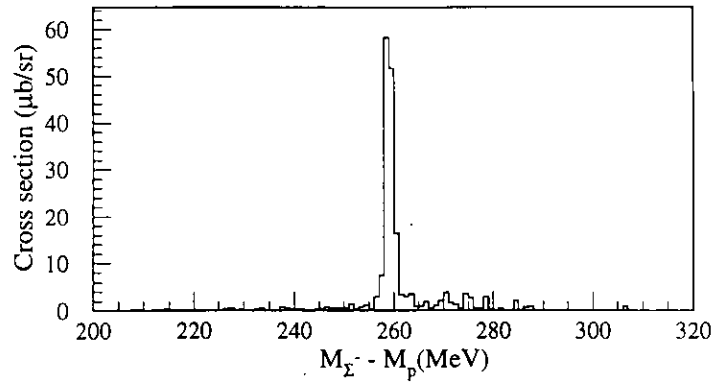
Figure 3.14: The peak of the elementary process from the CH_2 only data. The peak position was found to be at : $259.13 \pm .10$ MeV and the width (FWHM) was 1.93 ± 0.08 MeV. Events coming from the C target in CH_2 are seen at the lower part of the histogram.
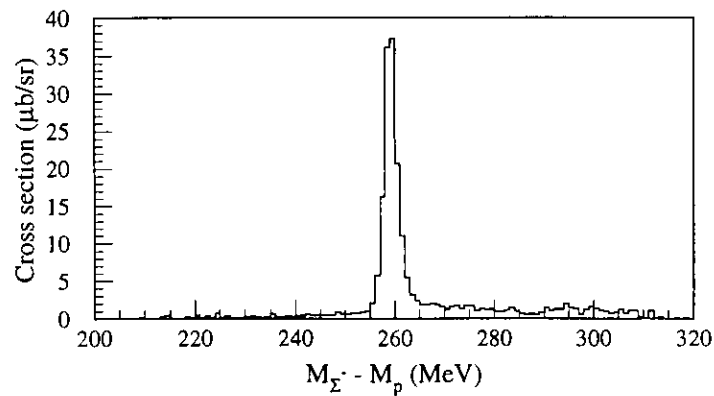
Figure 3.15: The peak of the elementary process from the $CH_2\&Si$ data(SKS 210A).
The peak position was found to be at 259.23 ± 0.13 MeV with a width(FWHM) of 3.31 ± 0.33 MeV.
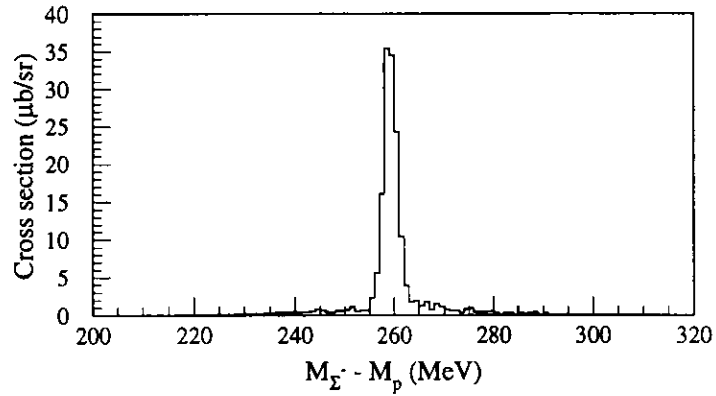
Figure 3.16: The peak of the elementary process from the CH$_2$&Si data(SKS 272A).
The peak position was found to be at 259.27 ± 0.14 MeV with a width (FWHM) of 3.32 ± 0.29 MeV.
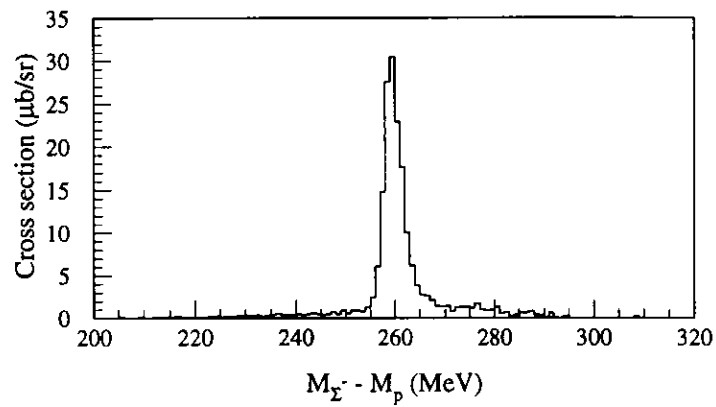
Figure 3.17: The peak of the elementary process from the CH$_2$&Ni.
The peak position was found to be at 259.45 ± 0.19 MeV with a width (FWHM) of 4.43 ± 0.42 MeV.
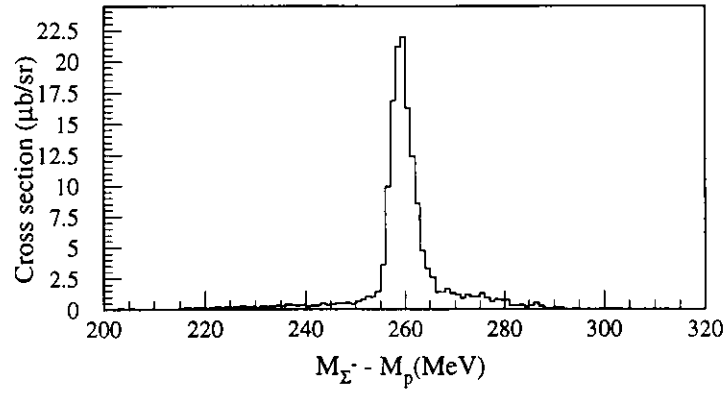
Figure 3.18: The peak of the elementary process from the CH_2&In.
The peak position was found to be at 259.39 ± 0.24 MeV with a width
(FWHM) of 4.79 ± 0.50 MeV.
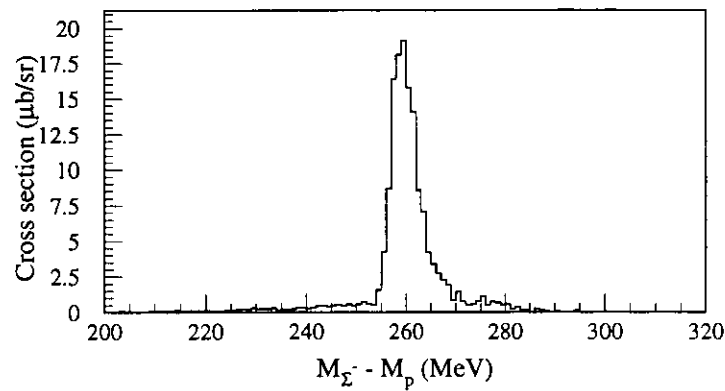
Figure 3.19: The peak of the elementary process from the CH_2&Bi.
The peak position was found to be at 259.62 ± 0.26 MeV with a width
(FWHM) of 5.16 ± 0.53 MeV.

Table **3.3**:Elementary peak position and energy resolution from the different sets of data. The quoted errors are statistical only.

Expected peak position $m_{\Sigma^-} - m_p = 259.177 \pm 0.029$ MeV/c^2 [41]

Data	Elementary peak position (MeV)	Energy resolution(FWHM) (MeV)
CH$_2$ only	259.20 $\pm$ 0.10	2.06 $\pm$ 0.20
CH$_2$&Si(SKS 210A)	259.23 $\pm$ 0.13	3.31 $\pm$ 0.33
CH$_2$&Si(SKS 272A)	259.27 $\pm$ 0.14	3.32 $\pm$ 0.29
CH$_2$&Ni	259.45 $\pm$ 0.19	4.44 $\pm$ 0.42
CH$_2$&In	259.39 $\pm$ 0.24	4.79 $\pm$ 0.50
CH$_2$&Bi	259.62 $\pm$ 0.26	5.16 $\pm$ 0.53

3.6.5 Linearity of the SKS momentum

In order to examine the linearity of the SKS momentum over a wider momentum region, π^+ beam through data without a target were taken at the SKS current setting of 272A(2.2T) for several central beam momenta of 630 MeV/c to 830 MeV/c. In table 3.1, typical beam through data taken in the present experiment are summarized. In the beam through data without a target, we assumed that the central momentum of the beam spectrometer was exactly proportional to the magnetic fields of the beam line magnets. Figure 3.20 shows the mean value of the momentum difference between the two spectrometers as a function of the central momentum of the beam spectrometer. It was found that the linearity was kept within ± 0.072 MeV/c in the momentum range.
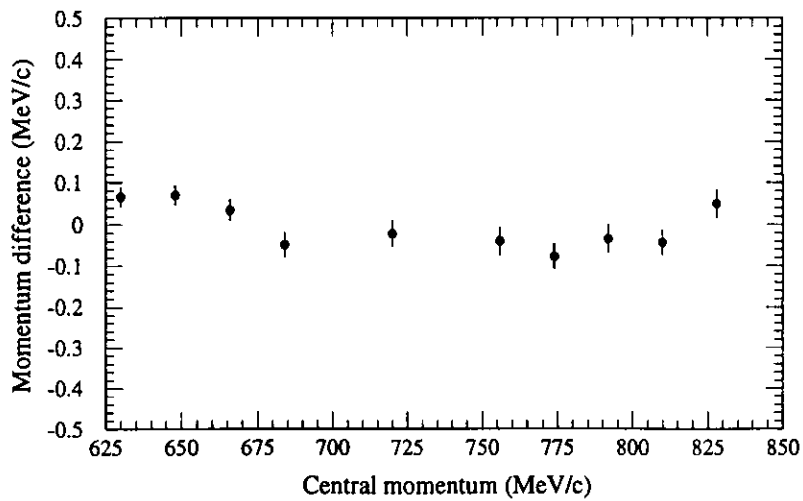
Figure 3.20: Mean value of the momentum difference between the SKS and the beam spectrometer as a function of the central momentum of the beam spectrometer.

3.7   Cross section

In order to obtain the vertical axis in terms of cross section, (i) experimental efficiencies and (ii) SKS acceptance should be estimated. In this section brief procedures of the efficiency estimation together with SKS acceptance estimation are described. In table 3.4, definition of each experimental efficiency factor together with other constant variables are listed.

59

Table 3.4: Definition of experimental efficiency factors and constant.

variable or constant	name	typical values
x	hit position	—
i	i-th run	—
k	k-th event	—
θ	scattering angle of the event	—
p	reconstructed momentum of the event	—
Y_k	yield	—
N_{beam}	scaler count of the $BEAM$ trigger	—
I_i	number of irradiated π^-	—
A	mass number of the target	—
(ρx)	target thickness in g/cm^2	—
N_A	Avogadro's number	—
ϵ_{DAQ}	DAQ efficiency	$80.4 \pm 0.1\%$
ϵ_{BDC}	BDC efficiency	$88.9 \pm 1.6\%$
$\epsilon_{K6track}$	K6 tracking efficiency	$96.5 \pm 1.4\%$
ϵ_{SDC12}	SDC12 efficiency	$92.2 \pm 1.2\%$
ϵ_{SDC34}	SDC34 efficiency	$85.2 \pm 1.7\%$
$\epsilon_{SKStrack}$	SKS tracking efficiency	$92.2 \pm 2.9\%$
ϵ_{vertex}	Z vertex cut efficiency	$92.9 \pm 2.8\%$
ϵ_{PID}	PID cut efficiency	$99.4 \pm 1.6\%$
$\epsilon_{TOF\ LC\ mul.cut}$	TOF-LC multiplicity cut efficiency	$98.7 \pm 1.3\%$
f_{decay}	K^+ decay factor	$\sim 42\%$
$d\Omega\,(\theta,\ p)$	simulated solid angle	—
f_{AC}	Accidental veto factor of AC	$99.1 \pm 0.2\%$
f_{beam}	beam normalization factor	$89.7 \pm 1.5\%$

3.7.1 Efficiency estimation

In this section, brief procedures of the efficiency estimation are described.

Data-acquisition efficiency

The dead time of the data-acquisition system caused a finite efficiency(ε_{daq}) of the data-acquisition. The data-acquisition efficiency was obtained by the ratio of the number of events accepted by the data-acquisition system to that of triggers. The typical value of ϵ_{DAQ} was $80.4 \pm 0.1\%$ for the CH_2&Si data.

Beam normalization factor

The beam normalization factor f_{beam} represents the fraction of π^- beam out of N_{beam}. By the excellent performance of the eGC, the e^- contamination was rejected with an efficiency of better than 99% in the trigger level. The proton contamination was also rejected by requiring a good timing coincidence between BH1 and BH2. However, muons in the beam, which are the decay products of pions, could not be separated from pions. Here, we assumed it as 6.2% which was found for the 1.05 GeV/c π^+ beam in previous E369 experiment [2]. Since the β of 1.2 GeV/c π^- is very close to that of 1.05 GeV/c π^+, it can also be use in our case.

The accidental coincidence rate f_{acc}, between BH1 and BH2 was estimated by using the *BEAM* trigger events mixed in the (π^-, K^+) data and was defined as $(N_{beam} - N_{BH1\cdot2})/N_{beam}$, where $N_{BH1\cdot2}$ is the number of events for which the time of flight between BH1 and BH2 are proper for π^-. f_{acc} was estimated by using the *BEAM* trigger events mixed in the (π^-, K^+) data. Typical value of f_{acc} was $4.4 \pm 1.7\%$ for CH_2&Si data with SKS 272A setting. Thus the value of $f_{beam} = (1 - f_\mu) \cdot (1 - f_{acc})$ was found to be $89.7 \pm 1.5\%$.

BDC efficiency and K6 tracking efficiency

The efficiency in the beam momentum reconstruction was estimated as a ratio of the number of events accepted as a good trajectory to that of good beam particles defined with BH1 and BH2, $N_{beam} \cdot (1 - f_{acc})$. It is composed of the BDC efficiency ϵ_{BDC} and the K6 tracking efficiency $\epsilon_{K6track}$. They were estimated by using the *BEAM* trigger events mixed in the (π^-, K^+) data. The BDC efficiency is the total efficiency to get straight tracks at the entrance and exit of the QQDQQ magnet, which was found to be $88.9 \pm 1.6\%$ for the CH_2&Si data. The K6 tracking efficiency is the analysis efficiency to reconstruct a particle trajectory in the beam spectrometer, which was typically $96.5 \pm 1.4\%$.

TOF and LC multiplicity cut efficiency

In the analysis of the trigger counters in the SKS, events with more than two hits on TOF and LC were rejected in order to reduce background. A part of the (π^-, K^+) events were also rejected by this cut. The efficiency of this cut was estimated

from the ratio of the accepted events with and without multiplicity cut and was thus obtained to be $98.7 \pm 1.3\%$ for the CH_2&Si data.

The intrinsic detection efficiency of TOF and LC was over 99% in the previous experiments ([2]). Thus we took it as 1.

AC1·2 accidental veto factor

Because of high counting rate of AC1·2, some of the PIK triggers were killed accidentally. The coincidence width between AC1·2 and $BEAM \times TOF \times LC$ was 56 ± 5 nsec, which is the dead time in the PIK trigger. Therefore, the accidental veto rate was estimated as $1 - f_{AC} = R_{AC} \times (56 \pm 5) \times 10^{-9}$, where R_{AC} is the single counting rate of AC1·2 and its typical value was 15×10^5. Thus the value of f_{AC} was obtained to be $99.1 \pm 0.2\%$.

SDC1·2 efficiency

The SDC1·2 efficiency, ϵ_{SDC12}, is the total efficiency to get straight tracks at the entrance of the SKS magnet. It was estimated in a similar way as that of BDC's by using the $BEAM$ trigger events mixed in the (π^-, K^+) data. For the estimation, tracks which should pass through the effective area of SDC1·2 were defined by extrapolating from straight tracks defined by BDC3·4. In SDC1·2, the beam counting rate per one wire was quite high, because the beam was focused at the target position. Therefore a degradation of the efficiency near the beam spot was observed. Figure 3.21 shows the efficiency as a function of the incident positions, X_{in} and Y_{in} estimated for the CH_2&Si data. It has a dependence on the horizontal position X_{in}. A solid curve was obtained by fitting the position dependence of efficiency and was used in the analysis for the event by event correction as shown in equation 3.8. The value of $\epsilon_{SDC1·2}$ averaged on the incident position was typically $92.8 \pm 1.2\%$.
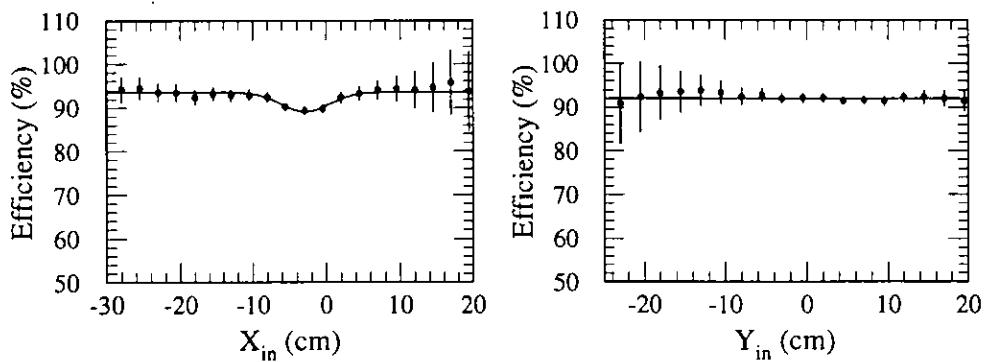
Figure 3.21:Typical SDC1·2 efficiency. Left: horizontal position (X_{in}), right: vertical position (Y_{in}).

SDC3-4 efficiency

The SDC3-4 efficiency, $\epsilon_{SDC3\text{-}4}$, is the total efficiency to get straight tracks at the exit of the SKS magnet. It was estimated by using the $(\pi^-, p)X$ events in the PIK trigger, since the proton will not decay in flight. For the estimation, tracks which should pass through the effective area of SDC3-4 were reconstructed by using TDC and ADC information of TOF and four sense wire layers of SDC4X·Y(those 4 layers of SDC4X·Y were not used in the good event reconstruction). Figure 3.22 shows the efficiency as a function of the incident positions for the CH_2&Si data. It has a strong dependence on the horizontal position, X_{out}. It was caused by some noisy channels in the x and x' planes of SDC3. The solid curve was obtained by proper fitting and was used in the analysis for the event by event correction. Typical SDC3-4 efficiency was $85.2 \pm 1.7\%$.
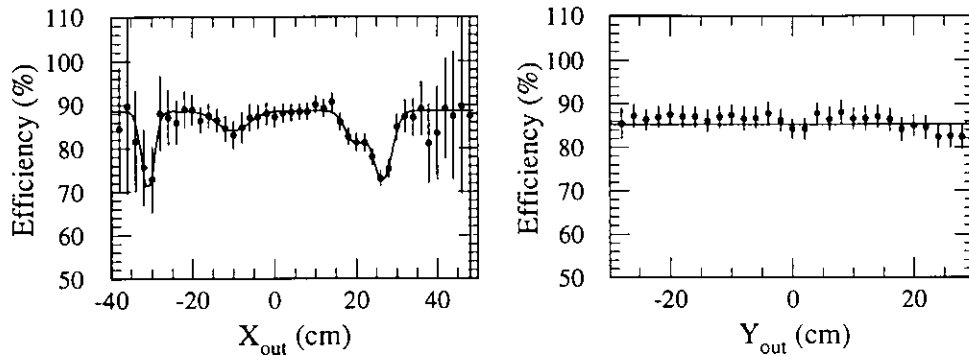
Figure 3.22: Typical SDC3-4 efficiency. Left: horizontal position (X_{out}), right: vertical position (Y_{out}).

SKS tracking efficiency

In the tracking routine, at first a loose χ^2_{SKS} cut was applied to reconstruct the particle trajectories in the SKS. However, a tight cut was applied in the final stage of the analysis procedure to reject the unwanted background sufficiently. The χ^2_{SKS} cut efficiency here estimated by the $(\pi^-, p)X$ events mixed in the PIK trigger. Taking a ratio of the reconstructed good protons with and without the χ^2_{SKS} cut, SKS tracking efficiency was thus estimated to be $92.2 \pm 2.9\%$ for the CH_2&Si data and particularly for the events gated with Si position. χ^2_{SKS} cut efficiency for the CH_2 events was also found to be almost same as this value. Figure 3.23 shows the reconstructed PID mass without(a) and with(b) the SKS χ^2_{SKS} cut. The PID resolution was improved with a proper χ^2_{SKS} cut and the PID cut efficiency for

the kaon selection was found to be 99.4 ± 1.6% in case of CH$_2$&Si data. Figure 3.24 shows the typical SKS chi-square distribution from the CH$_2$&Si data selecting $(\pi^-, p)X$ events.
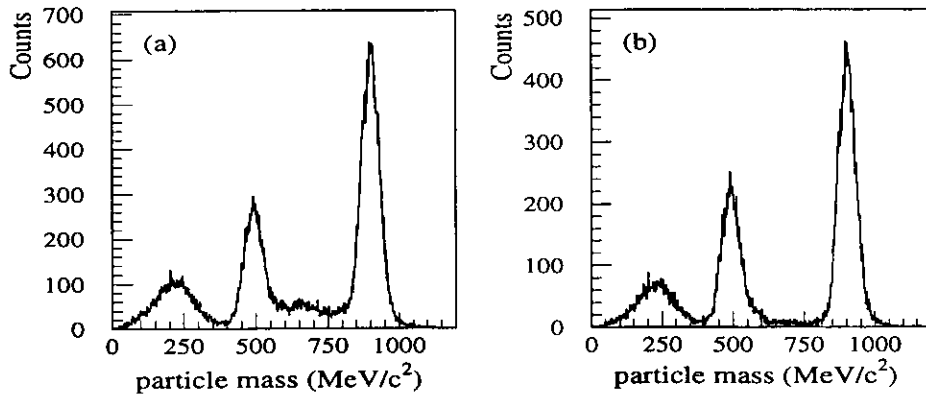
Figure 3.23: Typical PID spectra in the event reconstruction without(a) and with(b) SKS χ^2_{SKS} cut.
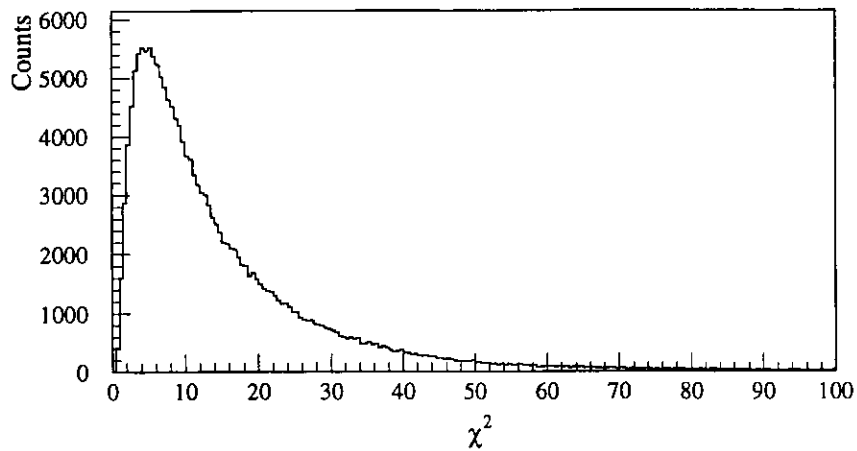
Figure 3.24: Typical distribution of the SKS χ^2 for the $(\pi^-, p)X$ events from CH$_2$&Si data.

K^+ decay factor

Since the $\beta\gamma c\tau$ of 0.72-GeV/c K^+ is almost 5.4 m, a part of the kaons produced in the target decays before they reach the detectors. The survival rate of SKS momentum reconstruction process was studied in detail with a Monte-Carlo simulation by T.Hasegawa [1]. Most of the K^+ decay events were rejected in the event reconstruction. The correction factor f_{decay} due to the decay was estimated to be 42% using an event by event correction taking into account of the momentum and the flight path length as $f_{decay} = \exp(-l/\beta\gamma c\tau)$, where l is the flight path length.

Event vertex cut efficiency

As the Z-vertex resolution around the forward angle region was bad due to the multiple scattering effects, a very careful treatment was needed to estimate the event vertex cut efficiency. In order to estimate it a Lorentz function was used which fitted well the Z-vertex distribution for the scattering angle from 4° to 8° as shown in figure 3.25. Then, the event vertex cut efficiency was estimated typically as $92.9 \pm 2.8\%$ for the Si events from the CH_2&Si data, whereas $90.4 \pm 3.9\%$ was obtained for the CH_2 events from the same set of data.
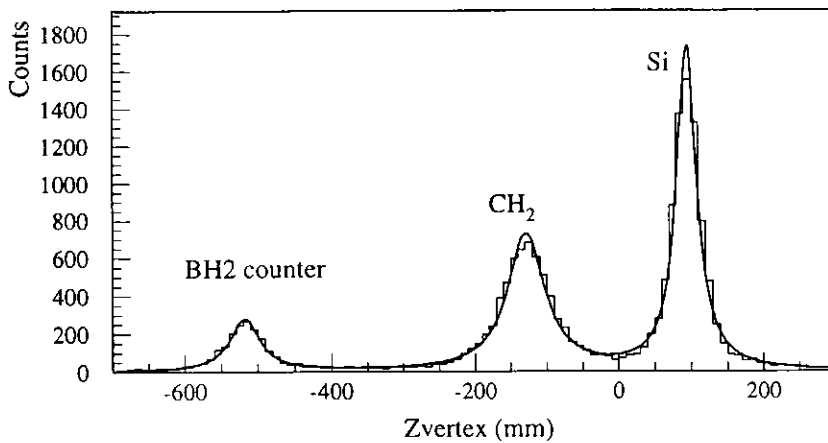
Figure 3.25: Typical Z-vertex distribution from the CH_2&Si data fitted by a Lorentz function.

3.7.2 The SKS Acceptance

The SKS acceptance was calculated by a Monte-Carlo simulation code, GEANT [43]. The geometrical configuration of the present experiment was kept same in the simulation and effect of multiple scattering, scattered particle's profile cut conditions were taken into account. Moreover a TOF timing cut was applied to the low momentum side of the TOF wall by comparing the timing spectra from the simulation and the analysis. Typical time distribution for the TOF slab number 12 from both of the simulation and the analysis is shown in figure 3.26. As seen in the figure the time distribution is sharply cut in the faster side on the data. It was also found by checking the raw TDC spectrum. This happened in the trigger level. In figure 3.6(a), the horizontal angular distribution is shown. The negative and positive side of the distribution in figure 3.6(a) we denote as the θ_- and θ_+, respectively. In SKS, particle having a comparatively low momentum and a large θ_- from the reaction point has a long trajectory as compared to the same one in the other side. So the particle having a θ_+ in the same condition as above is much faster. In the trigger label the time window for those faster kaons in the θ_+ side was very tight as we wanted to suppress the faster pions as much as possible. The TOF slab number 12, 13, 14 and 15 were found affected by this problem. For the other TOF slabs the time spectra both from the simulation and analysis were found similar. Hence, we applied a TOF timing cut by looking at the time spectra from the analysis.

In the event generator, the distribution of the beam profile defined as a function of (x_b, y_b, u_b, v_b) was produced from the experimental data, where x_b, y_b, u_b and v_b are the horizontal and vertical positions and their derivatives of a beam particle at the target.

The acceptance of the SKS $d\Omega(p, \theta)$ is denoted as follows:

$$\frac{d\Omega(p, \theta)}{dS(\theta)} = C(p, \theta) \tag{3.7}$$

where

$$p, \theta \quad : \quad \text{momentum and scattering angle,}$$
$$C(p, \theta) \quad : \quad \text{ratio of the accepted event to the generated event,}$$
$$dS(\theta) \quad : \quad \text{solid angle of the polar angle } \theta.$$

In the simulation, certain amount of events corresponding to scattered kaons were generated, whose momenta distributed within $p \pm \Delta p/2$ and scattering angles, $\theta \pm \Delta\theta/2$ to obtain $C(p, \theta)$. The acceptance maps as a function of p and θ were obtained for the upstream target position as well as for the downstream target position for each SKS excitation of 210A, 272A and 320A. Figure 3.27 shows the acceptance map for the downstream target position for 3 different SKS settings written in the figure. The figure was generated for the scattering angle from 4° to 8°. The sudden drop seen in the low momentum side of each setting was caused by the TOF timing gate used in the simulation as mentioned above.
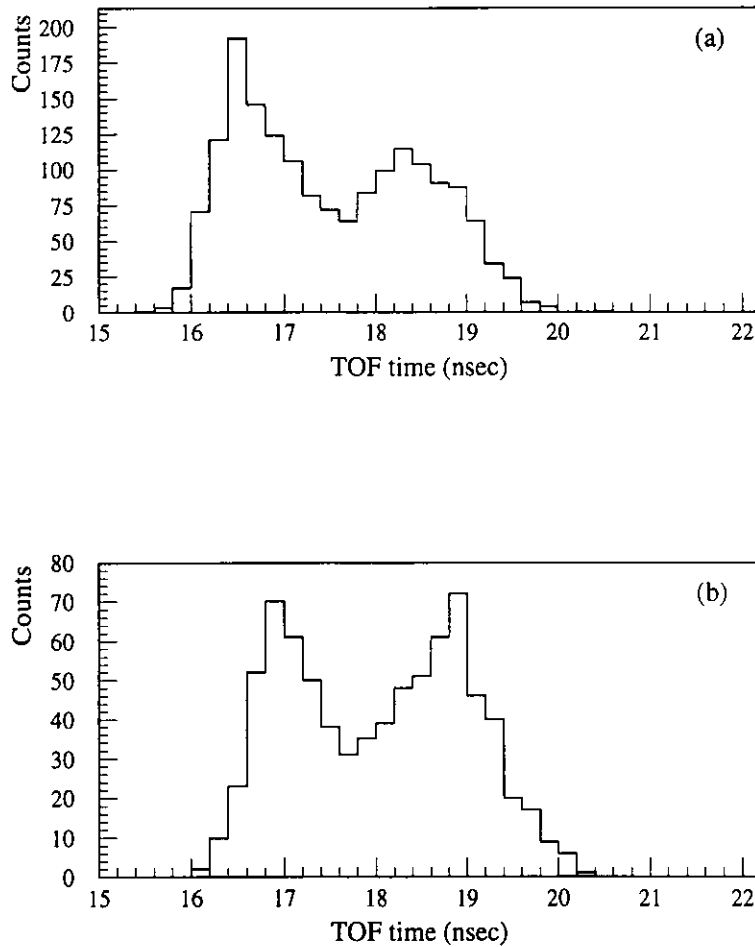
Figure 3.26: Typical time distribution of the TOF slab number 12 from the simulation(a) and the analysis(b) using the same experimental condition in the simulation. The distribution from the analysis clearly shows a sharply cut in the faster side. Both the figures are from the SKS current setting of 272A(2.2T).

Figure 3.28 shows a contour plot of SKS acceptance between the scattering angle and momentum.

The consistency of the SKS acceptance calculation was checked by the elementary cross section from the CH_2 target with all combination of target setup as well as comparing the Si and C spectra from three different SKS settings. Obtained elementary cross section in each setting is presented in section 3.7.4 and the inclusive Si and C spectra are presented in chapter 4.
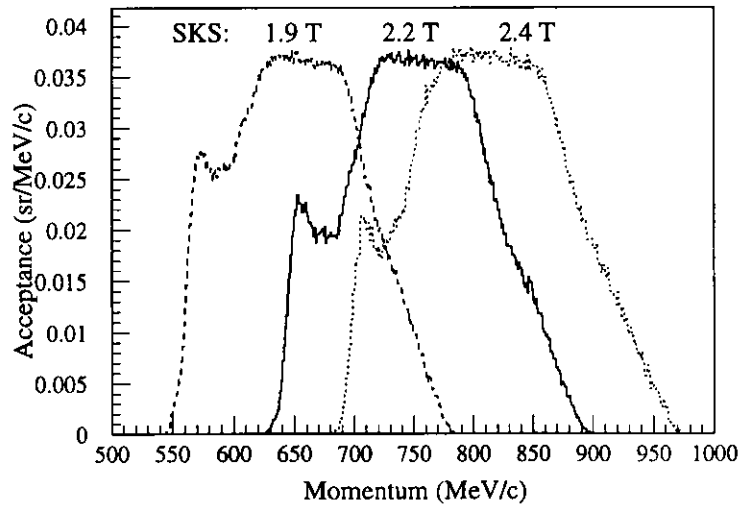
Figure 3.27: Momentum acceptance of SKS, seen from the downstream target position. Three different settings, SKS 1.9 T(210A), 2.2 T(272A) and 2.4 T(320A) are mentioned in the figure. Horizontal axis is kaon's momentum p in MeV/c and the vertical axis is in solid angle(sr).
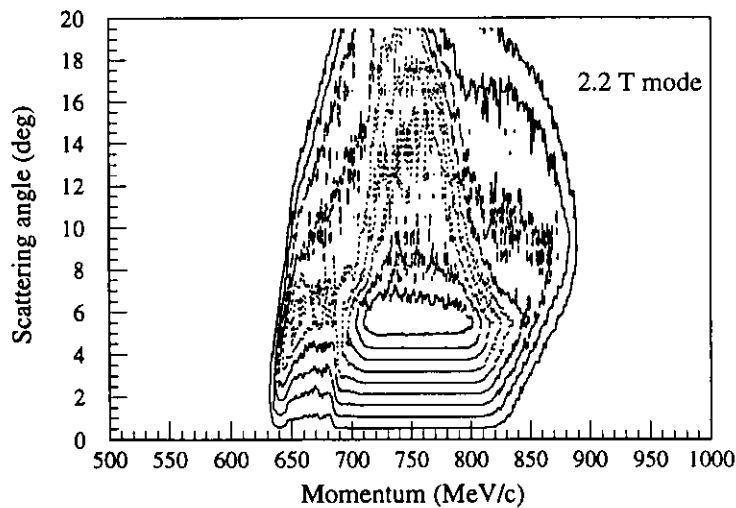
Figure 3.28: Contour plot of the SKS acceptance as a function of momentum and the scattering angle for the SKS 2.2 T mode seen from the downstream target position.

3.7.3 Application of the efficiency and the SKS acceptance

Application of the estimated detector and analysis efficiency factors to obtain the cross section is described here.

Among the factors in table 3.4, K^+ decay factor f_{decay}, position dependence of the SDC12 and SDC34 efficiencies and the SKS acceptance correction were estimated for event by event. f_{decay} was calculated from the reconstructed momentum P_{SKS} and flight path length for each event. As shown in figure 3.21 and 3.22, SDC12 and SDC34 efficiencies had position dependence. So the efficiencies were calculated from the fitting curves as follows;

$$\epsilon_{SDC12} = A_0 + A_1 \cdot f_{12}(x) = A_0\left(1 + \frac{A_1}{A_0} \cdot f_{12}(x)\right) ,$$

$$\epsilon_{SDC34} = B_0 + B_1 \cdot f_{34}(x) = B_0\left(1 + \frac{B_1}{B_0} \cdot f_{34}(x)\right) ,$$

$$A_0, A_1, B_0, B_1 = constant,$$
$$f_{12}(x), f_{34}(x) = efficiency\ curves$$
$$(function\ of\ hit\ position\ x) .$$

Using hit position x from the tracking information, $\left(1 + \frac{A_1}{A_0} \cdot f_{12}(x)\right)$ and $\left(1 + \frac{B_1}{B_0} \cdot f_{34}(x)\right)$ were calculated for each event.

Then, the corrected yield N_{corr} can be described as

$$N_{corr} = \sum_k \frac{1}{\left(1 + \frac{A_1}{A_0}f(x)\right) \cdot \left(1 + \frac{B_1}{B_0}f(x)\right) \cdot f_{decay} \cdot d\Omega\,(p,\theta)} . \tag{3.8}$$

In addition, the following efficiencies and factors were corrected run by run:

$$\epsilon_i = \left(\epsilon_{DAQ} \cdot \epsilon_{BDC} \cdot \epsilon_{K6track} \cdot f_{beam} \cdot A_0 \cdot B_0 \cdot \epsilon_{SKStrack} \cdot \epsilon_{vertex} \cdot f_{AC} \cdot \epsilon_{TOF\ LC\ mul.cut}\right)_i . \tag{3.9}$$

Then the cross section can be obtained as

$$\left(\frac{d\sigma}{d\Omega}\right) = \frac{A}{(\rho x) \cdot N_A} \cdot \frac{1}{\sum_i \epsilon_i \cdot I_i} \cdot \sum_k \frac{1}{\left(1 + \frac{A_1}{A_0}f(x)\right) \cdot \left(1 + \frac{B_1}{B_0}f(x)\right) \cdot f_{decay} \cdot d\Omega\,(p,\theta)} . \tag{3.10}$$

69

3.7.4 Elementary $p(\pi^-, K^+)\Sigma^-$ cross section

Data from elementary process in the present experiment are used mainly to calibrate the energy scale as well to check the accuracy of the measured cross section. In the section 3.6.4, results obtained from the energy scale calibration are discussed where the elementary missing mass spectra from the CH_2 target are presented in figures 3.14, 3.15, 3.16, 3.17, 3.18 and 3.19. In the lower parts of all those figures, events coming from the C target in CH_2 can be also seen. The inclusive C spectrum is presented in the next chapter. Taking into account all the estimated analysis and detector efficiencies as well as the calculated SKS acceptance, the differential cross section is obtained as

$$(\frac{d\sigma}{d\Omega})^{4°\sim8°}_{\pi^-p\to\Sigma^-K^+} \tag{3.11}$$

$$(\frac{d\sigma}{d\Omega})^{4°\sim8°}_{\pi^-p\to\Sigma^-K^+} \equiv \int_{\theta=4°}^{\theta=8°} \left(\frac{d\sigma}{d\Omega}\right) d\Omega \ / \ \int_{\theta=4°}^{\theta=8°} d\Omega \ . \tag{3.12}$$

In this section, the cross section of the elementary process, $(\frac{d\sigma}{d\Omega})^{4°\sim8°}_{\pi^-p\to\Sigma^-K^+}$ for the kaon's scattering angle at $4° \sim 8°$ are presented, which is obtained by fitting the elementary peak with a Gaussian form. The results are summarized in the table 3.5. The obtain value of cross section is given together with statistical(stat) and systematic(sys) errors. Estimation of the systematic error is described in the next subsection. Elementary cross section is found to be consistent in each set of data within error. The data includes both October and December cycles of the beam time which proves the validity of the present acceptance and the detection efficiencies estimation.

Table 3.5: The elementary cross section, $p(\pi^-, K^+)\Sigma^-$ from the different sets of data. The quoted errors are both statistical(stat) and systematic(sys).

Data set and (SKS current)	$\left(\frac{d\sigma}{d\Omega}\right)^{4°\sim8°}_{\pi^-p\to\Sigma^-K^+}$ $[\mu b/sr]$
CH_2 only (272A)	$127.20 \pm 9.59(stat)\pm7.19(sys)$
$CH_2\&Si$ (210A)	$128.41 \pm 8.13(stat)\pm6.09(sys)$
$CH_2\&Si$ (272A)	$124.73 \pm 7.48(stat)\pm6.15(sys)$
$CH_2\&Ni$ (272A)	$127.46 \pm 6.52(stat)\pm8.51(sys)$
$CH_2\&In$ (272A)	$122.82 \pm 5.42(stat)\pm6.54(sys)$
$CH_2\&Bi$ (272A)	$123.98 \pm 5.14(stat)\pm7.02(sys)$

Angular distribution of the $p(\pi^-, K^+)\Sigma^-$ reaction

The angular distribution of the elementary $p(\pi, K^+)\Sigma^-$ cross section over a wider angular range is obtained from the CH_2&Si data with SKS current setting of 210A. The result is shown in figure 3.29.

The angular distribution of the elementary process has been reported in the old bubble chamber experiments in 1960's ([44]), also shown in figure 3.29. Since the past experimental data was given in the center of mass system, it was transfered to the laboratory system for comparison with our obtained result. As a result, two points of the previous data appear near to $\theta_K = 10°$ and $17.5°$. A dotted curve is the angular distribution of the old data obtained from a Legendre fitting and solid curves indicate the error boundaries. The present data are shown as empty circles, which agrees well with the previous measurement and moreover improves the statistics very much.
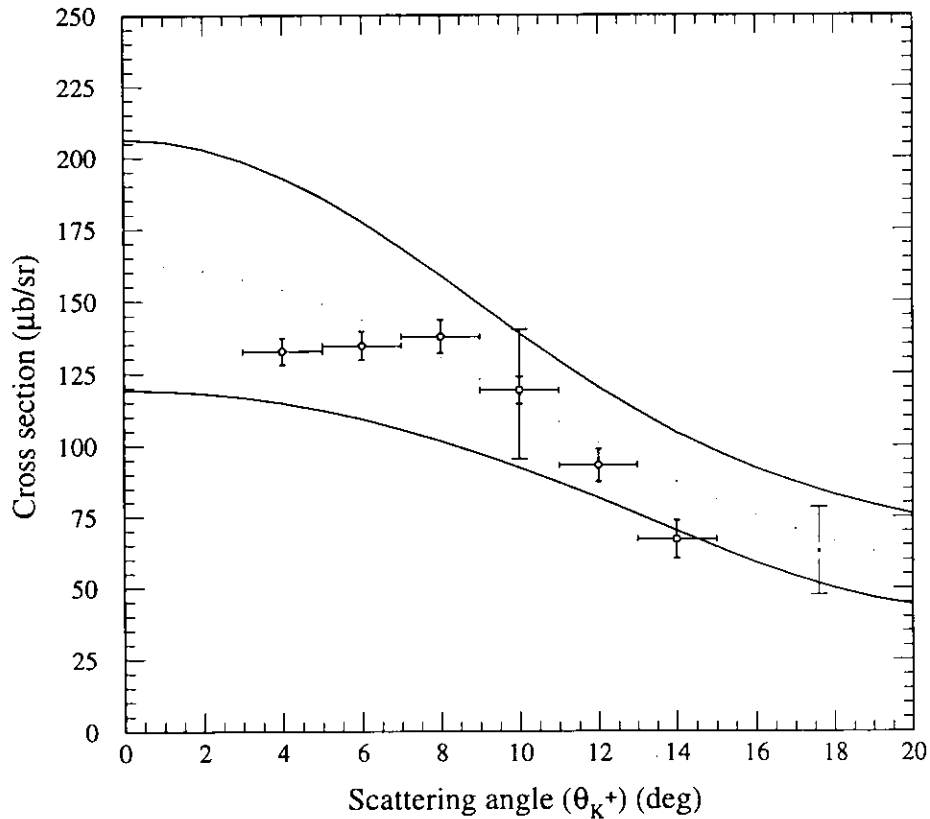
Figure 3.29: Angular distribution of the cross section from the elementary process, $p(\pi^-, K^+)\Sigma^+$. Empty circles are from the present data. The quoted errors are statistical.

71

3.7.5 Systematic errors

The total systematic error of the cross section was obtain from the errors of the target thickness, the SKS acceptance and the SDC3,4 chamber's position dependence of the efficiency. Other sources are found to be very small so as to neglect those contributions. The efficiency of the SDC3,4 was found to be position dependent as shown in figure 3.22 and the sudden drop corresponds to the rather lower momentum side of SDC3 chamber. To obtain the systematic error, the SDC3,4 efficiency function was varied within the fitting error. The SKS acceptance was also found to be affected by the trigger timing problem in the low momentum side. To study the systematic error, the timing cut was changed within the typical timing resolution of the TOF counter. As a result, the missing mass spectra on the lower momentum side or in other words, to the higher excitation energy regions, systematic errors were found to be large compared to the other side (figure 4.3, for example). The total systematic error obtained for the elementary process are summarized in the table 3.5 together with the elementary cross section and statistical errors.

3.7.6 Normalization of the yield by the beam momentum distribution

The shape of the missing mass spectra particularly, in the higher excitation energy side are found to be affected by the beam momentum distribution as the beam momentum distribution has a finite width ($\sim$ 38 MeV/c FWHM). As the low momentum side of the SKS acceptance found to be decrease rather sharply (figure 3.27), only at the very low momentum region or in other words, very high excitation energy region of the missing mass spectra were found to be affected. Then the final missing mass spectra were normalized by the beam momentum byte correction as follows; At first, the beam momentum distribution was divided into several region (here 7) by the width of the distribution in rms as shown in figure 3.30. Then the ratio of the intensity in a divided region to the total beam intensity was obtained as listed in table 3.6. The final missing mass spectra were the weighted average of the seven spectra obtained in each region.

Table 3.6: Typical Values of the beam intensity normalization

in figure 3.30	beam momentum MeV/c	typical ratio
(1)	$\sim$ 1166.0	$2.1 \pm 0.06\%$
(2)	$1166.0 \sim 1182.0$	$13.1 \pm 0.03\%$
(3)	$1182.0 \sim 1198.8$	$29.2 \pm 0.01\%$
(4)	$1198.0 \sim 1214.0$	$33.3 \pm 0.01\%$
(5)	$1214.0 \sim 1230.0$	$17.2 \pm 0.02\%$
(6)	$1230.0 \sim 1246.0$	$4.5 \pm 0.04\%$
(7)	$1246.0 \sim$	$0.4 \pm 0.1\%$
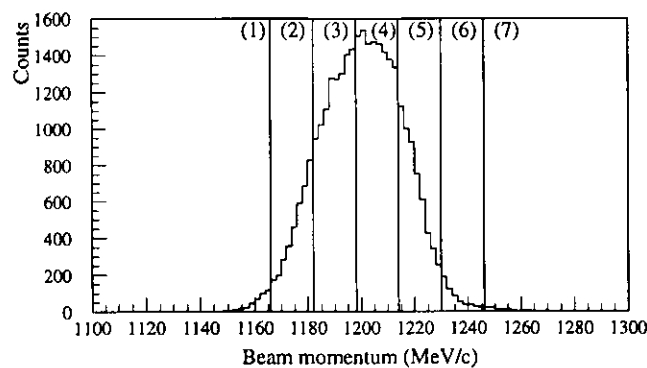
Figure 3.30: Typical beam momentum distribution divided into 7 regions for the beam momentum byte correction on the missing mass spectra.

3.7.7 Background level

One of the main advantage of the (π^-,K^+) reaction over (K^-, π^+) reaction is a lower background nature. By reconstructing the scattered particles mass we found the reconstructed kaons were well separated from the pions or protons (figure 3.5). However, a discussion of the yield, especially near the Σ^- binding threshold in the missing mass spectra needs a careful estimation of the background. In order to estimate the background level, in addition to the data on nuclear targets, we took the data without any target in the same condition; that was, π^- beam at 1.2 GeV/c and the SKS current setting at 272 A of about ~ 95 Gπ^- irradiation, such as near to a half of usual runs with-target.

Figure 3.31 shows the background level (broken line histogram) from the empty target data analysis. The Si spectrum(solid line histogram)is also shown for comparison. The horizontal axis is the Σ^- binding energy($-B_{\Sigma^-}$) in MeV and the vertical axis is the counts normalized by the total number of integrated beam in each case. The entry numbers shown in the figure was from the Si data whereas for the empty target data it was only 26 counts which is sufficiently low. Very near or below the Σ^- binding energy threshold there was no yield found coming from the empty target data. Thus we could neglect the background to discuss the whole spectrum shape.
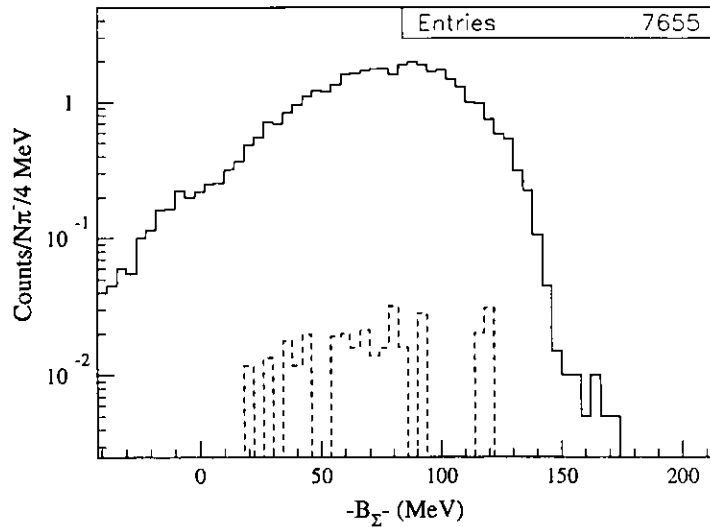
Figure 3.31: Background estimation in the (π^-,K^+) reaction from the empty target data analysis. Solid line histogram is from the Si data (entries 7655) where the broken line is from the empty target data (entries 26) assuming the Si kinematics.

Chapter 4

Experimental Results

The experimental results are presented in this chapter.

The inclusive (π^-, K^+) spectra have been generated for the kaon's scattering angle specified at $6° \pm 2°$. Below the $4°$, the Z-vertex resolution was distorted very much due to the multiple scattering effects in the target. The elementary process for a distribution of $6° \pm 2°$ is understood very well both in the kaon momentum spectrum as well as in the missing mass spectrum. All the other inclusive spectra are also obtained by the same cut in order to make the later discussion fair and to avoid the ambiguity of the SKS acceptance calculation in the larger scattering angle region. Results from the elementary process are presented in chapter 3. In this chapter, the inclusive spectra from ^{12}C, ^{28}Si, ^{58}Ni, ^{115}In and ^{209}Bi are presented. The differential cross section is obtained by the equation 3.12.

4.1 Silicon spectrum

The silicon spectra by the $^{28}Si(\pi^-, K^+)$ reaction are obtained from the CH$_2$&Si data with SKS three current settings as shown in figure 4.1, where three spectra are presented together in the missing mass scale in terms of the Σ^- binding energy (B_{Σ^-}). The vertical axis is in terms of $\mu b/sr/MeV$. Three spectra from three different settings are found to be overlapped very well within each acceptance. This again proves our well understanding in calculating the SKS acceptance as well as estimating the detector and analysis efficiency. By connecting these three spectra from the three settings enable us to discuss about the overall spectrum shape over a wider energy scale region as seen in the figure. Taking an weighted average from the three spectra in figure 4.1, the obtained Si spectrum is shown in figure 4.2, where the errors are statistical only. The average Si spectrum is also shown separately with the systematic errors only in figure 4.3. The detail description of the systematic error estimation is discussed in the previous chapter. In figure 4.4, the average Si spectrum is presented with both statistical and systematic errors. A small amount of contamination coming from the upstream CH$_2$ target can be seen in the Si spectrum (figure 4.4, for example) appeared as a sudden rise of

cross section at around 100 MeV of the excitation energy. It can be seen clearly in the Bi spectrum (figure 4.14) which affects the spectrum shape very much at around 100 MeV of the excitation energy. In section 4.5.1, estimation of the CH_2 contamination in the Bi spectrum is described. Same method is applied for the Si spectrum here and also for the Ni and In spectra. CH_2 contamination level in each spectrum is also mentioned in that section. Si spectrum after removing the CH_2 contamination is presented in figure 4.5.

K$^+$ Momentum (MeV/c)

850	790	730	670	605	535

☆ SKS 320A

● SKS 272A

○ SKS 210A

Differential cross section (μb/sr/MeV)

Binding energy ($-B_\Sigma$) (MeV)
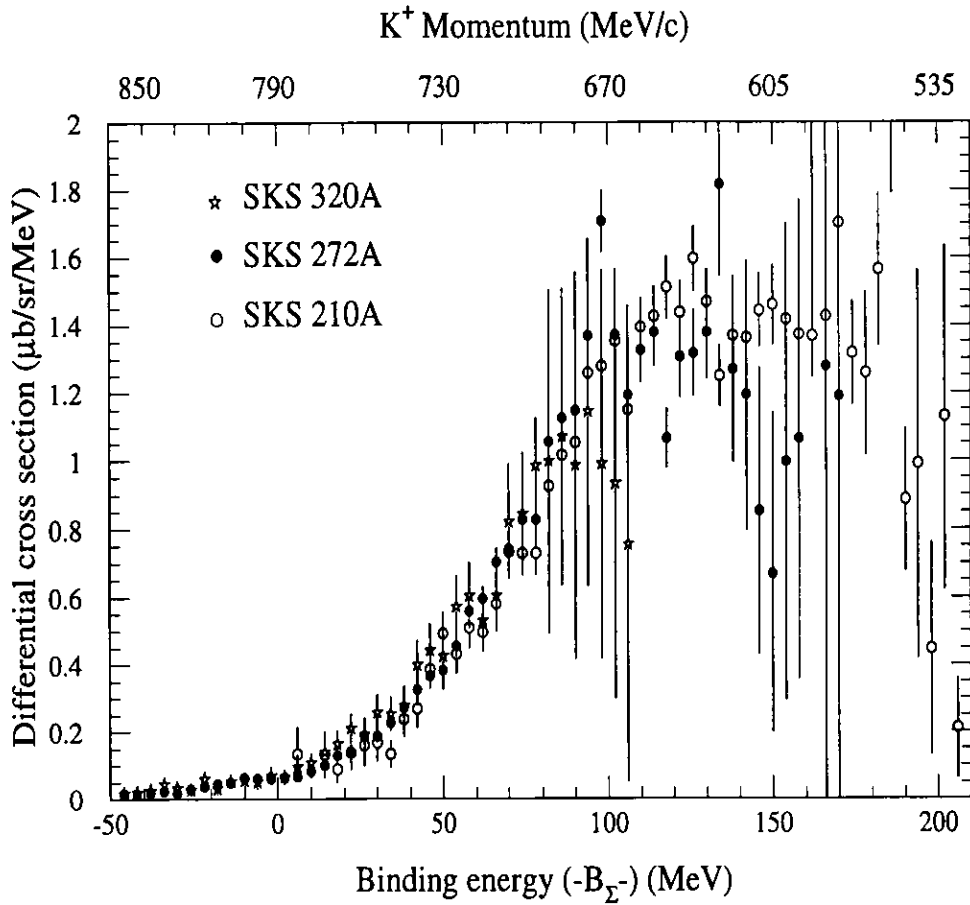
Figure 4.1: The ^{28}Si(π^-, K^+) inclusive spectra from the CH_2&Si data with SKS three current settings. Symbols stars, black circles and empty circles are those from SKS 320A, SKS 272A and SKS 210A, respectively. The quoted errors statistical only. The outgoing kaon momentum is also depicted on the top of the figure.
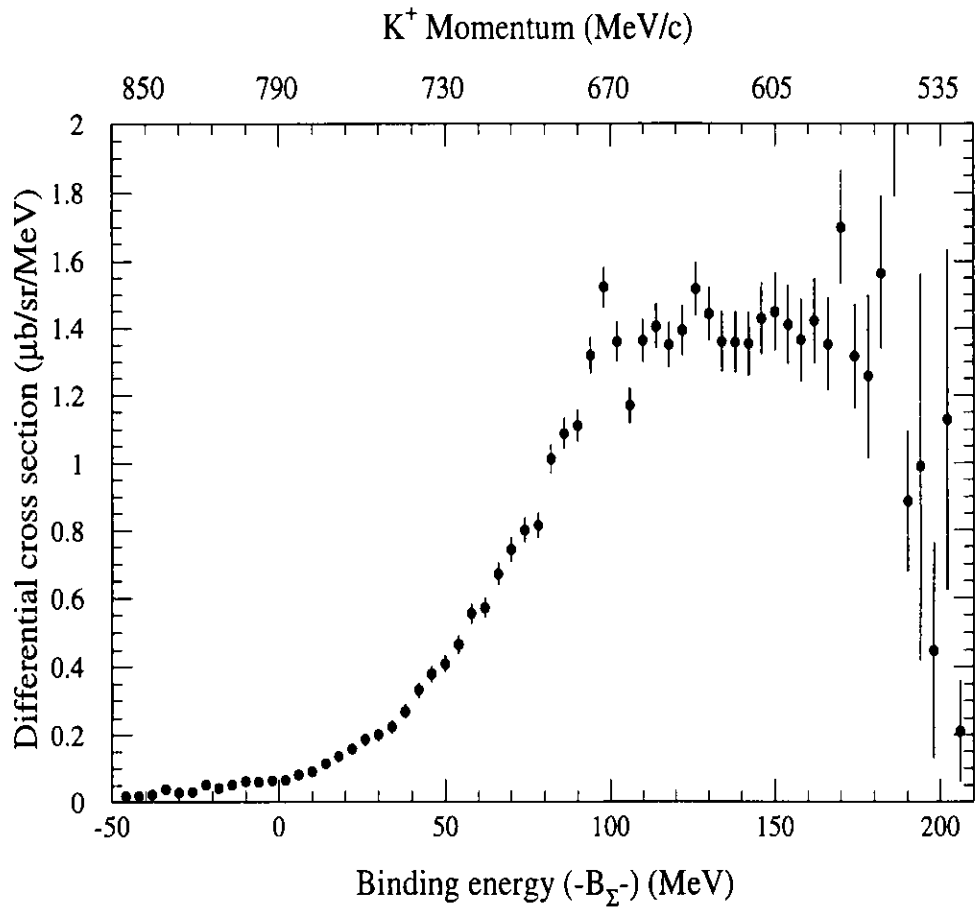
Figure 4.2: The ^{28}Si(π^-, K^+) inclusive spectrum obtained from the CH$_2$&Si data by taking an weighted average of three Si spectra measured with SKS three current settings(figure 4.1). The quoted errors are statistical only.

Figure 4.3: The ^{28}Si(π^-, K^+) inclusive spectrum obtained from the CH$_2$&Si data by taking an weighted average of three Si spectra measured with SKS three current settings(figure 4.1) and with systematic errors only.

Figure 4.4: The ^{28}Si(π^-, K^+) inclusive spectrum obtained from the CH$_2$&Si data by taking an weighted average of three Si spectra measured with SKS three current settings(figure 4.1). Errors include both statistical and systematic, where the boundary of the statistical error is shown by arm for each data point and the systematic error is plotted beyond the statistical error.
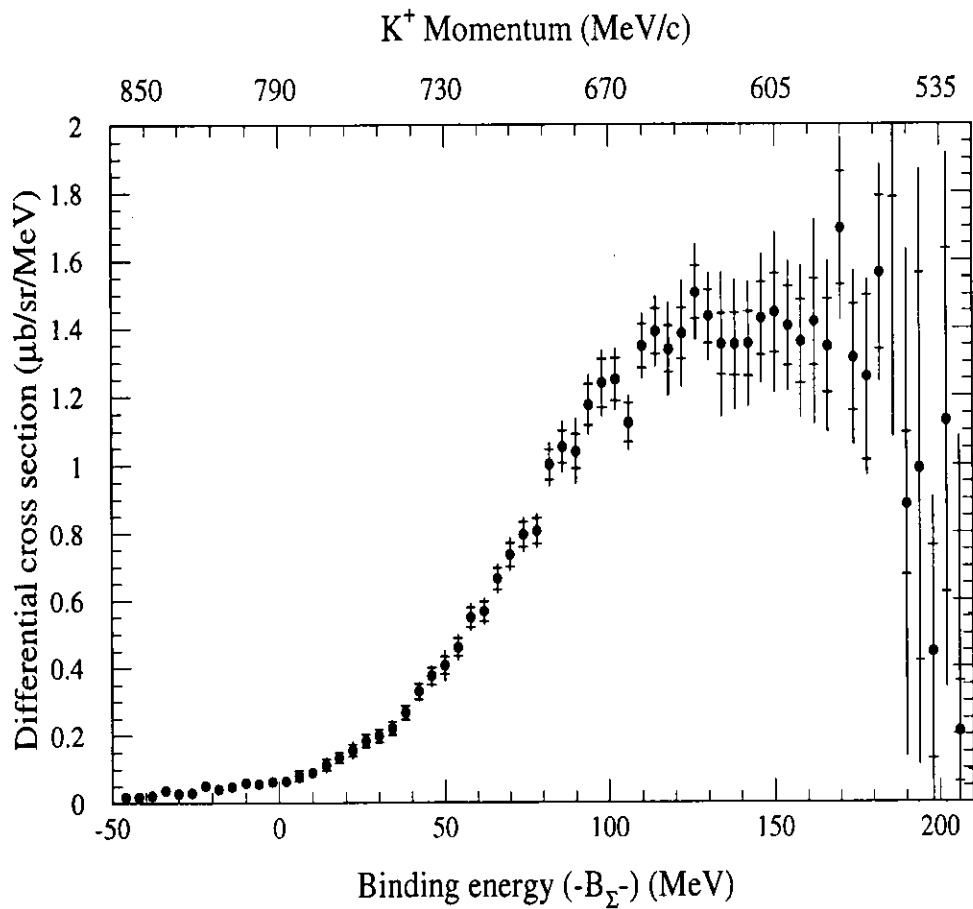
Figure 4.5: The average ^{28}Si(π^-, K^+) inclusive spectrum after removing the CH$_2$ contamination from figure 4.4. Errors include both statistical and systematic, where the boundary of the statistical error is shown by arm for each data point and the systematic error is plotted beyond the statistical error.

4.2 Carbon spectrum

The carbon spectra by the $^{12}C(\pi^-, K^+)$ reaction are obtained by selecting CH_2 events as the reaction vertex point and assuming the carbon kinematics, which is shown in figure 4.6 with SKS three current settings. As the elementary process from the proton target is dominated in the CH_2 events, a sharp contribution from the proton target is seen on the top of the carbon spectrum in all cases. Obtained carbon spectra by removing the elementary process are shown in the next figure 4.7. However, the gated region to remove the elementary process from the carbon spectrum also includes the carbon events as it is very hard to separate them individually or to estimate the carbon contribution separately. As a result, the carbon spectra is found to be sudden dropped at around 100 MeV of the excitation energy. Nevertheless, still we can discuss the carbon spectra from the deeply bound state to ~ 80 MeV above the Σ^- binding threshold as seen in the figure 4.7.
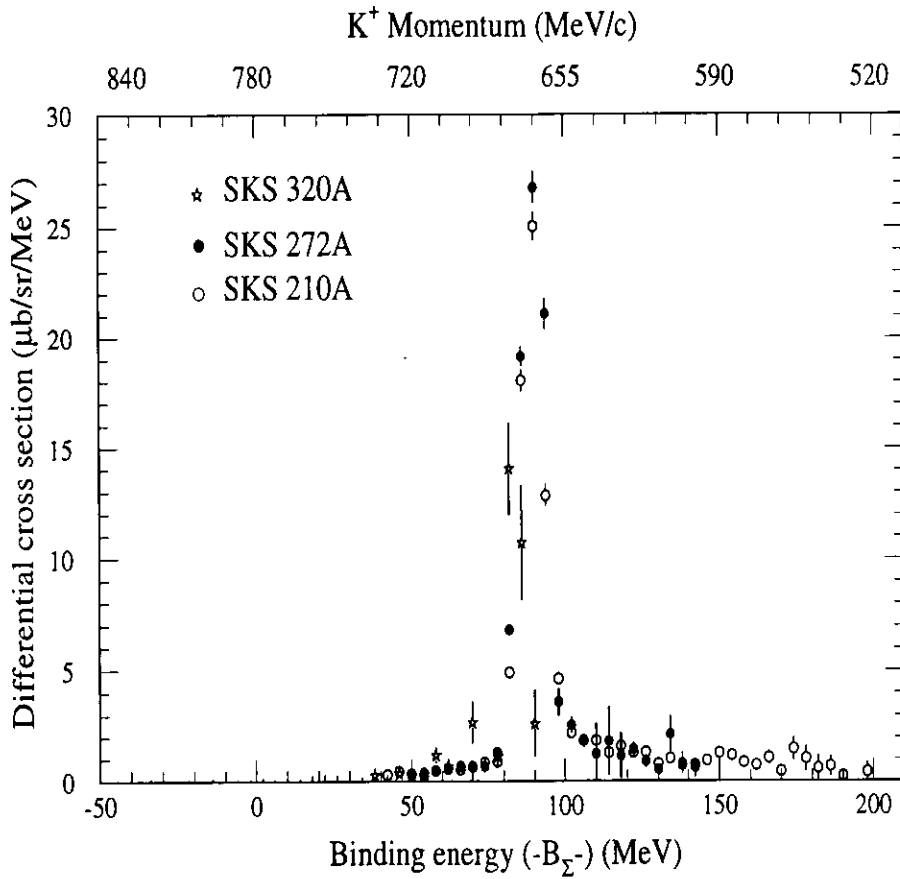
Figure 4.6: The $^{12}C(\pi^-, K^+)$ inclusive spectra obtained from the CH_2 target of CH_2&Si data with SKS three current settings assuming ^{12}C kinematics. Elementary contribution from the proton target is seen on the top of the carbon quasi-free spectra. The quoted errors are statistical only.

Same as Si spectrum, the average C spectrum is also obtained from the weighted average of three spectra (figure 4.7) and is shown in figure 4.8 with statistical errors only and with both statistical and systematic errors C spectrum is presented in figure 4.9.
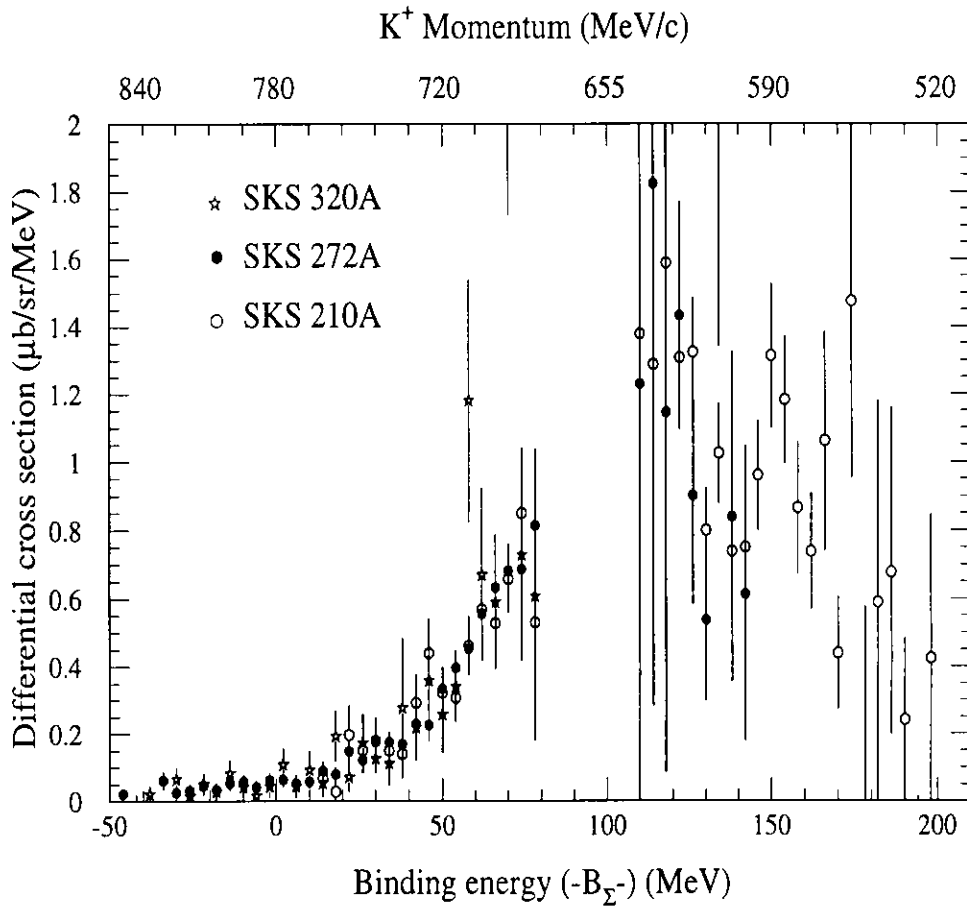
Figure 4.7: The $^{12}C(\pi^-, K^+)$ inclusive spectra obtained from the CH_2 target of CH_2&Si data with SKS three current settings assuming ^{12}C kinematics where the events from the H target are removed but it also caused the removal of C events on that region. For details, see the text. The quoted errors are statistical only.
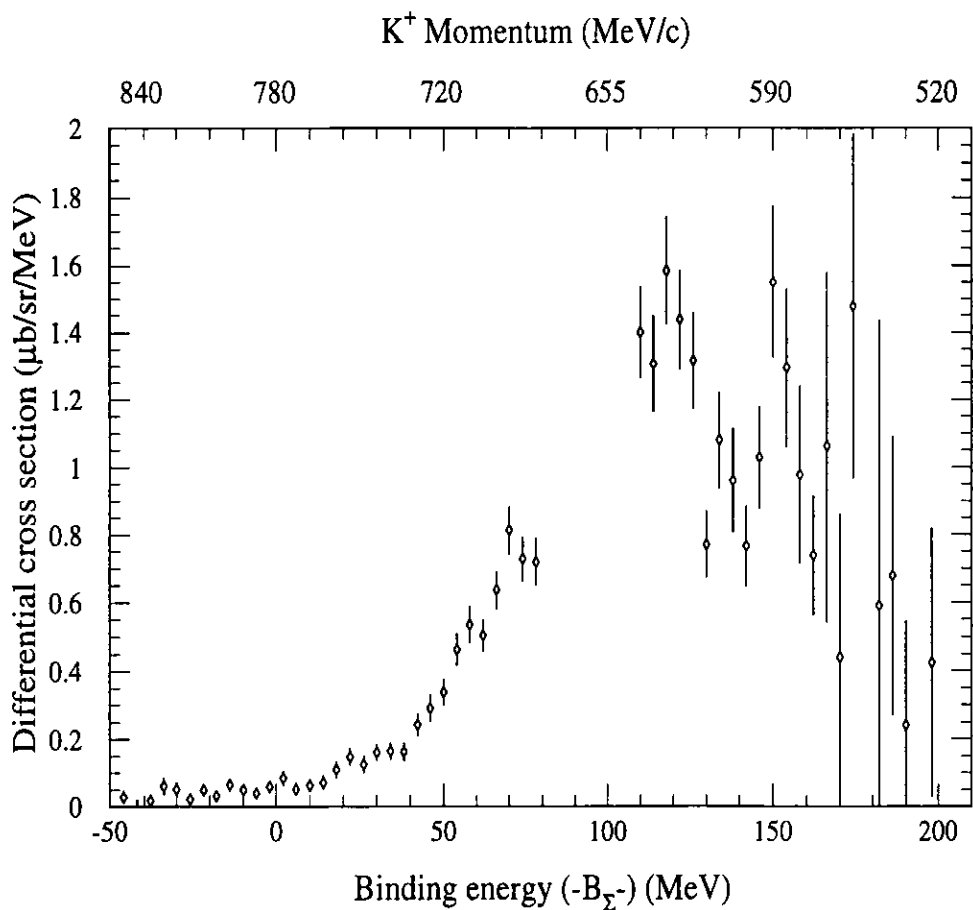
Figure 4.8: The $^{12}C(\pi^-, K^+)$ inclusive spectrum from the CH_2&Si data obtained by taking an weighted average of three C spectra measured with SKS three current settings(figure 4.7). The quoted errors are statistical only.
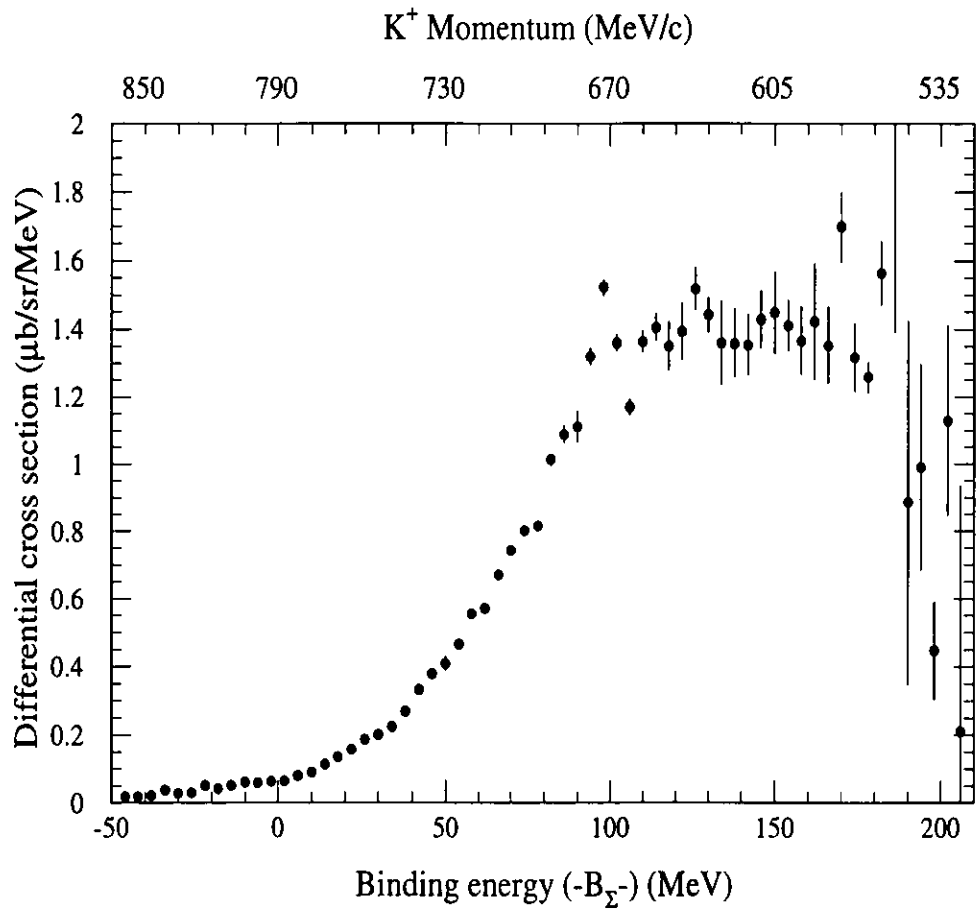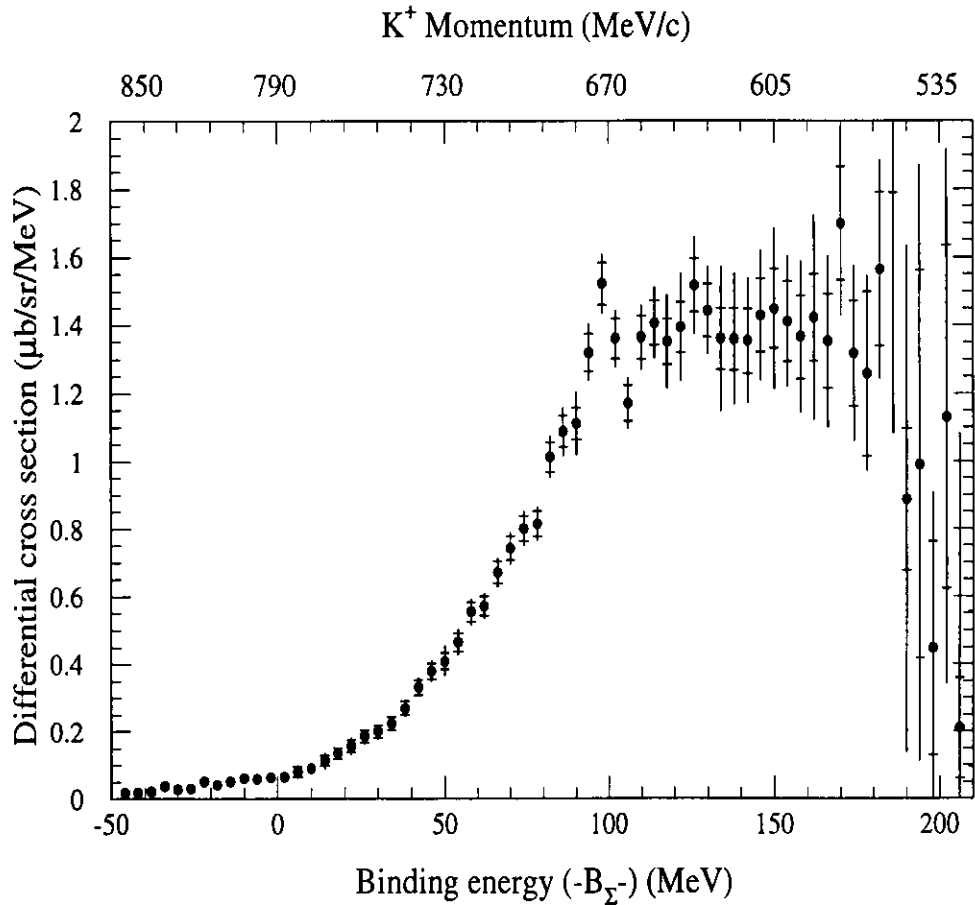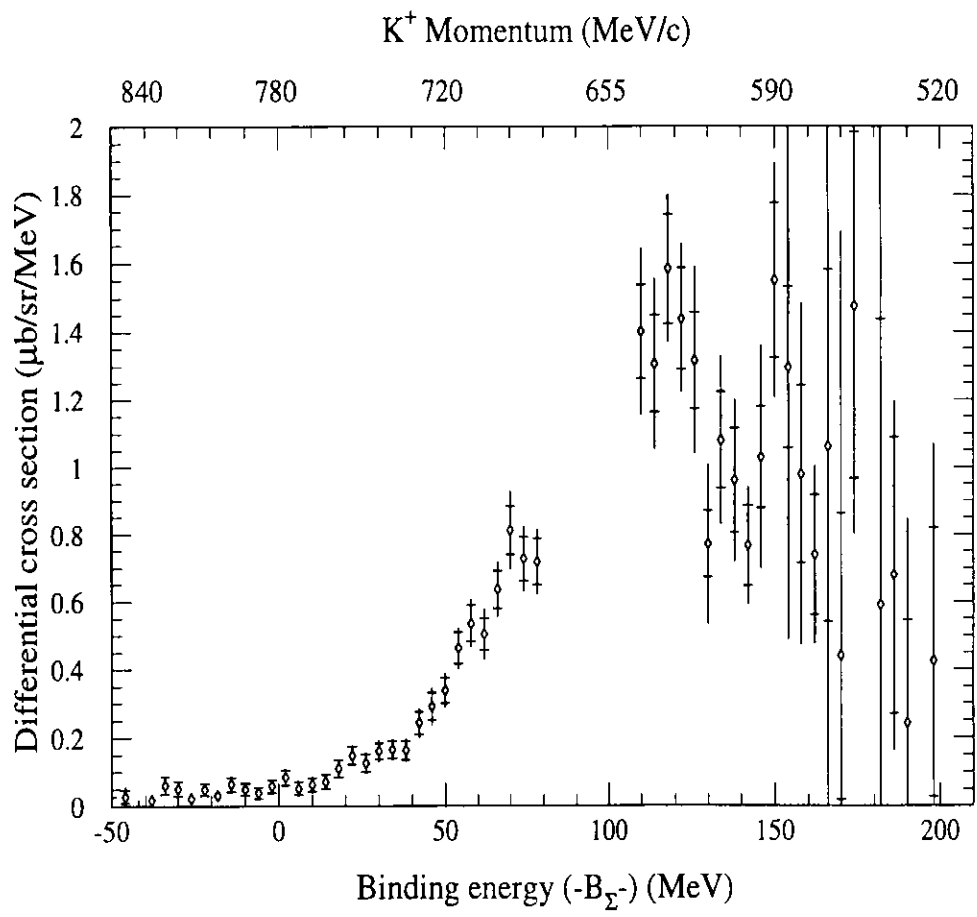
Figure 4.9: The $^{12}C(\pi^-, K^+)$ inclusive spectrum obtained from the CH_2&Si data by taking an weighted average of three spectra measured with SKS three current settings(figure 4.7). Errors include both statistical and systematic, where the boundary of the statistical error is shown by arm for each data point and the systematic error is plotted beyond the statistical error.

4.3 Nickel spectrum

Figure 4.10 shows the missing mass spectrum of the ^{58}In(π^-, K^+) reaction obtained from the CH$_2$&Ni data measured with SKS current 272A. The spectrum is plotted with both statistical and systematic errors. Contamination coming from the CH$_2$ target can be seen as an increase of the cross section at around 100 MeV of the excitation energy. In figure 4.13, Ni spectrum is presented by removing the CH$_2$ contamination.
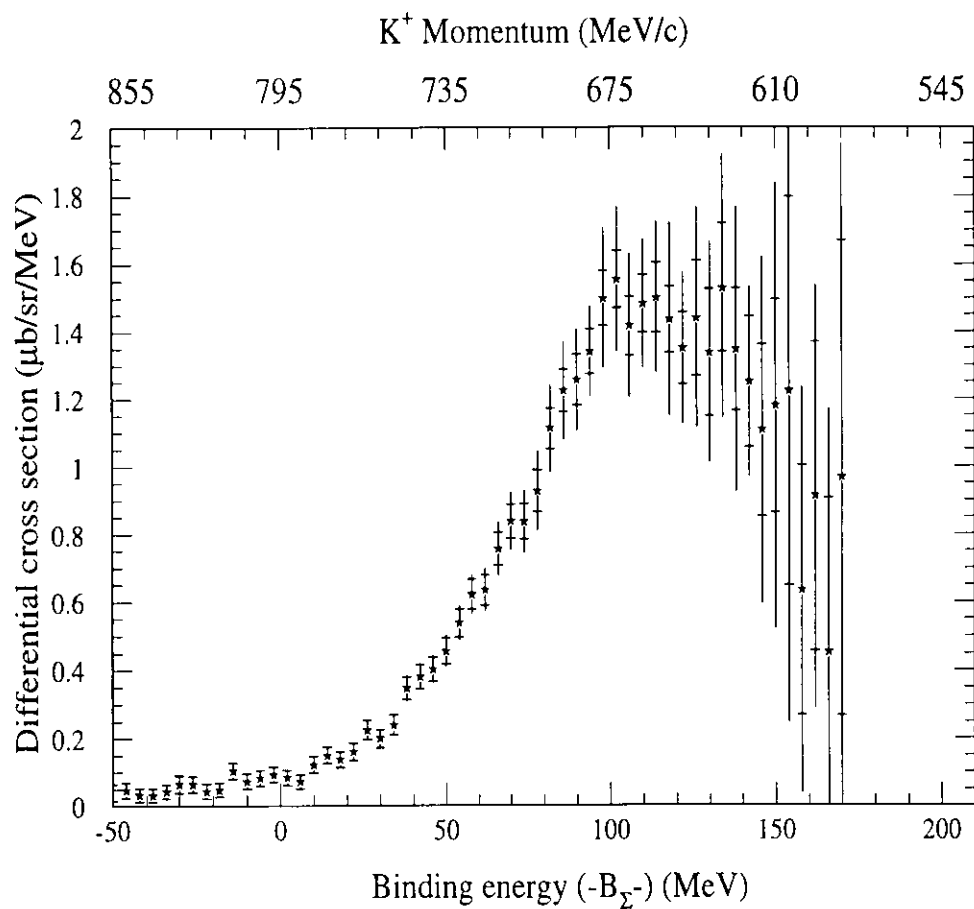
Figure 4.10: The ^{58}Ni(π^-, K^+) inclusive spectrum obtained from the CH$_2$&Ni data. The quoted errors are both statistical and systematic.
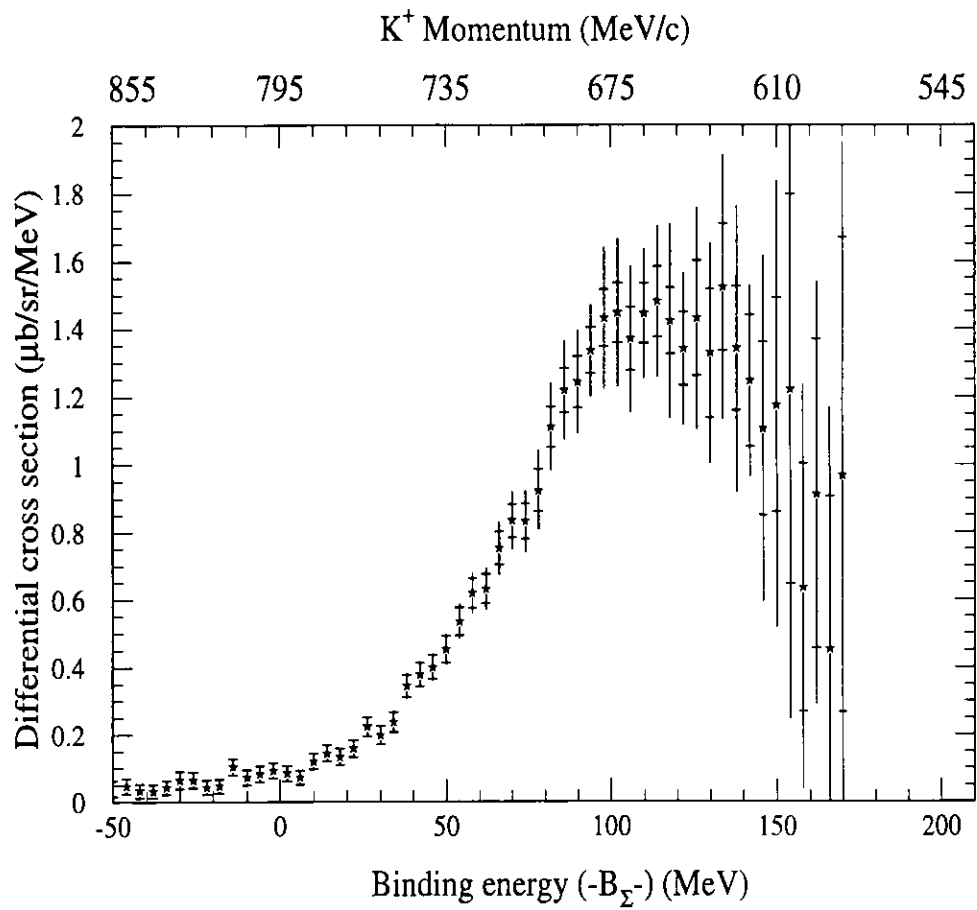
Figure 4.11: The ^{58}Ni(π^-, K^+) inclusive spectrum obtained from the CH$_2$&Ni data and after removing the contamination coming from the CH$_2$ target. The quoted errors are both statistical and systematic.

4.4 Indium spectrum

Figure 4.12 shows the missing mass spectrum of the ^{115}In(π^-, K^+) reaction obtained from the CH$_2$&In data measured with SKS current 272A. The spectrum is plotted with both statistical and systematic errors. A sharp increase of the cross section at around 100 MeV of the excitation energy is caused by the contamination coming from the CH$_2$ target. In figure 4.13, In spectrum is presented after removing the CH$_2$ contamination.
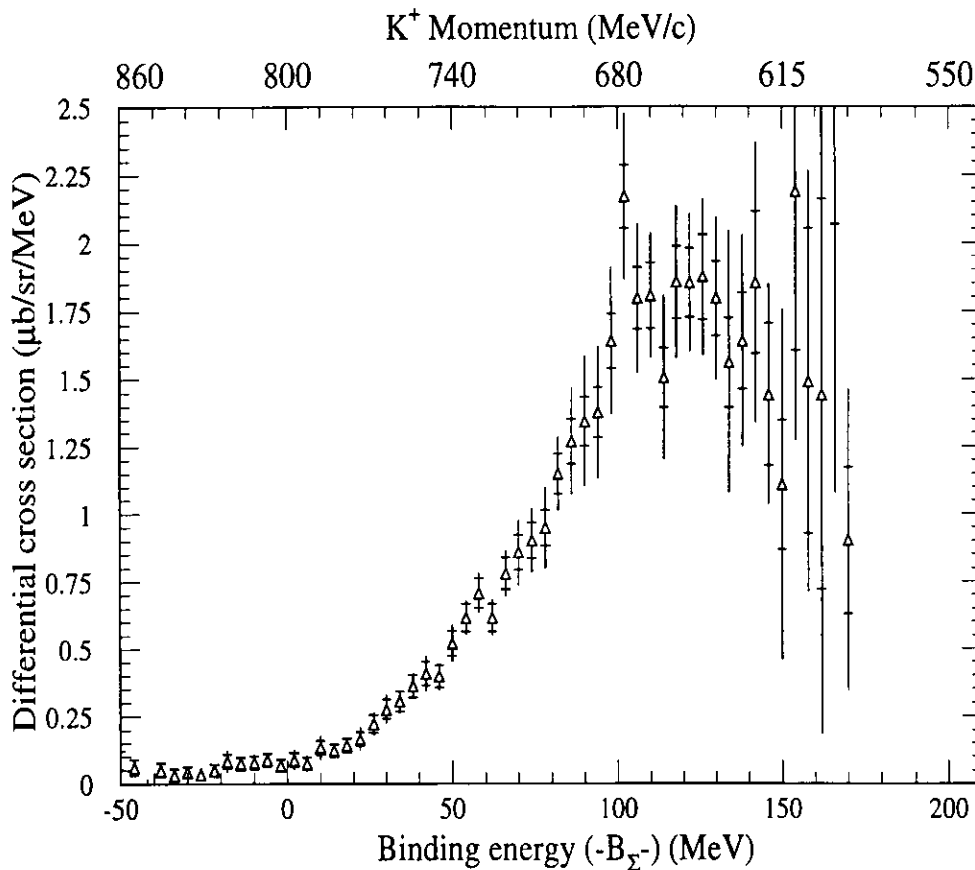
Figure 4.12: The ^{115}In(π^-, K^+) inclusive spectrum obtained from the CH$_2$&In data. The quoted errors are both statistical and systematic.
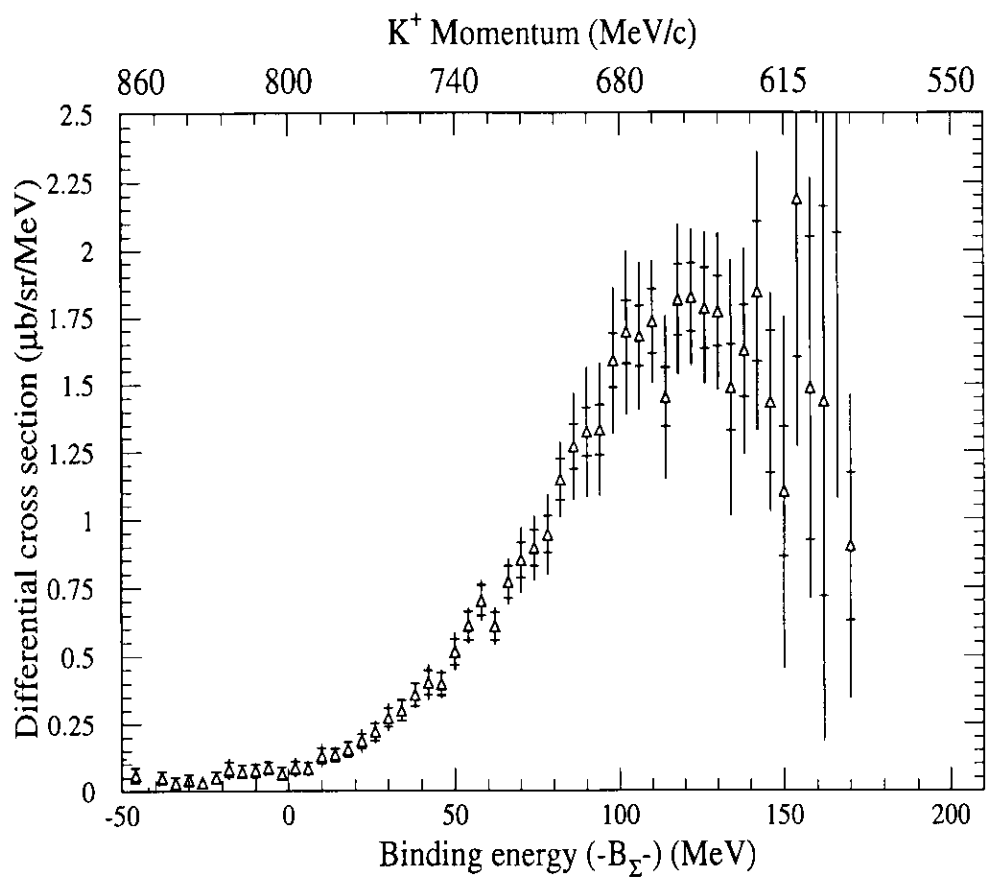
Figure 4.13: The ^{115}In(π^-, K^+) inclusive spectrum obtained from the CH$_2$&In data and after removing the CH$_2$ contamination. The quoted errors are both statistical and systematic.

4.5 Bismuth spectrum

Figure 4.14 is the missing mass spectrum of the ^{209}Bi(π^-, K^+) reaction obtained from the CH$_2$&Bi data measured with SKS current setting of 272A. Because of the heavier down stream target(here Bi), the Z-vertex resolution around the forward scattering angle region was distorted very much due to the multiple scattering effect in the target. As a result, a sudden rise of the cross section around $\sim$ 100 MeV excitation energy can be seen in the figure which affects the spectrum shape very much. This comes from the CH$_2$ target. Inclusive spectra on Si, Ni and In are also found be affected slightly by this fact. Estimation of the contamination level in the Bi spectrum coming from the CH$_2$ target is described in the next subsection 4.5.1.
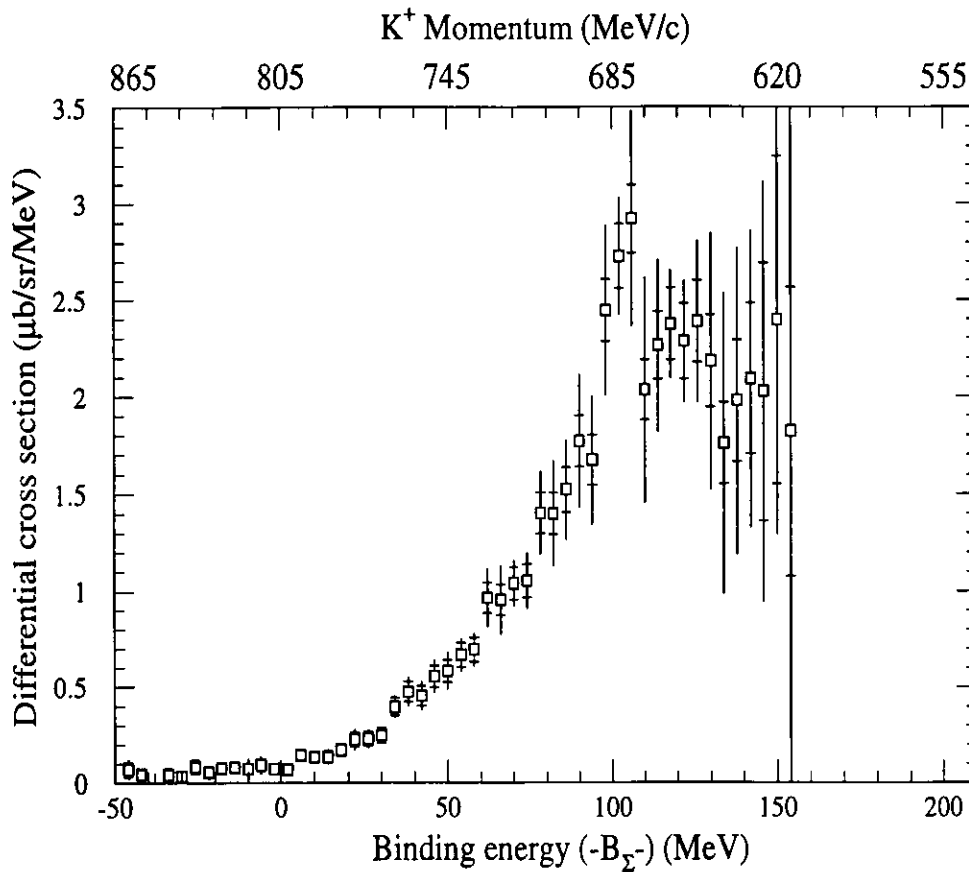
Figure 4.14: The ^{209}Bi(π^-, K^+) inclusive spectrum obtained from the CH$_2$&Bi data. Description is given in the text. The quoted errors are both statistical and systematic.

4.5.1 Estimation of the CH$_2$ events contamination in the Bi spectrum

As the Z-vertex resolution around the forward angular region was worse due to the multiple scattering effect in the downstream target (here Bi), a scattering angle cut greater than 4° was selected for all the inclusive spectra. But even by a scattering angle cut greater than 4°, CH$_2$ contamination in the inclusive spectra (Si,Ni, In and Bi) could not be removed completely. As a result, a sudden rise of the cross section appeared at around 100 MeV of the excitation energy in all spectra and in particularly, shape of the Bi spectrum is found to be affected very much in that region. We identified this sharp increase is caused by the hydrogen events from the CH$_2$ target. However, the carbon events from the CH$_2$ target are scattered as we could see in the CH$_2$ events distribution (figure 3.19, for example), where elementary(H) events appeared as a sharp peak and the carbon events were scattered and appeared in the lower part of the histogram. The description given here for the estimation of CH$_2$ contamination in the Bi spectrum and to remove that contamination from the Bi spectrum. Same procedure is applied to remove the CH$_2$ contamination from all other spectra individually.

At first, the hydrogen contamination in the Bi spectrum is estimated by fitting the Bi spectrum by the function of P$_1$+G+G, where P$_1$ is a first order polynomial
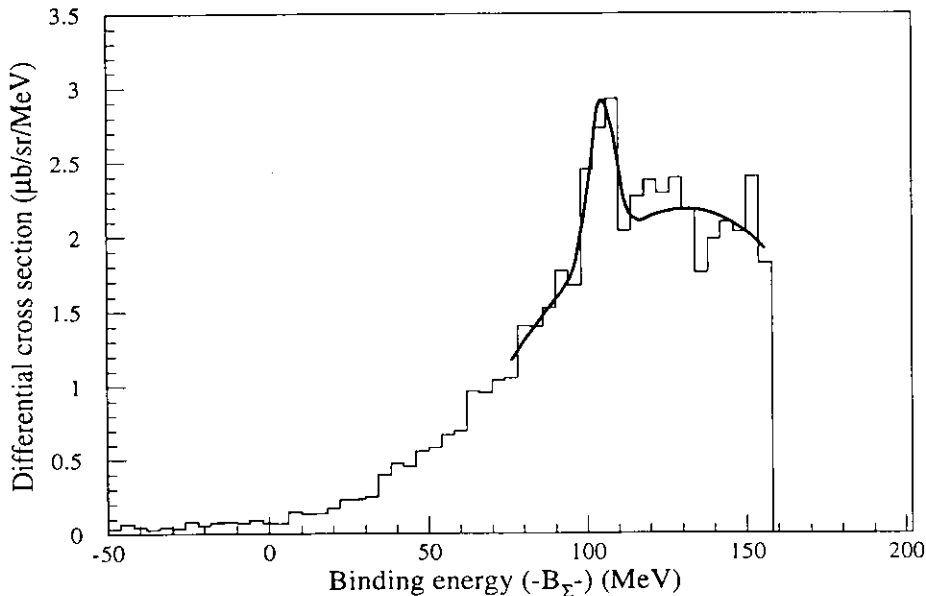
Figure 4.15: Hydrogen peak in the Bi spectrum is fitted to estimate the hydrogen contamination level.

function and G represents a Gaussian function as seen in figure 4.15. From the fitting result of the first Gaussian function, hydrogen contamination in the Bi spectrum is estimated to be 9.39 ± 5.29 μb/sr. Then, to estimate the carbon contamination in the Bi spectrum, gating the Z-vertex for the CH_2 target the spectrum is generated by the Bi kinematics and is shown in figure 4.16. Fitting by two Gaussian functions and from the fitting result of the prominent peak, the hydrogen contribution is calculated and the rest are thought to be the carbon contribution. As a result, the ratio of the carbon to hydrogen contribution($R_{C/H}$) in the CH_2 target was found to be $31.3 \pm 5.04\%$. Assuming $R_{C/H}$ is target independent, finally the carbon contamination in the Bi spectrum is found be 2.94 ± 1.87 μb/sr. Then the CH_2 spectrum (figure 4.16) is normalized to the obtained contamination level and is plotted in figure 4.17. Finally, that normalized CH_2 spectrum is subtracted from the Bi spectrum in figure 4.14. Final Bi spectrum after removing the CH_2 contamination is presented in figure 4.18.

By using the same procedure, contamination level in the Si spectrum is estimated to be 2.34 ± 1.34 μb/sr and 0.79 ± 0.53 μb/sr from H and C, respectively. In the Ni spectrum it is found to be 1.86 ± 1.09 μb/sr and 0.65 ± 0.37 μb/sr from H and C, respectively. In the In spectrum, 3.76 ± 1.94 μb/sr and 1.28 ± 0.67 μb/sr are estimated to be come from H and C, respectively.
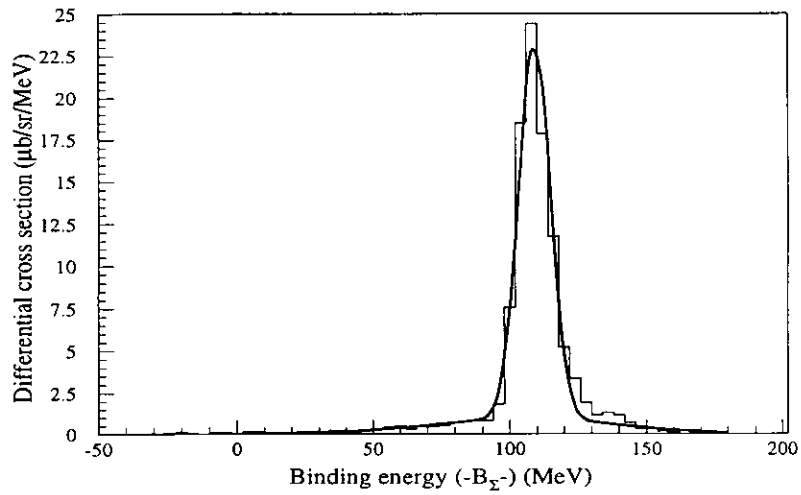
Figure 4.16:CH$_2$ events from the CH$_2$&Bi data are generated by the Bi kinematics to obtain the H to C ratio so as to estimate the C contamination level in the Bi spectrum. The spectrum is fitted by the two Gaussian functions. The carbon to hydrogen ratio is found to be $31.3 \pm 5.04\%$.
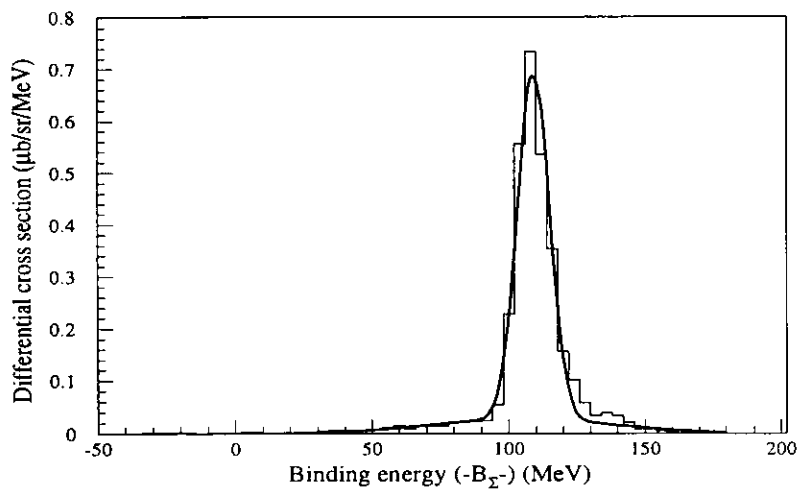
Figure 4.17: Normalized CH$_2$ spectrum obtained by the contamination level of H and C in the Bi spectrum, which is to be subtracted from the Bi spectrum in order to remove the CH$_2$ contamination.
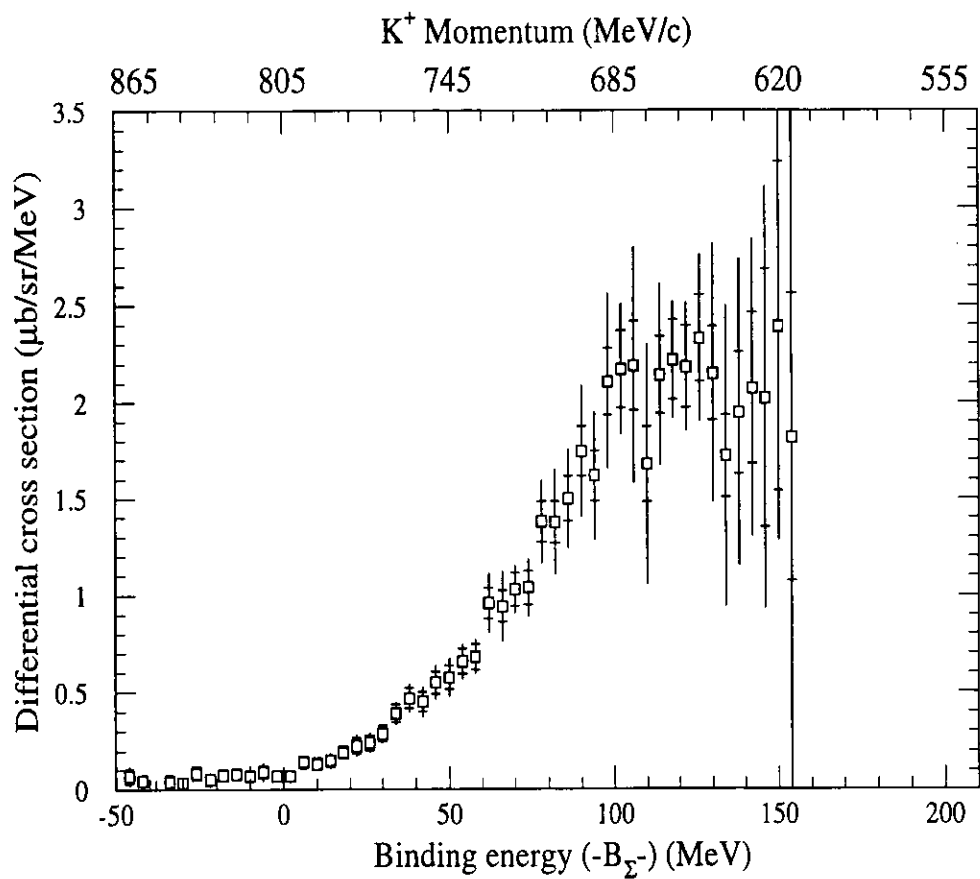
Figure 4.18: The ^{209}Bi(π^-, K^+) inclusive spectrum after removing the CH$_2$ contamination. See text for detail. The quoted errors are both statistical and systematic.

Chapter 5

Discussion

In this chapter, discussions are done following the results presented in the last chapter. The discussion on the elementary process has been made extensively in chapter 3. Discussions on the measured Si spectrum by comparing with the Monte-Carlo simulated spectra are done in this chapter. The observed Si spectrum is also compared with the theoretical spectra, calculated in the framework of DWIA and the discussions are made based on the comparison.

5.1   Inclusive spectra

The observed inclusive spectra for C, Si, Ni, In and Bi have been presented in the previous chapter. The Si and C spectra were measured with SKS three current settings to cover a wider energy scale in missing mass$(M_{HY} - M_A)$. As seen in the figures 4.1 and 4.7, spectrum with different SKS setting overlap very well within each acceptance. It guarantees the quality of our observed spectra to make the physics discussion rather fairly. The inclusive spectra for Ni, In and Bi were taken by only SKS 272A setting, but can be treated on the same footing as the C and Si data since inclusive spectra on both C and Si with SKS three current settings were found to be overlapped well within the statistics (figure 4.7, 4.1). Then, the peak position of each inclusive spectrum is found to be greater than 100 MeV from the Σ^- binding threshold (B_{Σ^-}=0).

5.2   Similarity of the inclusive spectra

From the analysis of the inclusive spectra it is found that all the inclusive spectra show a similarity in shape at least upto the $-B_{\Sigma^-} \leq 90$ MeV as shown in figure 5.1. All the inclusive spectra are overlayed together where all the data are taken for the SKS current setting at 272A in order to make the comparison easy.

94
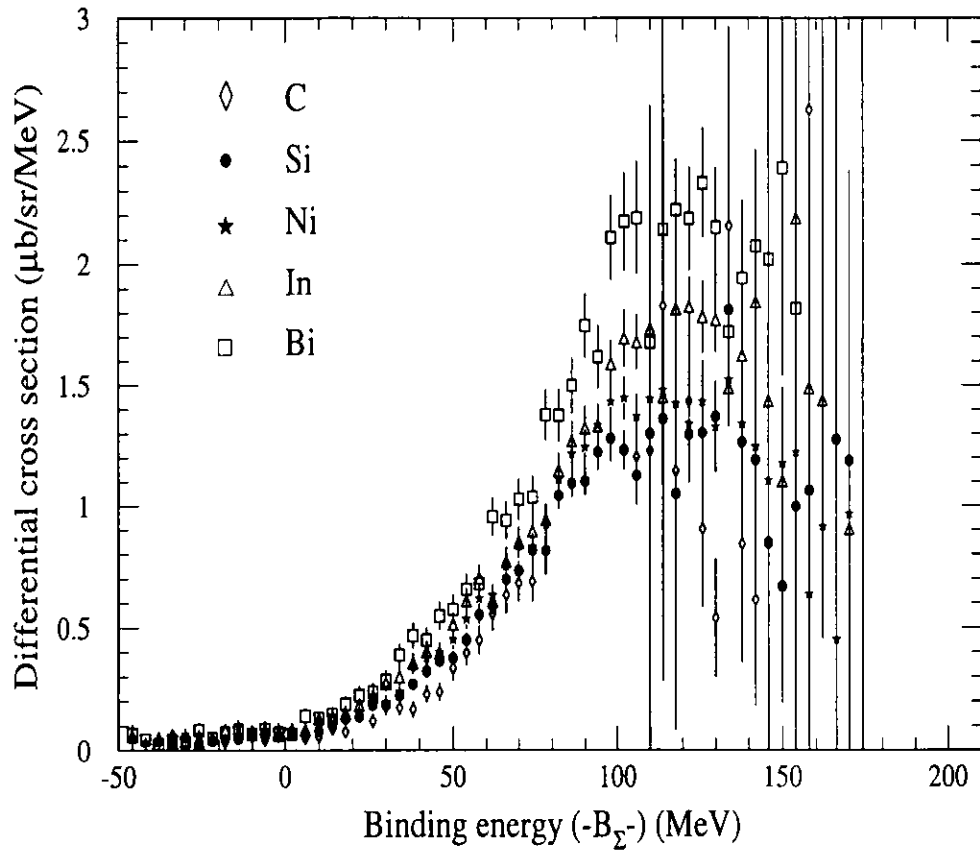
Figure 5.1: Comparison of the inclusive spectra on each target taken for the SKS current setting at 272A. The quoted errors are statistical only.

5.3 Mass number dependence of cross section

Mass number dependence of the Σ^- production cross section is obtained from the ratio of the inclusive Si spectrum to the others. The comparison is made after removing the CH_2 contamination from all spectra and are as follows;

- Ratio of C data (from CH_2&Si data at SKS 272A)
  to Si data (from CH_2&Si data at SKS 272A).

- Ratio of In data (from CH_2&In data at SKS 272A)
  to Si data (from CH_2&Si data at SKS 272A).

- Ratio of Ni data (from CH_2&Ni data at SKS 272A)
  to Si data (from CH_2&Si data at SKS 272A).

- Ratio of Bi data (from CH_2&Bi data at SKS 272A)
  to Si data (from CH_2&Si data at SKS 272A).

Results are shown in figures 5.2, 5.3, 5.4 and 5.5. The fitting region is also shown in each figure by the fitted line. Fitting results are summarized in table 5.1.

Table 5.1: Fitting results of the ratio of cross section $(0 < -B_\Sigma < 90 \text{ MeV})$. The quoted errors are statistical.

data	fitting result
C	0.81 ± 0.15
Si	1.
Ni	1.16 ± 0.07
In	1.26 ± 0.09
Bi	1.49 ± 0.12
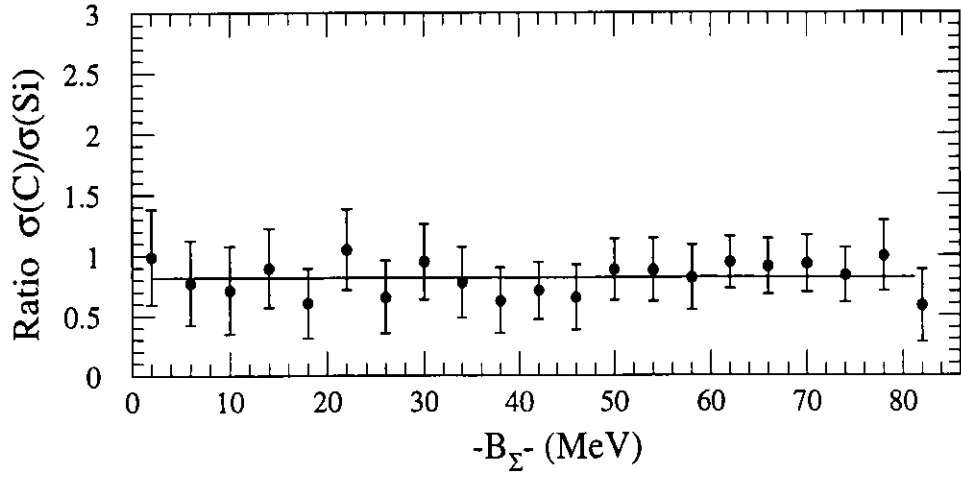
Figure 5.2: Ratio of the cross section, $\left(\frac{d^2\sigma}{d\Omega dE}\right)_{C,SKS272A} / \left(\frac{d^2\sigma}{d\Omega dE}\right)_{Si,SKS272A}$
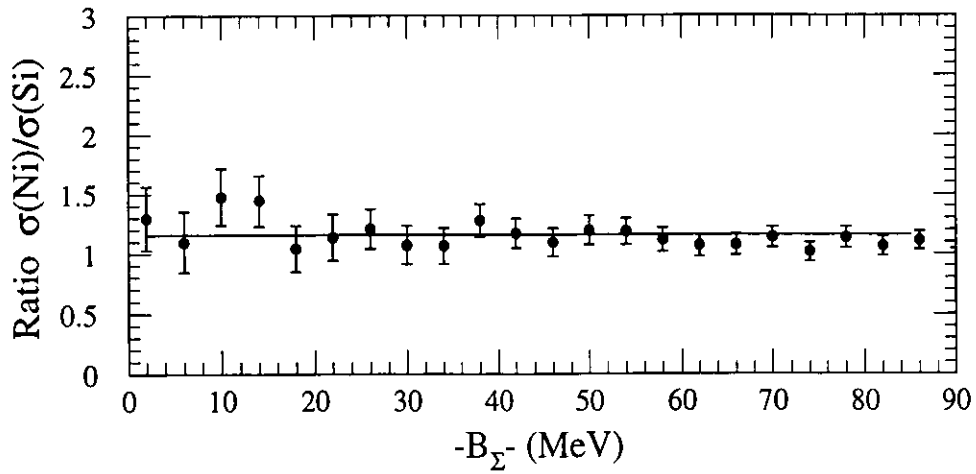
Figure 5.3: Ratio of the cross section, $\left(\frac{d^2\sigma}{d\Omega dE}\right)_{Ni,SKS272A} / \left(\frac{d^2\sigma}{d\Omega dE}\right)_{Si,SKS272A}$

97
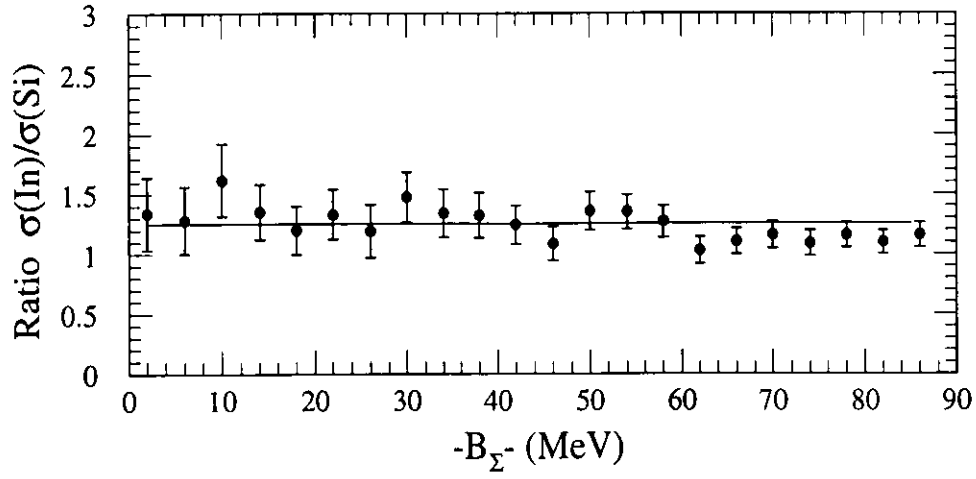
Figure 5.4: Ratio of the cross section, $\left(\frac{d^2\sigma}{d\Omega dE}\right)_{In,SKS272A} \Big/ \left(\frac{d^2\sigma}{d\Omega dE}\right)_{Si,SKS272A}$
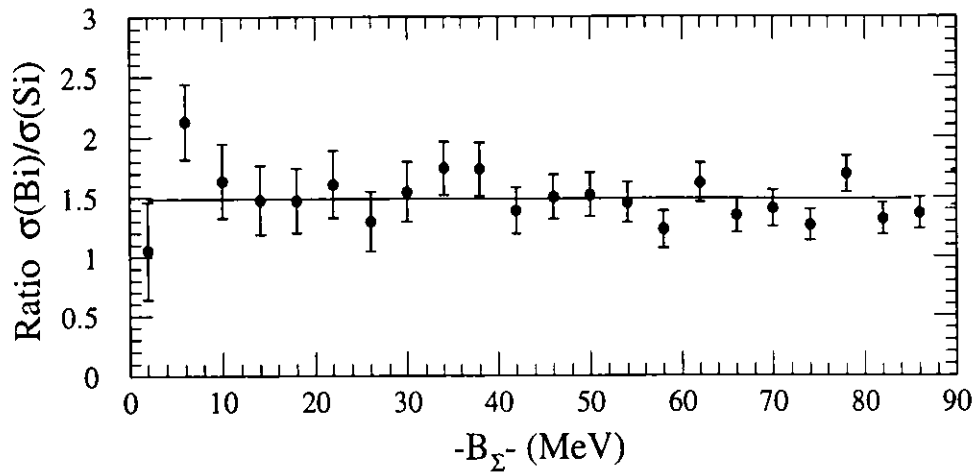
Figure 5.5: Ratio of the cross section, $\left(\frac{d^2\sigma}{d\Omega dE}\right)_{Bi,SKS272A} \Big/ \left(\frac{d^2\sigma}{d\Omega dE}\right)_{Si,SKS272A}$

5.3.1 Comparison of the mass number dependence to the eikonal approximation

The effective nucleon number(N_{eff}) of the (π^-, K^+) reaction on C, Si, Ni, In and Bi target at 6° is calculated by the eikonal approximation [45]. Procedure of the eikonal approximation is summarized in Appendix C.

In the figure 5.6, the present experimental data are shown together with the eikonal approximation. The horizontal axis is in terms of target mass number where the vertical axis shows the ratio.

Mass number dependence of the cross section for the (π^-, K^+) reaction is found to be rather weak in the present data as seen in the figure 5.6. The mass number dependence of the present data is fitted by a function of $C_A \times A^\alpha$ where C_A is a constant and α is the fitting parameter. The value of α is found to be 0.20±0.04. The value of α can reflect the effect of distortion. The present data shows the stronger distortion than that in the eikonal approximation.

The ratio of the inclusive (π^+, K^+) spectra on Fe to C was presented by Akei *et al.*[46]. The ratio was found to be 2.2 ± 0.22. Analysis of our measured (π^+, K^+) data also shows a similar result. Measured (π^+, K^+) spectra together with the obtained result and discussion are presented in Appendix B.
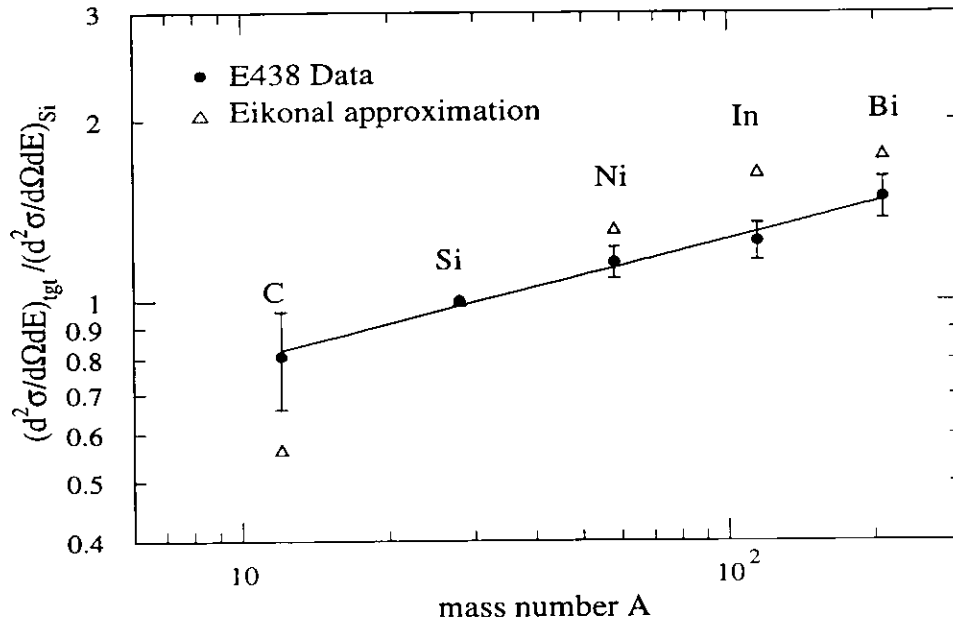
Figure 5.6: Mass number dependence of the cross section $(0 < -B_{\Sigma^-} < 90$ MeV) compared to the eikonal approximation. The quoted errors in the data are statistical.

5.4 Shape of the Si spectrum by a Monte-Carlo simulation

A Monte-Carlo simulation of the quasi-free Σ^- production in the (π^-, K^+) reaction on Si target has been done to see whether the simulation can reproduce the measured spectrum. In the calculation, the reaction is treated as two body collision of π^- to bound proton for simplicity, where the present experimental π^- beam momentum distribution (figure 3.3) is used. The energy resolution of the SKS obtained in the present experiment is also taken into account. A brief procedure of the simulation is summarized in the Appendix D, however, the detail description can be found in the Ref. [42].

To simulate the bound proton, we took the 4-momentum of the target proton, $\tilde{P} = (m_p - B_p, \vec{P}_f)$, where m_p is the mass of proton, B_p is the binding energy of proton in the nucleus and $\vec{P}_f$ is the Fermi momentum.

The total cross section and the angular distribution of the $p(\pi^-, K^+)\Sigma^-$ reaction were measured with bubble chamber in 1960's [44, 47, 48] and presented as a function of the center mass energy, $\sqrt{s}$. In the present simulation, we quoted the kaon's scattering angle distribution and the total cross section from those references. The detail procedure of this calculation is summarized in the Appendix D.

Figure 5.7 shows a comparison of simulated Si spectra to the observed one. The absolute value of the simulated spectrum is scaled to N_{eff}, a half of N_{eff} or a quarter of N_{eff}, which is obtained by the eikonal approximation (table C.1). The difference of the simulated spectrum to the observed one can be found; the present simple model calculation does not reproduce the measured spectral shape. Particularly, the shape above the Σ^- production threshold seems too steep in the simulated spectrum. This discrepancy may be caused by the finite Σ^--nucleus potential as no final state interaction of Σ^- to the residual nucleus is considered so as no Σ^--nucleus optical potential is assumed in the simulated spectrum. In the observed spectrum, the intensity near the binding energy threshold seems to be much suppressed. A repulsive Σ-nucleus potential may give such a suppression around the binding energy threshold. The effect of distortion which is expressed as N_{eff} in the simulated spectrum seems much stronger in the observed spectrum. Suppression of the cross section may be caused by a repulsive Σ-nucleus potential as well as stronger distortion effect than we expected.

Figure 5.7: Observed Si spectrum compared with simulated spectra. The data represents by the black circles with both the statistical and the systematic errors. Lines are the simulated Si spectra changing the value of N_{eff} as quoted in the figure. The value of N_{eff} is obtained from the eikonal approximation (table C.1).
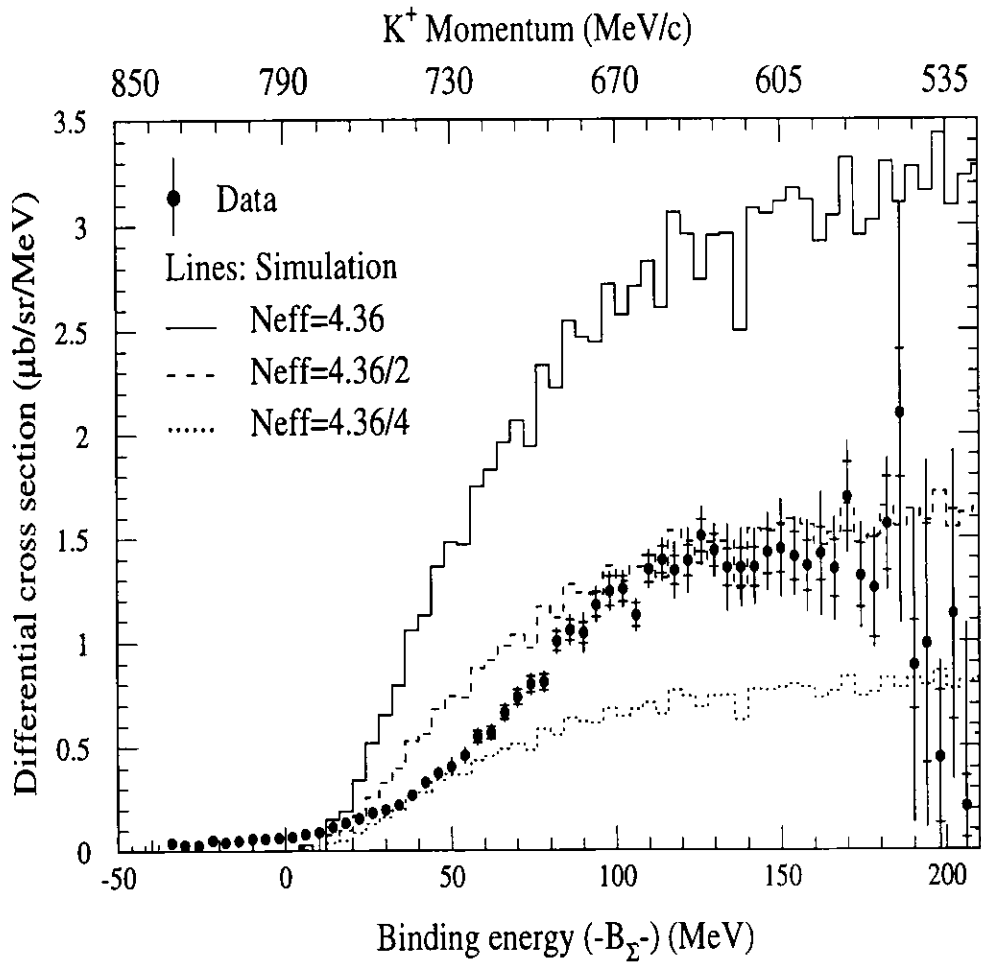
5.5 Comparison of the observed Si spectrum to the DWIA calculation (I)

As shown in chapter 1 (figure 1.12, 1.13), Si spectra using two typical types of potential, namely, 'ND', and 'BATTY' have been calculated [31]. Here we compare the observed spectral shape to those calculated spectra. The potential 'ND' represents an attractive real part and moderately absorptive imaginary part and is based on the one boson exchange potential(OBEP) describing the two-body YN interaction, whereas the potential 'BATTY' represents a strongly repulsive real part and deeply absorptive imaginary part and is obtained from the Σ^--atomic X-ray data. The calculation was done in the framework of DWIA using the (π^-, K^+) reaction. The DWIA framework has been used to calculate the cross sections of the bound Λ hypernuclear states produced by the (π^+, K^+) or (K^-, π^-) reaction [49]. The DWIA is also used to calculate the continuum spectra in intermediate-energy hadron reactions, such as $(p, \acute{p})$, (p, n) and so on. At first, we compared the spectral shape with existing calculation. Comparison of the observed spectrum with calculated spectra (ND and BATTY) is shown in figure 5.8.

Since the strength of the distortion effect needs to be optimized, as already discussed in section 5.3.1 we compare the spectral shape only. The vertical axis in each comparison is thus an arbitrary unit. The solid line spectrum in the figure 5.8(up and down) represents the result based on each original potential, proposed by 'ND' and 'BATTY', respectively. It is clearly seen from the comparison that none of the calculated spectra can reproduce our observed spectral shape. Particularly, the peak position of the observed spectrum is much shifted to the higher excitation energy from both of the calculated one. We found that a repulsive potential (BATTY) pushes the spectral shape towards the higher excitation energy. The peak position is found to be shifted towards the higher energy region in figure 5.8(down) compared to that of using an attractive type potential in figure 5.8(up), in the calculation. The strength around the peak region is found to be much suppressed in case of a repulsive potential in figure 5.8(down) but increases below the binding energy threshold which could be due to the large imaginary part appeared in the original repulsive potential(BATTY,figure 1.12). Then, the depth of the imaginary part of the potential in each case was changed arbitrarily in order to see the change of the spectrum. The spectra using different imaginary values are shown by the broken and dotted lines in each figure. The strength of the spectrum, particularly, below the binding energy threshold is found to be very sensitive to the choice of the imaginary depth but none of the spectrum within this variation could reproduce our observed spectral shape.
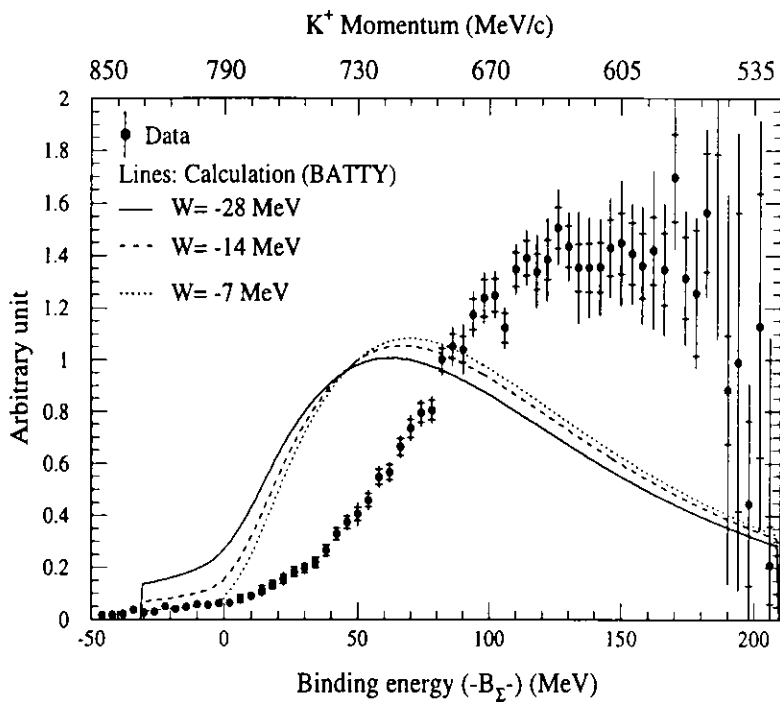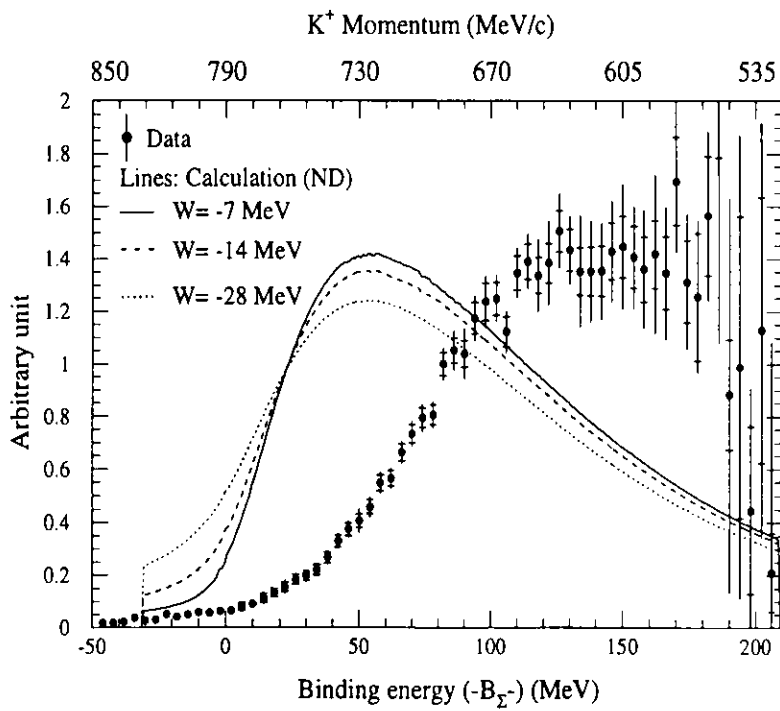
Figure 5.8: Comparison of the observed Si spectrum with calculated spectra. The calculated spectra in the top and bottom figures represent an attractive and a repulsive Σ-nucleus potential, respectively, whereas the broken line and dotted line in each figure correspond to different depth of the imaginary part changed artificially from the original potentials(solid line).

As for the DWIA, we suggest that the elementary amplitude may have a excitation energy dependence since the center of mass(CM) energy of the scattered kaon and produced Σ^- is different in different excitation energy. The elementary cross section is gradually decreasing with the increase of the CM energy (figure 1.14). The shape of the calculated spectrum would be change if we take into account this effect. We found that the parameterization of the distortion effect for the incoming pion and outgoing kaon, expressed as the isospin-averaged total cross section, πN and KN are also needed to be optimized although these effects are found rather weak for the spectral shape but significant for the absolute value of the cross section (see eikonal approximation in Appendix C). Taking into account these effects, Si spectrum has been calculated in the framework of DWIA which is described in the next section.

5.6 Comparison of the Si spectrum to the DWIA calculation (II)

In order to reproduce the observed Si spectrum, another DWIA calculation has been made [50]. In this calculation the excitation energy dependence of the elementary amplitude is taken into account, as already mentioned as a suggestion for the DWIA in the previous section. At first, the Si spectrum has been calculated for the density-dependent potential proposed by Batty et al. [22], from a phenomenological study of the Σ^- atomic X-ray data. The potential has a strong repulsive core in the real part(V_Σ) and deeply absorptive imaginary part(W_Σ), as seen in figure 5.9 (solid lines). The calculated Si spectrum is shown in the figure 5.10, where it is compared with the previous calculation (dotted line) which also used the same potential. As seen from the comparison, the peak position of the present spectrum is found to be much shifted to the higher excitation energy region and the strength near the binding energy threshold is suppressed compared to the previous one. Then by increasing the strength of the repulsive core of V_Σ from the original potential by a factor of two and four, Si spectra are calculated in order to see the response of the spectral shape with respect to the change and is shown in figure 5.11 by broken line and dotted line, respectively, together with the original one(solid line). The observed Si spectrum is also plotted for comparison. It is found that none of the calculated spectra could reproduce the observed spectral shape and an increase of the strength of repulsive core of the potential is found to suppress the strength of the whole spectrum without changing the shape itself.

Next, the calculation is made for a Woods-Saxon type potential $U_\Sigma(r)$, where
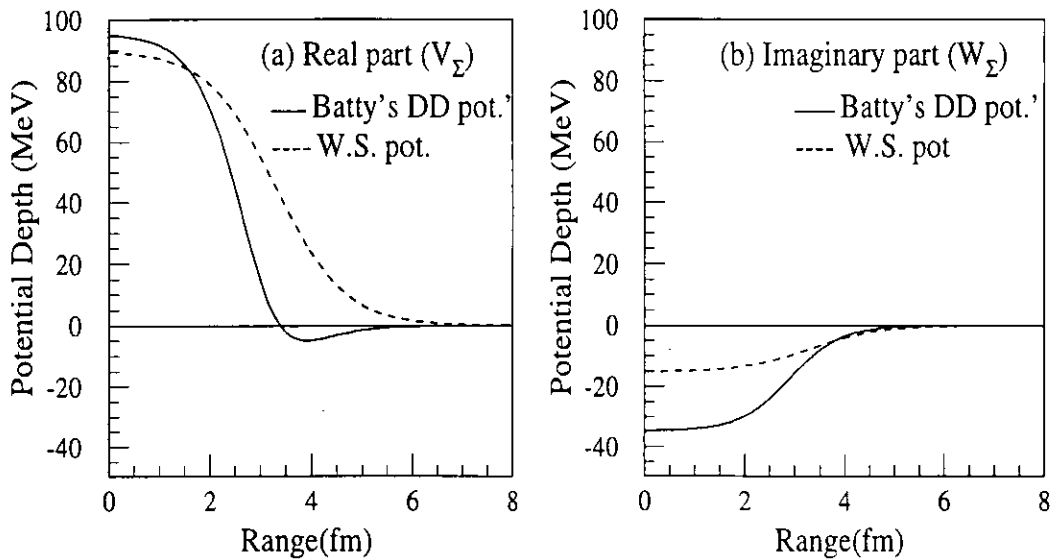
Figure 5.9: Real(a) and imaginary(b) parts of Batty's DD potential (solid lines) together with the present Woods-Saxon type potential(broken lines).

$U_\Sigma(r) = (V_\Sigma + iW_\Sigma)f(r)$. Here, $f(r)$ represents the Fermi function. The range parameter is chosen to be 3.3 fm by the formula, $1.1(A-1)^{\frac{1}{3}}$ and the diffuseness parameter was chosen to be 0.67, where the strength of the imaginary part, W_Σ is -15 MeV. The radial distribution of the potential is plotted in figure 5.9 (broken lines), where the depth of the real part $V_\Sigma = 90$ MeV is as an example. By using different depth of the real part V_Σ, from 10 MeV to 410 MeV with an interval of 20 MeV, Si spectra has been calculated and some of them are shown in figure 5.12. Calculated spectrum for each V_Σ is labelled in the figure. As seen in the figure, an increase of the strength of repulsive core (V_Σ) changes the spectral shape, where the peak position is found to be gradually moved to the higher excitation energy side by suppressing the strength. Then the observed spectrum is tried to fit by these calculated spectra with a function of $C \times F(-B_{\Sigma^-})$, where $F(-B_{\Sigma^-})$ represents a calculated spectrum and C is a free parameter. The vertically free parameter C is introduced because we already found that the distortion effect is much stronger to that obtained in the eikonal approximation (figure 5.6) which is related to the vertical height of the spectrum. At this stage, we are comparing only the spectral shape. In figure 5.13 some of the fitted curves by different lines on the observed spectrum are shown. The fitting χ^2 is observed in every case. The χ^2 value for each corresponding fitting is summarized in table 5.2. By looking χ^2 values it is found that calculated spectra

105
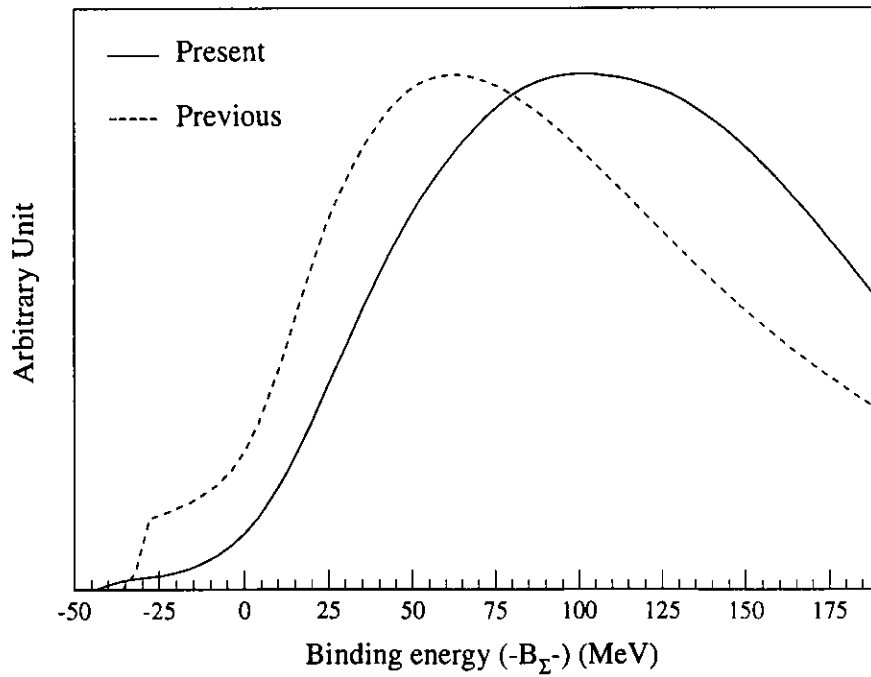
Figure 5.10: Calculated Si spectrum by taking into account the effect of the energy dependence of the elementary cross section(solid line) and compared with the previous calculation(broken line). Absolute values of the cross section is arbitrary in both case.
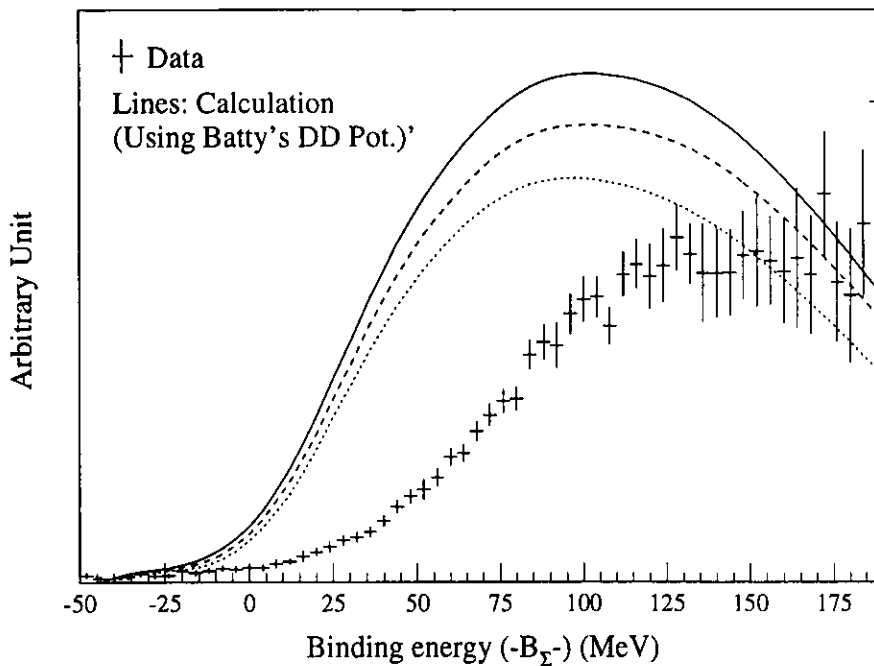
Figure 5.11: Observed Si spectral shape is compared with the present calculated spectra by using Batty's DD potential where the strength of the repulsive core of the potential is increased by a factor of two(broken line) and four(dotted line) from the original one(solid line).

with V_Σ in between $90 \sim 250$ MeV seem to give reasonable description. The confidence level of each fitting is also calculated from the χ^2 value and is found that the calculated spectra by $V_\Sigma < 70$ MeV or $V_\Sigma \geq 310$ should be regarded to be excluded. A different depth of the imaginary part (W_Σ) may optimize the accepted region in a better way. As trials, the present calculation is extended by changing the depth of the imaginary part(W_Σ) to several values, like, -10, -20, -25, -30, -35 and -40 MeV, where the real part is also changed to several values for each W_Σ. Every time the observed spectral shape is tried to fit by the calculated spectrum. Fitted χ^2 values in each case are plotted as a function of V_Σ for the corresponding value of W_Σ and is shown in figure 5.14. Different symbol in the figure represents the corresponding value of W_Σ used in the calculation. From this test it is found that calculated spectra with $W_\Sigma = -15$ MeV give the best χ^2 values and at $V_\Sigma = 150$ MeV but very close at the region of $V_\Sigma = 150 \pm 40$ MeV. As seen in the table 5.2, χ^2 values are found to be significantly improved with $V_\Sigma > 70$ MeV and again increased with $V_\Sigma > 250$ MeV. Spectra by using $W_\Sigma = -10$ MeV give minimum χ^2 values at a region of $V_\Sigma = 210 \pm 40$ MeV, but an unexpected shape is found at around $V_\Sigma = 150$ MeV. By using $W_\Sigma = -20$ MeV a similar trend like $W_\Sigma = -15$ MeV is found but χ^2 values are a bit higher than the later one. The cases of $W_\Sigma \leq -35$ MeV seem to be unacceptable.

From the present study it is thus understood that a strong repulsive Σ-nucleus potential with a finite imaginary part is favorable in reproducing the measured spectral shape. The present calculation suggests that not only bound states but also highly excited states seem to be suppressed. This means that overlapping of the initial state to the final state of upto fairly large angular momentum is suppressed. In case of Batty's repulsive potential, calculated spectra failed to reproduce the observed spectrum. In Batty's potential, the range of the repulsive core is shorter than that of the Woods-Saxon type potential. As a result, relatively, smaller angular momentum Σ^- states would be still contribute to the spectrum. For more quantitative discussions, further theoretical studies are necessary. Theoretical treatment of the distortion effect has to be optimized in order to reproduce absolute value of the cross section. Then allowed region in V_Σ and W_Σ would be much narrower. Calculations for the other targets have yet to be done. From the mass number dependence, the contribution of the iso-vector term in the potential may be extracted. The effect of the Coulomb potential would be interesting in heavy target, where the Coulomb-Assisted Hybrid states (CAHBS) are discussed ([33, 34]). More theoretical works are required to consistently explain the present result and the past data, such as the Σ^--atomic X-ray data, YN interaction and so on.
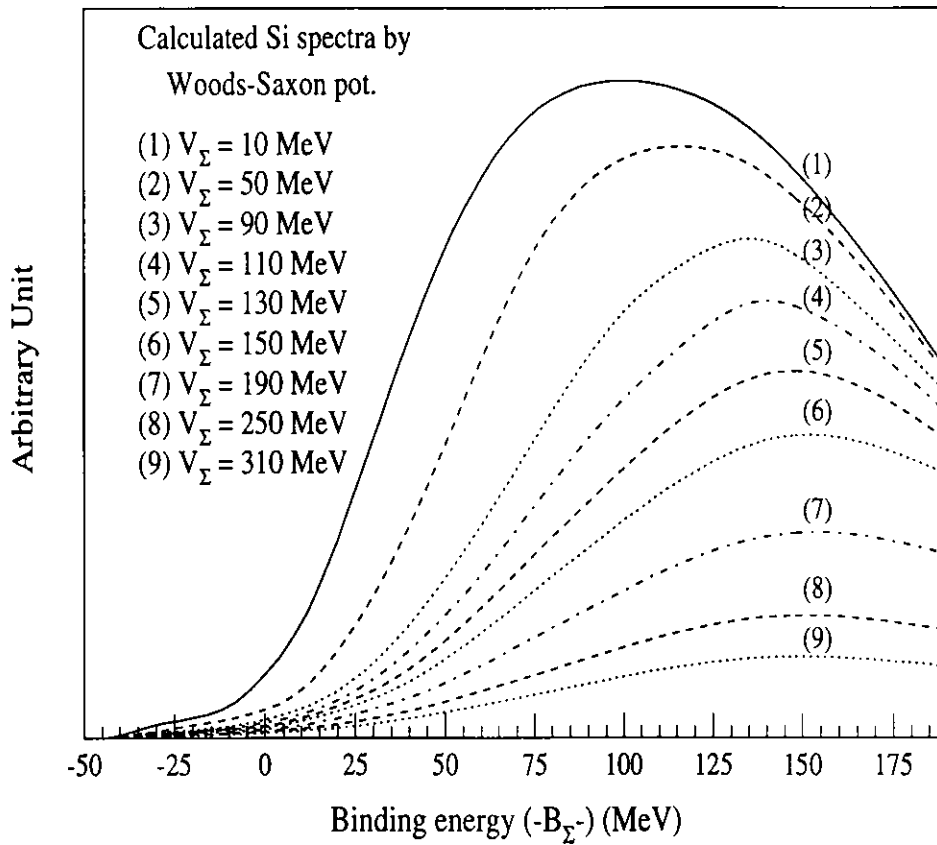
Figure 5.12: Calculated Si spectra by using Woods-Saxon type potential, where the strength of repulsion of the real part is changed by several values as labelled in the figure. The imaginary part of the potential, $W_\Sigma = -15$ MeV. The peak position is found to be gradually moved to the higher excitation energy region suppressing the strength of the spectrum by the increase of the strength of repulsion.
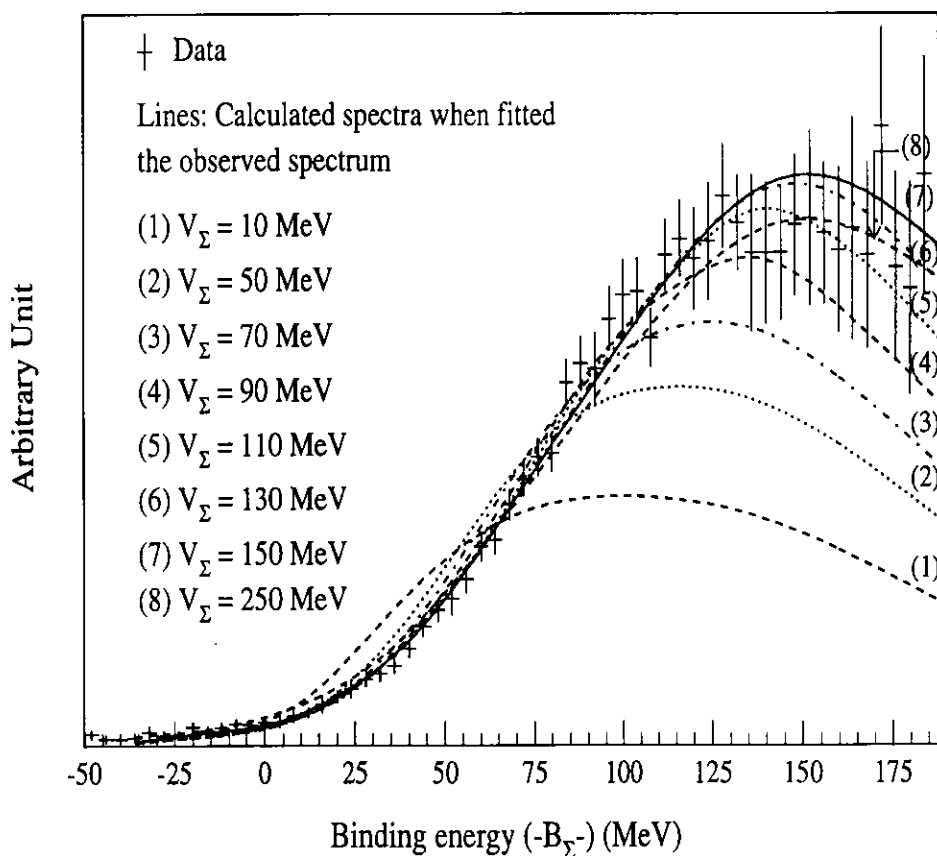
Figure 5.13: Measured Si spectrum is fitted by the calculated spectra(lines). Different line of the calculated spectrum represents the corresponding spectrum with different V_Σ as labelled in the figure, where the imaginary part of the potential, $W_\Sigma = $ -15 MeV in all cases. Calculated spectra with $V_\Sigma \geq$ 90 MeV seem to give reasonable description.

Table 5.2: Fitted χ^2 value of the observed spectrum by the calculated spectra for different V_Σ with W_Σ = -15 MeV.

V_Σ(MeV)	χ^2 (ndf=56)	V_Σ(MeV)	χ^2 (ndf=56)
10.0	870.90	230.0	50.920
30.0	549.70	250.0	61.601
50.0	292.40	270.0	74.090
70.0	133.80	290.0	88.401
90.0	60.570	310.0	102.30
110.0	37.720	330.0	116.01
130.0	33.730	350.0	129.04
150.0	33.420	370.0	140.85
170.0	33.890	390.0	151.76
190.0	36.550	410.0	160.67
210.0	41.980		
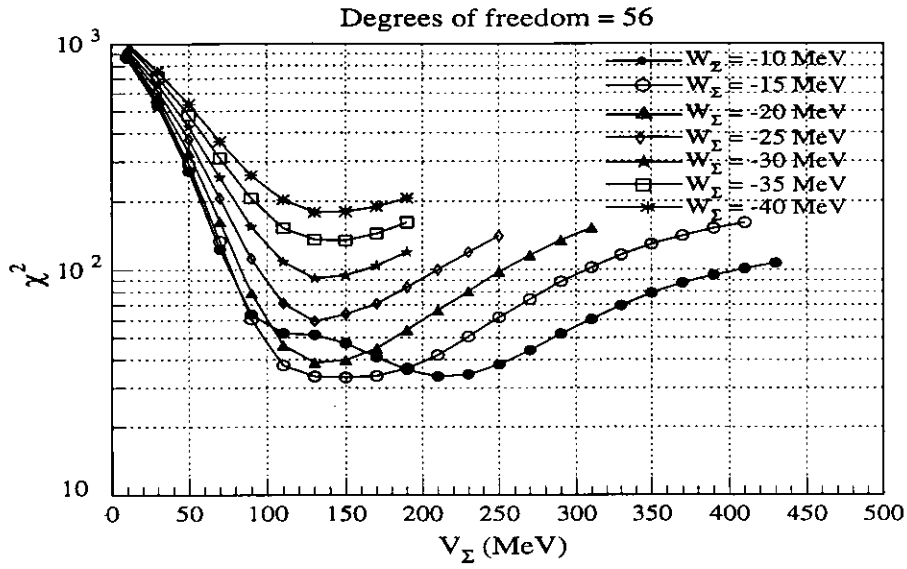
Figure 5.14: Fitted χ^2 values as a function of V_Σ in each value of W_Σ in the present calculation.

110

Chapter 6

Summary and Conclusion

In order to obtain a conclusive understanding about the Σ-Nucleus potential, we have measured the inclusive (π^-, K^+) spectra at the beam momentum of 1.2 GeV/c on various nuclear targets from medium to heavy with reasonably high statistics and for the first time.

In this thesis, inclusive spectra on C, Si, Ni, In and Bi at $\theta_K = 6° \pm 2°$ are presented. The calibration of the energy scale was done successfully using the elementary $p(\pi^-, K^+)\Sigma^-$ reaction from the CH_2 target. We found the precision of the energy scale was as good as ± 0.1 MeV. The energy resolution using only the CH_2 target was obtained to be 1.93 ± 0.08 MeV/c^2. The cross section of the elementary process agreed very well with each set of data within the errors, which proved our understanding of the SKS acceptance and precise determination of experimental efficiencies and moreover, reflected the reliability of the absolute cross section for all the inclusive spectra. The angular distribution of the elementary process obtained from this experiment agreed well with the previous bubble chamber data improving the statistics very much.

The shape of all the inclusive spectra were found to be similar in the region of $-B_{\Sigma^-} < 90$ MeV and the mass number dependence of the cross section in this region was found to be rather weak compared to the eikonal approximation.

A Monte-Carlo simulation was also done to obtain the quasi-free Si spectrum. The simulated spectra were found not to reproduce the measured spectral shape. The effect of distortion in the measured spectrum was found to be much stronger than that of calculated one by the eikonal approximation so as to suppress the cross section in the measured spectrum. The inclusive Si spectral shape was compared with the calculated spectra using an attractive(ND) and a repulsive(BATTY) Σ-nucleus potential in the framework of DWIA. We found that both of the calculated spectra did not reproduce the measured one in shape. Particularly, the measured spectrum was found to be shifted towards the higher excitation energy. Energy dependence of the elementary cross section was found to be very sensitive for the spectral shape. Taking into account this effect, another DWIA calculation was done for Si. It was found that the spectral shape was changed significantly in the present calculation from that one in the previous calculation by using the same Σ-nucleus potential in both calculation but still different from the observed one.

Then, by using a Woods-Saxon type potential, Si spectra were calculated, where the depth of the real part(V_Σ) was changed to several values and was extended to several values of the imaginary part(W_Σ) in each set of V_Σ. A χ^2 test was done by fitting the shape of the measured Si spectrum by the calculated spectra to obtain an allowed region of the potential from the present calculation. Strong repulsive potentials of which depth of the real part, $V_\Sigma > 70$ MeV with moderately absorptive imaginary part were found to be favorable in reproducing the observed spectral shape.

Hence, we concluded that the observed inclusive spectra suggest a strong repulsive Σ-nucleus potential with a moderately absorptive imaginary part.

Acknowledgment

Appendix A

Green's Function Method

A.1 Distorted Wave Impulse Approximation (DWIA)

The framework of DWIA is often used to calculate the (π, K) or (K, π) spectra by using the Green's function method. In chapter 1, a very brief description of the Green's function method is introduced. In this appendix, the expressions by the Green's function method in this formalism are summarized. Further detail descriptions can be found in many references ([35, 52], for example).

The double differential cross section in the framework of DWIA for the (π^-, K^+) reaction is expressed by

$$
\frac{d^2\sigma}{d\Omega_{K+}dE_{K+}} = \beta \cdot \left(\frac{d\sigma}{d\Omega_{K+}}\right)_{ele} \cdot S(E) ,
\tag{A.1}
$$

where β is the kinematical factor, $\left(\frac{d\sigma}{d\Omega_{K+}}\right)_{ele}$ is the Fermi-averaged differential cross section for the elementary process $(\pi^- + p \rightarrow K^+ + \Sigma^-)$, which was discussed in section 5.6. $S(E)$ is the strength function of a hypernuclear system. The kinematical factor β is defined as

$$
\beta = \left\{ 1 + \frac{E_{K+}^{(2)}p_{K+}^{(2)} - p_{\pi^-}cos\theta_{K+}}{E_\Sigma^{(2)}p_{K+}^{(2)}} \right\} \frac{p_{K+}E_{K+}}{p_{K+}^{(2)}E_{K+}^{(2)}},
\tag{A.2}
$$

where $E_{K+}^{(2)}$ and $p_{K+}^{(2)}$ are the total energy and momentum of K^+ in the laboratory system, which is determined by the two body kinematics of free π^-N at the incident momentum, p_{π^-}. As seen in equation A.2, β is not a constant value but proportional to $p_{K+}E_{K+}$. The strength function $S(E)$ can be expressed as

$$
S(E) = \frac{-1}{\pi} Im \sum_{\alpha\alpha'} \int dr \int dr' f_\alpha^+(r) G_{\alpha\alpha'}(E; r, r') f_{\alpha'}(r'),
\tag{A.3}
$$

where $f(\alpha)$ is the form factor characterized with the distorted wave of the incident and outgoing particles and the residual nuclear state and can be expressed as in

116

equation A.4. $G_{\alpha\alpha'}(E; r, r')$ is the Green's function for the Σ-nucleus system in the coupled channels description.

$$f_\alpha(r) = \chi^{(-)*}(R)\chi^+(R) < \alpha|\psi_N(r)|i >, \qquad (A.4)$$

where $R = (M_c/M_{hy})r$. The ket and bra, $|i>$ and $<\alpha|$ represent the states of a target and of a core nucleus, respectively and $\psi_N(r)$ is the annihilation operator of N. The symbols χ^+ and $\chi^{(-)*}$ are the distorted waves of incoming π^- and outgoing K^+, respectively and can be calculated by the eikonal approximation which is described in Appendix C.

The term $< \alpha|\psi_N(r)|i >$ is a proton-hole wave function and can be written as

$$< \alpha|\psi_N(r)|i >= (-1)^{j_\alpha+\mu_\alpha} \phi_{n_\alpha,l_\alpha,j_\alpha}(r)\Phi_{\mu_\alpha}^{(l_\alpha,\frac{1}{2})j_\alpha}(\Omega) \qquad (A.5)$$

The Green's function $G_{\alpha\alpha'}(E; r, r')$ can be expressed as

$$G_{\alpha\alpha'}(E; r, r') = < \alpha|\psi_Y(r)\frac{1}{E - H - i\eta}\psi_Y^+(r')|\alpha' >, \qquad (A.6)$$

where Y stands for the hyperon, here a Σ^-. H can be written as

$$H = T_{nucl-\Sigma} + U_{nucl-\Sigma} + V_{nucl-\Sigma}^{(C)}, \qquad (A.7)$$

where $T_{nucl-\Sigma}$, $U_{nucl-\Sigma}$ and $V_{nucl-\Sigma}^{(C)}$ correspond to the kinetic energy operator, interaction between Σ and the residual nucleus, and the coulomb interaction, respectively.

If $U_{nucl-\Sigma}$ is taken to be a single-particle optical potential, Green's function becomes diagonal with respect to the core nucleus states $|\alpha>$. In the present calculation described in section 5.6, the off-diagonal couplings, $\alpha - \alpha'$ were neglected. The spreading widths of proton-hole states (nuclear core states) and the energy resolution of the detector can be taken into account by putting a finite of η in equation A.6. The Green's function $G_{\alpha\alpha'}(E; r, r')$ can be decomposed into the following form:

$$G_{\alpha\alpha'}(E; r, r') = \sum_{JM} \sum_{l_Y, j_Y, \mu_Y} \sum_{l'_Y, j'_Y, \mu'_Y} (j_\alpha\mu_\alpha j_Y\mu_Y|JM)(j'_\alpha\mu'_\alpha j'_Y, \mu'_Y|JM)$$
$$\times \Phi_{\mu_Y}^{(l_Y,\frac{1}{2})j_Y}(\Omega)\Phi_{\mu'_Y}^{(l'_Y,\frac{1}{2})j'_Y+}G_{\alpha l_Y j_Y,\alpha'l'_Y,j'_Y}^J(E; r, r'), \qquad (A.8)$$

where G^J is given by

$$G_{\alpha l_Y j_Y,\alpha'l'_Y,j'_Y}^J(E; r, r') = < n_\alpha| < r| < JM|\frac{1}{E - H + i\eta}|JM > |r' > |n'_\alpha >, \qquad (A.9)$$

From the angular momentum algebra, the partial-wave decomposition of $S(E)$ can be expressed by the following way:

$$S(E) = \sum_{JM} \sum_{l_Y, j_Y} \sum_{n_N, l_N, j_N} \sum_{l'_Y, j'_Y} \sum_{n'_N, l'_N, j'_N} W(j_N, J_Y, j'_N, j'_Y, J)$$
$$\times S_{(l_Y j_Y, n_N l_N j_N)(l'_Y j'_Y, n'_N l'_N j'_N)}^{JM}(E), \qquad (A.10)$$

117

where,

$$W(j_N, J_Y, j_N', j_Y', J) = \sqrt{(2j_N + 1)(2j_N' + 1)} \; (j_N \tfrac{1}{2} J 0 | j_Y \tfrac{1}{2})(j_N' \tfrac{1}{2} J 0 | j_Y' \tfrac{1}{2}), \quad (A.11)$$

and

$$
\begin{aligned}
S^{JM}_{(l_Y j_Y, n_N l_N j_N)(l_Y' j_Y', n_N' l_N' j_N')}&(E) \\
= \frac{-1}{\pi} &\int dr dr' r^2 r'^2 \tilde{j}^*_{JM}(p_{\pi^-}, p_{K^+}, \theta_{K^+}, r) \phi^*_{n_N, l_N, j_N}(r) \\
&\times G^J_{(l_Y j_Y, n_N l_N j_N)(l_Y' j_Y', n' N l_N' j_N')}(E; r, r') \\
&\times \tilde{j}_{JM}(p_{\pi^-}, p_{K^+}, \theta_{k^+}, r') \phi_{n_N', l_N', j_N'}(r') \quad\quad (A.12)
\end{aligned}
$$

where the function $\tilde{j}_{JM}(p_{\pi^-}, p_{K^+}, \theta_{k^+}, r')$ is known as the distorted spherical wave function and is defined as

$$\chi^{(-)*}\left(p_{k^+}, \frac{M_C}{M_{HY}} r\right) \chi^{(+)}\left(p_{\pi^-}, \frac{M_C}{M_{HY}} r'\right) \quad\quad (A.13)$$

$$= \sum_{J=0}^{\infty} \sum_{M=-J}^{M=J} \tilde{j}_{JM}(p_{\pi^-}, p_{K^+}, \theta_{k^+}, r') Y_J^M \quad\quad (A.14)$$

The detail calculation can be found in ref.[51]. The term $\phi^*_{n_N, l_N, j_N}(r)$ represents the 'hole state' and in the present treatment this is the 'single-particle state'.

For one-body potential, Green's function becomes diagonal and then the strength function $S(E)$ can be expressed as

$$S(E) = \sum_{JM} \sum_{l_Y, j_Y} \sum_{n_N, l_N, j_N} W(j_N, J_Y, J) S^{JM}_{(l_Y j_Y, n_N l_N j_N)}(E) \quad\quad (A.15)$$

where,

$$W(j_N, J_Y, J) = (2j_N + 1)(j_N \tfrac{1}{2} J 0 | j_Y \tfrac{1}{2})^2 \quad\quad (A.16)$$

and

$$
\begin{aligned}
S^{JM}_{(l_Y j_Y, n_N l_N j_N)}&(E) \\
= \frac{-1}{\pi} &\int dr dr' r^2 r'^2 \tilde{j}^*_{JM}(p_{\pi^-}, p_{K^+}, \theta_{K^+}, r) \phi^*_{n_N, l_N, j_N}(r) \\
&\times G^J_{(l_Y j_Y, n_N l_N j_N)} \tilde{j}_{JM}(p_{\pi^-}, p_{K^+}, \theta_{k^+}, r') \phi_{n_N, l_N, j_N}(r') \quad\quad (A.17)
\end{aligned}
$$

where the term $G^J_{(l_Y j_Y, n_N l_N j_N)}$ is the solution of the radial part of the Schrödinger equation in one dimensional, which can be seen in equation 1.7 expressed for three dimensional case.

Then, the double differential cross section as expressed in equation A.1 can be calculated by employing the above quantities. A gross feature of the spectrum can be described by the strength function $S(E)$ in this formalism.

Appendix B

Inclusive (π^+, K^+) reaction

We took some data using the (π^+, K^+) reaction on CH_2&Si to measure the inclusive spectra on ^{12}C and ^{28}Si as shown in table 2.10. The beam momentum was fixed at 1.2 GeV/c. The target setup configuration was the same as in figure 2.19. It is interesting to check the DWIA framework for the inclusive spectra in the present experimental condition as well as to check the consistency of the present experimental results since DWIA framework is already found to be a powerful tool in explaining the inclusive spectra for the (π^+, K^+) reaction at 1.05 GeV/c. The inclusive spectra on C and Si obtained from the present experiment are presented in this Appendix. If the theoretical spectra on C and Si appear using this experimental conditions then we can compare for the quantitative physics discussion. Inclusive spectra using the (π^+, K^+) reaction on ^{12}C and ^{56}Fe was reported in Ref [46]. Ratio of the cross section on ^{56}Fe to ^{12}C was found to be 2.2 ± 0.2. From the present data, the ratio of cross section on ^{28}Si to ^{12}C is also presented here.

Carbon spectrum

The inclusive C spectrum in the $^{12}C(\pi^+, K^+)$ reaction is obtained by selecting CH_2 events as the reaction vertex point and assuming the carbon kinematics and shown in figure B.1. The outgoing kaon's scattering angle is chosen to be same as (π^-, K^+) data (6° ± 2°). The horizontal axis is in terms of the Λ binding energy and the vertical axis is in terms of $\mu b/sr/MeV$. Due to the gating of the elementary process, $p(\pi^+, K^+)\Sigma^+$ from the CH_2 target, the carbon events in that region also rejected, which can be seen as a sharp drop of the spectrum at around 150 MeV from the Λ binding threshold. But it is quite hard to estimate the C contribution separately from the H contribution so as to correct the spectrum over that region. For the present discussion it is not so serious if we neglect to correct that region. The peak position of the C spectrum seems to be appear around 100 MeV from the Λ binding threshold.

119
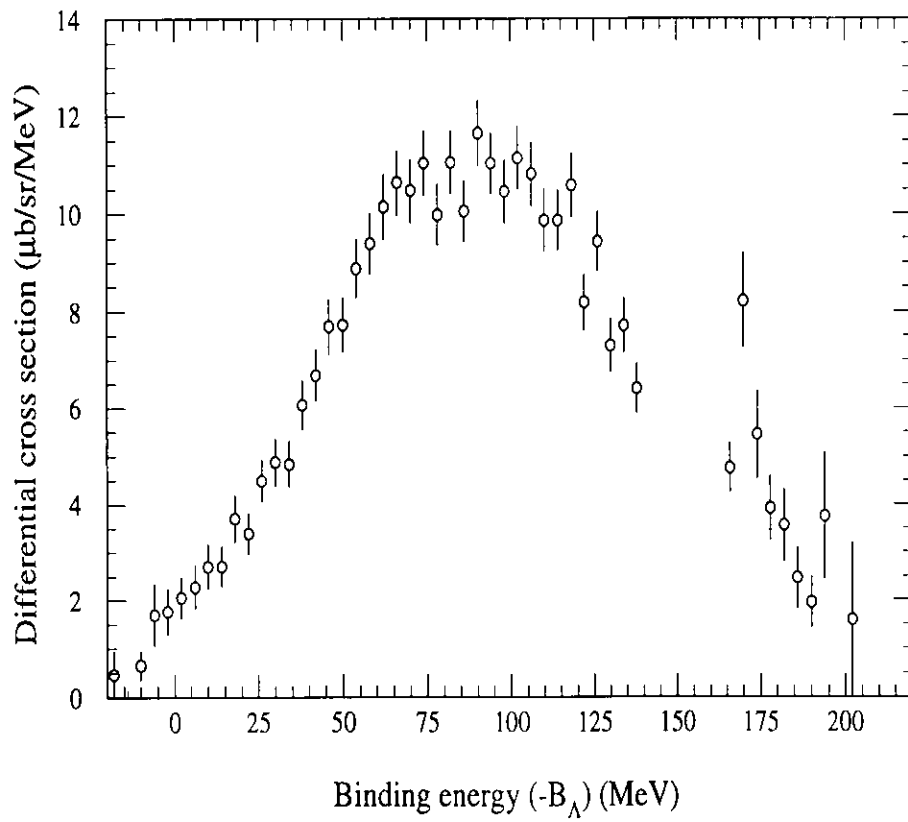
Figure B.1: The $^{12}C(\pi^+, K^+)$ inclusive spectrum from the CH$_2$&Si data. See the text for detail. The quoted errors are statistical.

Silicon spectrum

The inclusive Si spectrum obtained by the ^{28}Si(π^+, K^+) reaction from the CH$_2$&Si data is shown in the figure B.2.
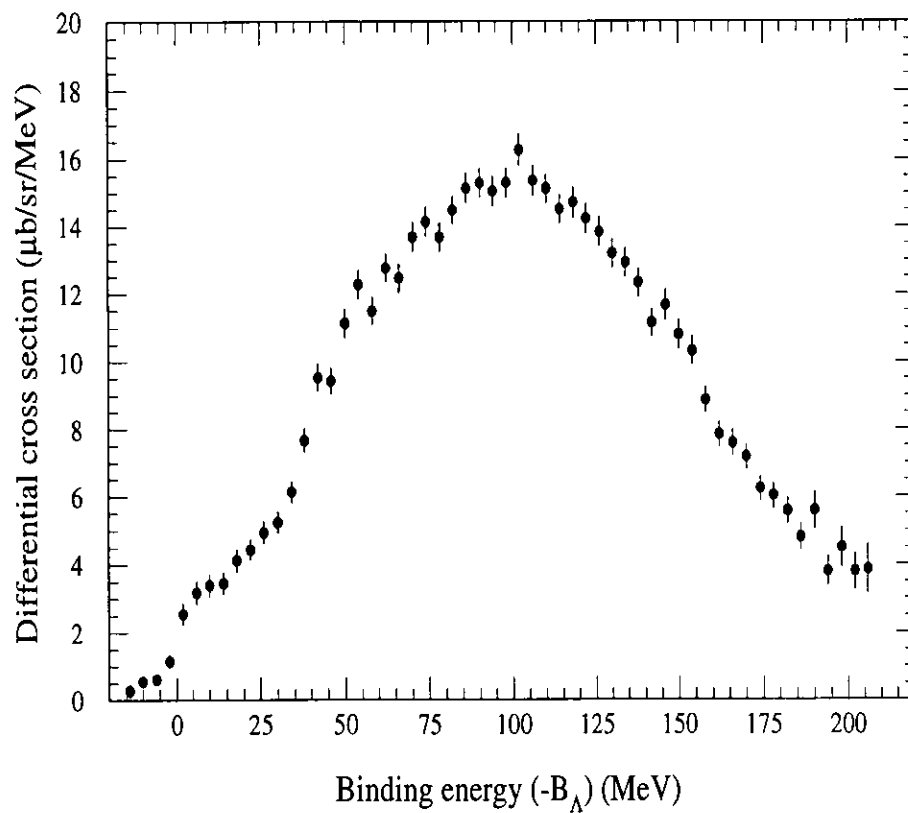
Figure B.2: The ^{28}Si(π^+, K^+) inclusive spectrum from the CH$_2$&Si data. The quoted errors are statistical.

Ratio of the cross section

Figure B.3 shows the ratio of cross section obtained from Si to C as a function of the scattered kaon momentum rather than a function of the excitation energy so that it can be compared more directly free from the binding energy effect as was also reported in ref [46]. The ratio is found constant over a wider momentum region and is 1.475 ± 0.14. The quoted error are statistical. Taking the ratio of Fe to C as 2.2 from the previous measurement [46], the ratio of Si to C is calculated to be ~ 1.5 assuming the mass number dependence of A^{α}. So the present value agrees well with the previous measurement within the statistical error.
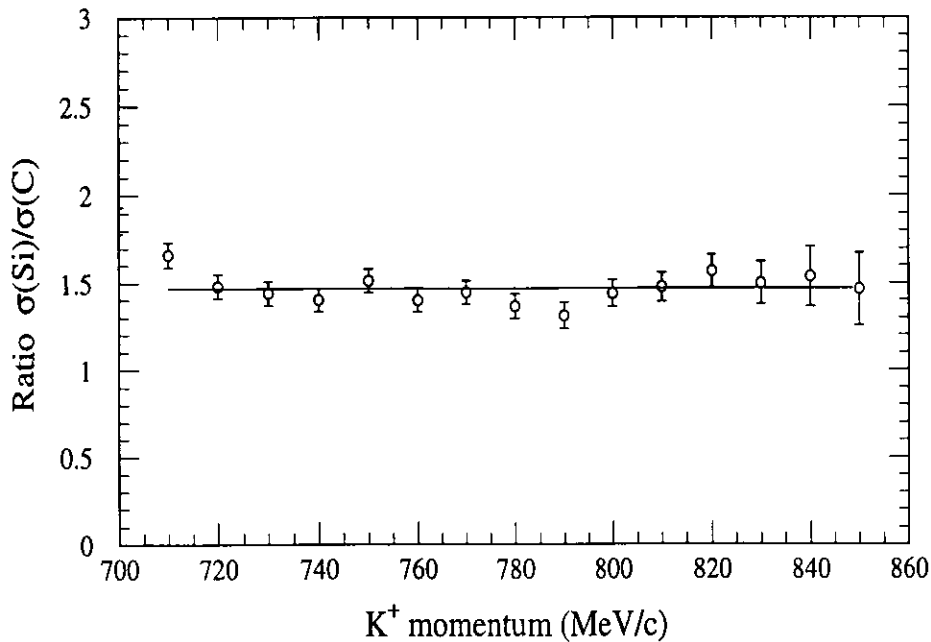
Figure B.3: Ratio of the cross section, $\left(\frac{d^2\sigma}{d\Omega dP_K}\right)_{Si} / \left(\frac{d^2\sigma}{d\Omega dP_K}\right)_C$ as a function of scattered kaon momentum. The quoted errors are statistical.

Appendix C

Here, the calculation of the effective nucleon number N_{eff} in the eikonal approximation is mentioned.

Brief procedure to estimate N_{eff} by the eikonal approximation

At first, definitions of some used parameters are summarized below.

$$\begin{array}{rcl}
\rho_N(\mathbf{r}) & : & \text{nucleon density} \\
\mathbf{k}_\pi, \ \mathbf{k}_K & : & \text{wave number of a target proton} \\
 & & \text{(Its unit vector is indicated by '\^'.)} \\
v_\pi, \ v_K & : & \text{velocity of pion and kaon} \\
U_{\pi N}, \ U_{KN} & : & \text{pion-nucleus and kaon-nucleus optical potential} \\
b, \ z & : & \text{components of } \mathbf{r} \\
\gamma_\pi, \ \gamma_K & : & \mathrm{Re}\overline{f_{\pi N}}(0)/\mathrm{Im}\overline{f_{\pi N}}(0) \text{ and } \mathrm{Re}\overline{f_{KN}}(0)/\mathrm{Im}\overline{f_{KN}}(0) \\
\overline{f_{\pi N}}(0), \ \overline{f_{KN}}(0) & : & \text{isospin-averaged forward elementary amplitude} \\
\bar{\sigma}_{\pi N}^{tot}, \ \bar{\sigma}_{KN}^{tot} & : & \text{isospin-averaged total cross section of } \pi N \text{ and } KN \text{ reaction}
\end{array}$$

The effective nucleon number N_{eff} can be calculated by integrating the nucleon density distribution. In the reaction, pion and kaon passes a finite path in a nucleus as figure C.1 suggests. Then the absorption of incoming pion and outgoing kaon in the nucleus will reduce N_{eff}. In the eikonal approximation, N_{eff} is defined as follows.

$$N_{eff} = \int \rho_N(\mathbf{r}) |\chi_K^{(-)}(\mathbf{r}, \mathbf{k}_K)|^2 |\chi_\pi^{(+)}(\mathbf{r}, \mathbf{k}_\pi)|^2 d^3\mathbf{r} \tag{C.1}$$

where $\chi_\pi^{(+)}$ and $\chi_K^{(-)}$ are the distorted waves of incoming pion and outgoing kaon, respectively [52]. Using the toroidal coordinate system (figure C.1) and assuming $z_1 = \hat{\mathbf{k}}_\pi \cdot \mathbf{r}$ and $z_2 = \hat{\mathbf{k}}_K \cdot \mathbf{r}$, we can write the distorted waves as:

$$\chi_\pi^{(+)} = \exp\left[i\mathbf{k}_\pi \cdot \mathbf{r} - \frac{i}{v_\pi} \int_{-\infty}^{z_1} U_{\pi N}(b_1, z')dz'\right] , \tag{C.2}$$

$$\chi_K^{(-)} = \exp\left[i\mathbf{k}_K \cdot \mathbf{r} - \frac{i}{v_K} \int_{z_2}^{\infty} U_{KN}(b_2, z')dz'\right] . \tag{C.3}$$

Reaction point can be denoted as $(b_\pi, z_\pi) = (b_1, z_1)$ and $(b_K, z_K) = (b_2, z_2)$ where (b_π, z_π) and (b_K, z_K) are coordinate defined as in figure C.1. $U_{\pi N}$ and U_{KN} are
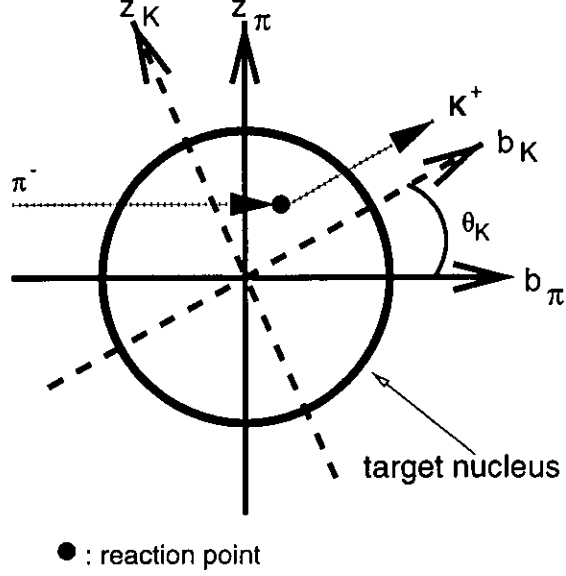
Figure C.1:(π, K) reaction in a nucleus.
Reaction point can be denoted as $(b_\pi, z_\pi) = (b_1, z_1)$ and $(b_K, z_K) = (b_2, z_2)$.

given by

$$U_{\pi N} \approx -i\frac{v_\pi}{2}\overline{\sigma}_{\pi N}^{tot}(1 - i\gamma_\pi)\rho(\mathbf{r}) \tag{C.4}$$

$$U_{KN} \approx -i\frac{v_K}{2}\overline{\sigma}_{KN}^{tot}(1 - i\gamma_K)\rho(\mathbf{r}) \tag{C.5}$$

γ can be neglected since the differential cross section is insensitive to it [53]. We adopted $\overline{\sigma}_{\pi N}^{tot} = 35$ mb and $\overline{\sigma}_{KN}^{tot} = 14$ mb [53]. As for ρ, following charge density distribution was employed as follows [54].

$$C \quad \rho = \rho_0 \left[1 + 1.067 \cdot (r/1.687)^2\right] \exp\left(-(r/1.687)^2\right) \tag{C.6}$$

$$Si \quad \rho = \rho_0 \left[1 + \exp\left((r - 3.15)/0.537\right)\right]^{-1} \tag{C.7}$$

$$Ni \quad \rho = \rho_0 \left[1 + \exp\left((r - 4.309)/0.517\right)\right]^{-1} \left(1 - 0.131 \cdot (r/4.309)^2\right) \tag{C.8}$$

$$In \quad \rho = \rho_0 \left[1 + \exp\left((r - 5.357)/0.563\right)\right]^{-1} \tag{C.9}$$

$$Bi \quad \rho = \rho_0 \left[1 + \exp\left((r - 6.75)/0.468\right)\right]^{-1} \tag{C.10}$$

where ρ_0 is normalization factor as to make $4\pi \int \rho(\mathbf{r}) \cdot r^2 dr = A$.

Furthermore, if we use following ρ_N^{nlj} as a nucleon density distribution, N_{eff} can be obtained state by state.

$$\rho_N^{nlj}(\mathbf{r}) = |\phi^{nlj}(r)|^2 \times N^{nlj} \tag{C.11}$$

where $\phi^{nlj}(r)$ and N^{nlj} are the radial-wave function and number of nucleons occupying the state [nlj]. Results obtained by this calculation for different targets are presented in the figure 5.6. In table C.1 calculated results are summarized.

Table C.1: N_{eff} for each state at $\theta_K = 6°$ by the eikonal approximation ([45]).

state	C	Si	Bi
$0s_{1/2}$	0.66	0.40	0.07
$0p_{3/2}$	1.81	1.15	0.20
$0p_{1/2}$	—	0.55	0.09
$0d_{5/2}$	—	2.26	0.41
$0d_{3/2}$	—	—	0.24
$1s_{1/2}$	—	—	0.12
$0f_{7/2}$	—	—	0.71
$0f_{5/2}$	—	—	0.45
$1p_{3/2}$	—	—	0.33
$1p_{1/2}$	—	—	0.16
$0g_{9/2}$	—	—	1.10
$0g_{7/2}$	—	—	0.73
$1d_{5/2}$	—	—	0.66
$1d_{3/2}$	—	—	0.41
$0h_{11/2}$	—	—	1.62
$2s_{1/2}$	—	—	0.23
$0h_{9/2}$	—	—	0.11
total	2.47	4.36	7.64

Appendix D

Brief procedures of the Monte-Carlo simulation for the quasi-free Si spectrum are summarized here.

The Fermi motion of proton in a target nucleus was put on by assuming proton's momentum distribution. For a nucleon in silicon nuclei, radial wave functions $\Psi(r)$ and binding energies were calculated by solving the Schrödinger equation (equation D.1).

$$\left(-\frac{\hbar^2 \nabla^2}{2m_p} + U(r)\right) \Psi(r) = E\Psi(r) \tag{D.1}$$

$$U(r) = V_0 \cdot f(r) + V_{LS} \left(\frac{\hbar}{m_\pi c}\right)^2 \frac{1}{r} \frac{df(r)}{dr} (l \cdot \sigma) + V_{Coulomb}(r) \tag{D.2}$$

$$f(r) = [1 + \exp((r - c)/z)]^{-1} \tag{D.3}$$

$$V_{Coulomb}(r) = \begin{cases} \dfrac{Z_c \cdot e^2}{r} \left(\dfrac{3}{2} - \dfrac{1}{2}\left(\dfrac{r}{c}\right)^2\right) & (0 < r < c) \\ \dfrac{Z_c \cdot e^2}{r} & (r \geq c) \end{cases} \tag{D.4}$$

where

$U(r)$	:	the single particle potential of a bound proton [55],
$V_0 \cdot f(r)$	:	Woods-Saxon potential of the proton,
V_{SO}	:	spin-orbit potential of the proton (fixed at 7 MeV),
$V_{Coulomb}(r)$	:	Coulomb potential of the proton,
c	:	nuclear radius,
z	:	diffuseness,
e	:	electron charge magnitude,
Z_c	:	charge of core nucleus in unit of e.

V_0 and c were adjusted so as to reproduce the separation energy S_p ($= B_p$ in the outermost orbit) and the r.m.s. radius $\sqrt{\langle r^2 \rangle}$. Momentum distributions $\psi(p)$ was calculated from Fourier transforms of the $\Psi(r)$. Calculated $\phi(p)$ of silicon nuclei are shown in figure D.1.

Binding energy of the target proton B_p for each state is summarized in table D.1.

Since the state-by-state N_{eff} is a simple function of the probability amplitude, we can use values on table C.1 as a ratio of each state in adding state-by-state.
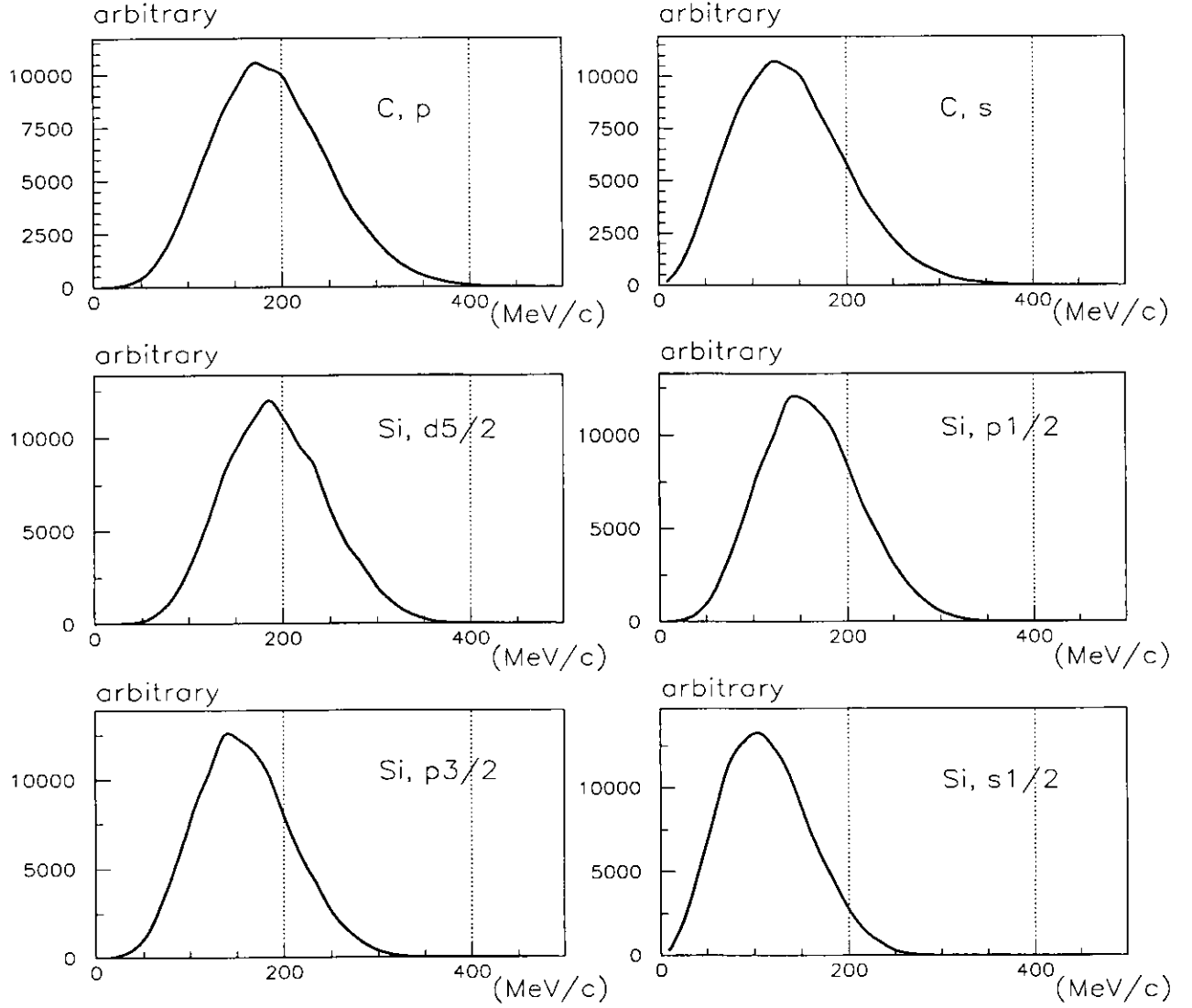
Figure D.1: Proton's momentum distribution in silicon nucleus

Table D.1: B_p of Si in the Monte-Carlo calculation ([45]).

state	B_p of Si [MeV]
$0s_{1/2}$	31.491
$0p_{3/2}$	21.978
$0p_{1/2}$	27.07
$0d_{5/2}$	11.585

Angular distribution of the $p(\pi^-, K^+)\Sigma^-$ reaction

In the 1960's, study of the $(\pi, K)\Sigma$ reactions were performed enthusiastically with bubble chambers as can be found in following references [44, 47, 48]. It is known that the differential cross section of the $p(\pi^-, K^+)\Sigma^-$ reaction has an angular distribution which is denoted as

$$\left(\frac{d\sigma}{d\Omega}\right)_{cm} = \sum_{i=0}^{n} A_n P_n(\cos\theta_{\Sigma\ cm}) \tag{D.5}$$

where $\theta_{\Sigma\ cm}$ is a scattering angle of Σ in the center of mass system, $P_n(\cos\theta_{\Sigma\ cm})$ is the Legendre polynomial and A_n is the coefficient.

In figure 3.29, angular distribution of the elementary process from the CH_2&Si data (SKS at 210A) in the present experiment is presented as a comparison with the bubble chamber data.

$\sqrt{s}$ dependence of the total cross section and angular distribution

In the Monte-Carlo calculation of the quasi-free process, we refereed to the $\sqrt{s}$ dependence of the total cross section and the Legendre coefficients A_n (n = 0 $\sim$ 2) which was outlined by Ref. [44, 47, 48]. Figure D.2 shows the $\sqrt{s}$ corresponding to the beam momentum. Figure D.3 (a) is the $\sqrt{s}$ dependence of the $(\pi^-, K^+)\Sigma^-$-reaction total cross section $\sigma^{tot}_{\pi^- p \to K^+ \Sigma^-}$. Figure D.3 (b), (c) and (d) are those of the Legendre coefficients A_n, where n = 0 to 2. Lines are fitting results which was used in the Monte-Carlo calculation.
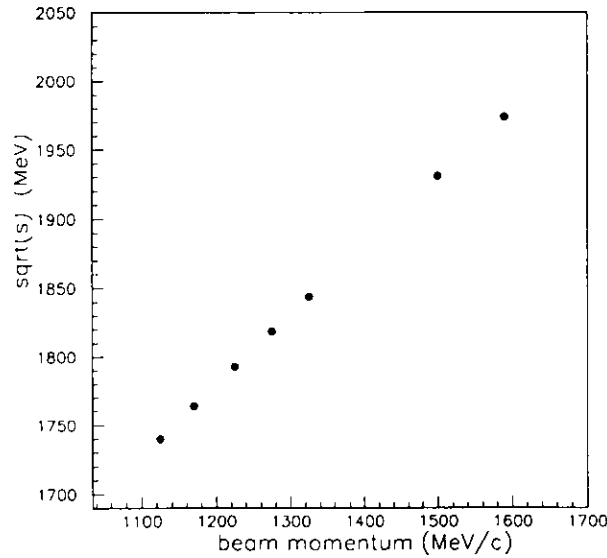
Figure D.2: Beam momentum to $\sqrt{s}$
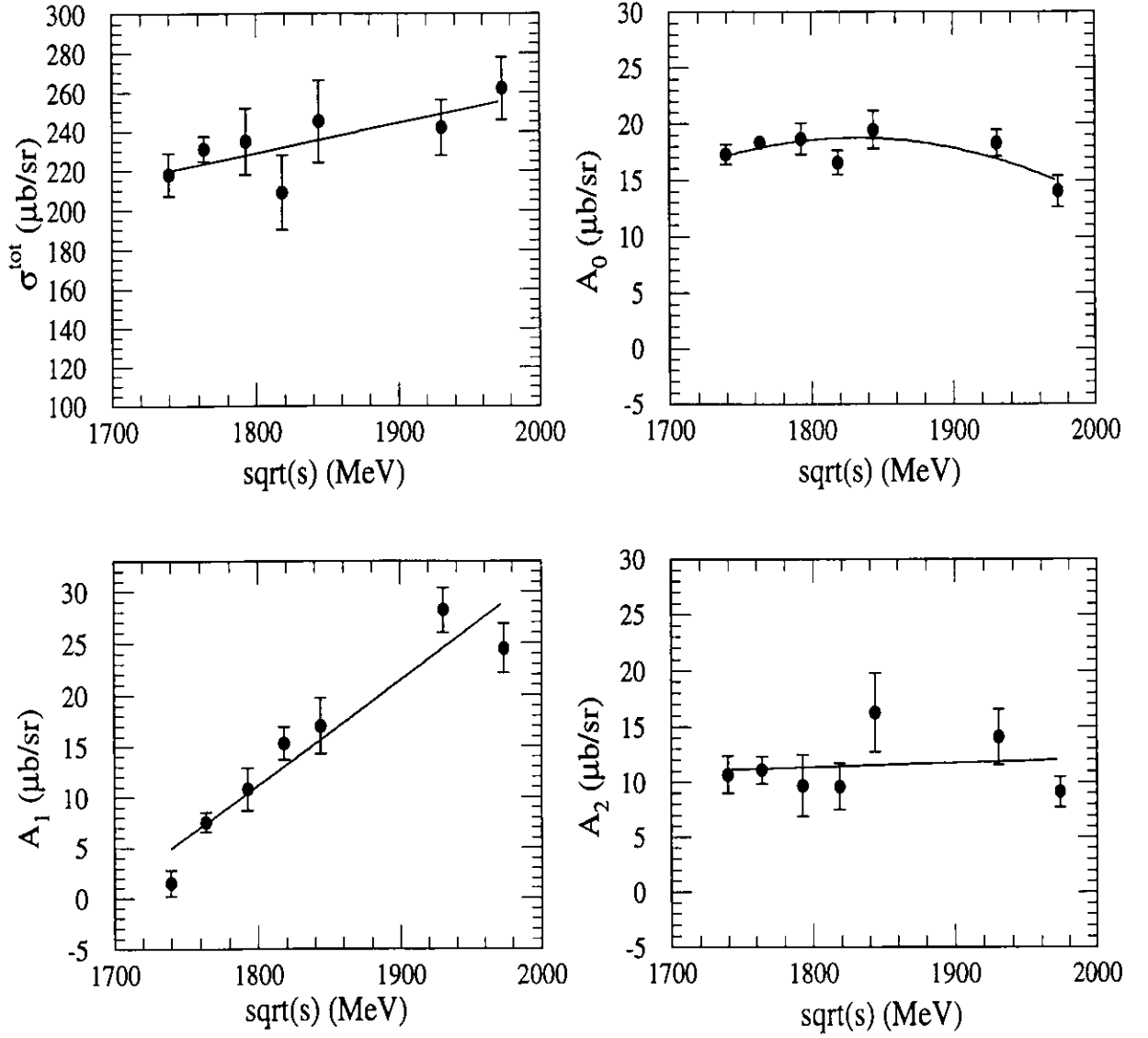
Figure D.3: $\sqrt{s}$ dependence of $\sigma^{tot}_{\pi^- p \to K^+ \Sigma^-}$ and A_n. Fitting result are :

(a) $\sigma^{tot} = (0.1535 \pm 0.0046) \cdot \sqrt{s} + (-47.54 \pm 8.43)$

(b) $A_0 = (-0.00019 \pm 0.0000013) \cdot (\sqrt{s})^2 + (0.71 \pm 0.0031) \cdot \sqrt{s} + (-627.8 \pm 4.3)$

(c) $A_1 = (0.1029 \pm 0.0047) \cdot \sqrt{s} + (-174.0 \pm 8.75)$

(d) $A_2 = (0.00383 \pm 0.0017) \cdot \sqrt{s} + (+4.48 \pm 3.66)$

Appendix E

Inclusive (π^-, K^+) spectra shown in figures 4.5, 4.9, 4.11, 4.13 and 4.18 are presented here as tables E.1, E.2, E.3, E.4 and E.5, respectively. All the spectra were generated by 4 MeV binning and then divided by 4 so as to obtain the cross section in terms of μb/sr/MeV. The quoted values of Σ^- binding energy (B_{Σ^-}) are the center of bins.

Table E.1: The ^{28}Si(π^-, K^+) inclusive spectrum as a table.

-B$_\Sigma$- (MeV)	Cross section (μb/sr/MeV)	Statistical errors	Systematic errors
-50.0	0.0308	0.0127	0.0006
-46.0	0.0174	0.0109	0.0008
-42.0	0.0184	0.0108	0.0003
-38.0	0.0223	0.0115	0.0015
-34.0	0.0375	0.0135	0.0015
-30.0	0.0280	0.0126	0.0005
-26.0	0.0292	0.0113	0.0010
-22.0	0.0503	0.0133	0.0007
-18.0	0.0410	0.0121	0.0005
-14.0	0.0498	0.0126	0.0012
-10.0	0.0598	0.0123	0.0008
-6.00	0.0576	0.0130	0.0010
-2.00	0.0635	0.0136	0.0018
2.000	0.0644	0.0133	0.0032
6.000	0.0804	0.0158	0.0036
10.00	0.0908	0.0147	0.0010
14.00	0.1129	0.0160	0.0087
18.00	0.1335	0.0161	0.0020
22.00	0.1556	0.0172	0.0092
26.00	0.1831	0.0183	0.0039
30.00	0.1974	0.0188	0.0038
34.00	0.2201	0.0192	0.0031
38.00	0.2667	0.0206	0.0039
42.00	0.3287	0.0227	0.0054
46.00	0.3741	0.0241	0.0078
50.00	0.4054	0.0255	0.0200
54.00	0.4594	0.0267	0.0126
58.00	0.5491	0.0287	0.0117
62.00	0.5667	0.0292	0.0100
66.00	0.6636	0.0329	0.0116
70.00	0.7360	0.0352	0.0143
74.00	0.7952	0.0372	0.0144
78.00	0.8061	0.0380	0.0140
82.00	1.0008	0.0448	0.0187
86.00	1.0527	0.0472	0.0271
90.00	1.0397	0.0496	0.0472
94.00	1.1750	0.0594	0.0280
98.00	1.2382	0.0719	0.0251
102.0	1.2491	0.0629	0.0261
106.0	1.1228	0.0564	0.0233
110.0	1.3462	0.0649	0.0311
114.0	1.3898	0.0662	0.0386
118.0	1.3375	0.0674	0.0712
122.0	1.3845	0.0746	0.0842
126.0	1.5055	0.0789	0.0635
130.0	1.4338	0.0788	0.0514
134.0	1.3521	0.0902	0.1235
138.0	1.3523	0.0919	0.1005
142.0	1.3539	0.0950	0.0898
146.0	1.4285	0.1075	0.0842
150.0	1.4456	0.1171	0.1201
154.0	1.4067	0.1179	0.0751
158.0	1.3604	0.1227	0.1016
162.0	1.4187	0.1283	0.1731
166.0	1.3470	0.1384	0.1146
170.0	1.6948	0.1666	0.1028
174.0	1.3139	0.1550	0.1028
178.0	1.2560	0.2420	0.0461
182.0	1.5632	0.2263	0.0946
186.0	2.0955	0.3099	0.0765
190.0	0.8844	0.2094	0.5393
194.0	0.9897	0.5720	0.3064
198.0	0.4460	0.3163	0.1451
202.0	1.1287	0.5051	0.2822
206.0	0.2095	0.1489	0.7257
210.0	0.3247	0.2302	0.1518

Table E.2: The ^{12}C(π^-, K^+) inclusive spectrum as a table.

-B$_{\Sigma^-}$ (MeV)	Cross section (μb/sr/MeV)	Statistical errors	Systematic errors
-50.0	0.0103	0.0166	0.0005
-46.0	0.0286	0.0182	0.0097
-42.0	0.0052	0.0140	0.0003
-38.0	0.0181	0.0137	0.0011
-34.0	0.0614	0.0253	0.0032
-30.0	0.0514	0.0213	0.0021
-26.0	0.0225	0.0142	0.0008
-22.0	0.0496	0.0176	0.0021
-18.0	0.0318	0.0149	0.0014
-14.0	0.0641	0.0204	0.0039
-10.0	0.0497	0.0173	0.0034
-6.00	0.0388	0.0167	0.0013
-2.00	0.0584	0.0185	0.0021
2.000	0.0839	0.0224	0.0033
6.000	0.0518	0.0182	0.0047
10.00	0.0629	0.0200	0.0063
14.00	0.0716	0.0199	0.0033
18.00	0.1097	0.0257	0.0027
22.00	0.1482	0.0259	0.0041
26.00	0.1261	0.0251	0.0067
30.00	0.1610	0.0242	0.0066
34.00	0.1648	0.0260	0.0055
38.00	0.1636	0.0278	0.0064
42.00	0.2428	0.0320	0.0103
46.00	0.2912	0.0393	0.0173
50.00	0.3374	0.0375	0.0128
54.00	0.4634	0.0472	0.0135
58.00	0.5361	0.0539	0.0176
62.00	0.5040	0.0472	0.0279
66.00	0.6366	0.0561	0.0263
70.00	0.8127	0.0710	0.0459
74.00	0.7284	0.0659	0.0313
78.00	0.7202	0.0692	0.0289
82.00	0.0000	0.0000	0.0000
86.00	0.0000	0.0000	0.0000
90.00	0.0000	0.0000	0.0000
94.00	0.0000	0.0000	0.0000
98.00	0.0000	0.0000	0.0000
102.0	0.0000	0.0000	0.0000
106.0	0.0000	0.0000	0.0000
110.0	1.3992	0.1379	0.1062
114.0	1.3047	0.1430	0.1069
118.0	1.5827	0.1595	0.0559
122.0	1.4375	0.1480	0.0685
126.0	1.3142	0.1429	0.1314
130.0	0.7710	0.0995	0.1373
134.0	1.0794	0.1433	0.1063
138.0	0.9604	0.1549	0.0851
142.0	0.7663	0.1190	0.0555
146.0	1.0287	0.1507	0.1796
150.0	1.5495	0.2253	0.1189
154.0	1.2955	0.2376	0.5724
158.0	0.9786	0.2640	0.2432
162.0	0.7387	0.1783	0.0858
166.0	1.0623	0.5202	0.9010
170.0	0.4400	0.4218	0.8310
174.0	1.4755	0.5091	0.1655
178.0	0.8101	0.6703	0.5042
182.0	0.5911	0.8451	1.1040
186.0	0.6790	0.4109	0.2050
190.0	0.2408	0.3036	0.3022
194.0	0.3468	0.4105	0.2902
198.0	0.4235	0.3963	0.2496

Table E.3: The $^{58}\text{Ni}(\pi^-, K^+)$ inclusive spectrum as a table.

-B$_{\Sigma^-}$ (MeV)	Cross section (μb/sr/MeV)	Statistical errors	Systematic errors
-50.0	0.0402	0.0238	0.0006
-46.0	0.0464	0.0228	0.0005
-42.0	0.0327	0.0199	0.0009
-38.0	0.0322	0.0198	0.0004
-34.0	0.0425	0.0206	0.0005
-30.0	0.0648	0.0261	0.0007
-26.0	0.0651	0.0234	0.0007
-22.0	0.0437	0.0223	0.0006
-18.0	0.0471	0.0207	0.0006
-14.0	0.1035	0.0240	0.0017
-10.0	0.0726	0.0226	0.0009
-6.00	0.0824	0.0234	0.0010
-2.00	0.0924	0.0226	0.0012
2.000	0.0837	0.0225	0.0009
6.000	0.0722	0.0205	0.0009
10.00	0.1197	0.0238	0.0014
14.00	0.1442	0.0248	0.0016
18.00	0.1342	0.0240	0.0016
22.00	0.1588	0.0248	0.0016
26.00	0.2233	0.0283	0.0025
30.00	0.1985	0.0268	0.0021
34.00	0.2382	0.0292	0.0026
38.00	0.3454	0.0333	0.0041
42.00	0.3787	0.0347	0.0049
46.00	0.4000	0.0355	0.0047
50.00	0.4529	0.0383	0.0077
54.00	0.5349	0.0407	0.0099
58.00	0.6191	0.0441	0.0154
62.00	0.6318	0.0441	0.0181
66.00	0.7529	0.0496	0.0290
70.00	0.8350	0.0500	0.0355
74.00	0.8329	0.0522	0.0403
78.00	0.9241	0.0609	0.0556
82.00	1.1104	0.0599	0.0686
86.00	1.2185	0.0635	0.0821
90.00	1.2426	0.0753	0.0761
94.00	1.3347	0.0689	0.0654
98.00	1.4305	0.0841	0.1260
102.0	1.4465	0.0887	0.1298
106.0	1.3691	0.0923	0.1248
110.0	1.4438	0.0879	0.1044
114.0	1.4801	0.1038	0.1194
118.0	1.4224	0.0983	0.1876
122.0	1.3406	0.1075	0.1183
126.0	1.4306	0.1707	0.1561
130.0	1.3283	0.1895	0.1368
134.0	1.5228	0.1890	0.2007
138.0	1.3421	0.1820	0.2400
142.0	1.2459	0.1937	0.0881
146.0	1.1056	0.2547	0.2580
150.0	1.1761	0.3156	0.3438
154.0	1.2218	0.5745	0.4022
158.0	0.6356	0.3673	0.2316
162.0	0.9136	0.4570	0.1678
166.0	0.4536	0.4538	0.2631
170.0	0.9689	0.7014	0.2788

Table E.4: The ^{115}In(π^-, K^+) inclusive spectrum as a table.

-B$_{\Sigma^-}$ (MeV)	Cross section (μb/sr/MeV)	Statistical errors	Systematic errors
-50.0	0.0855	0.0353	0.0039
-46.0	0.0587	0.0281	0.0017
-42.0	0.0035	0.0143	0.0002
-38.0	0.0499	0.0248	0.0009
-34.0	0.0302	0.0226	0.0022
-30.0	0.0415	0.0202	0.0021
-26.0	0.0329	0.0194	0.0010
-22.0	0.0490	0.0216	0.0021
-18.0	0.0814	0.0258	0.0121
-14.0	0.0724	0.0233	0.0030
-10.0	0.0763	0.0233	0.0058
-6.00	0.0860	0.0234	0.0035
-2.00	0.0650	0.0224	0.0014
2.000	0.0865	0.0247	0.0109
6.000	0.0846	0.0224	0.0055
10.00	0.1312	0.0275	0.0176
14.00	0.1349	0.0235	0.0097
18.00	0.1546	0.0264	0.0168
22.00	0.1861	0.0258	0.0062
26.00	0.2204	0.0327	0.0097
30.00	0.2731	0.0356	0.0168
34.00	0.3003	0.0370	0.0062
38.00	0.3572	0.0412	0.0063
42.00	0.4032	0.0442	0.0213
46.00	0.3974	0.0416	0.0091
50.00	0.5141	0.0476	0.0212
54.00	0.6095	0.0521	0.0124
58.00	0.7018	0.0558	0.0187
62.00	0.6084	0.0516	0.0155
66.00	0.7704	0.0586	0.0261
70.00	0.8492	0.0645	0.0564
74.00	0.8939	0.0662	0.0524
78.00	0.9444	0.0669	0.0824
82.00	1.1461	0.0755	0.0635
86.00	1.2693	0.0829	0.1165
90.00	1.3236	0.0901	0.1501
94.00	1.3309	0.0924	0.1541
98.00	1.5872	0.1001	0.1706
102.0	1.6932	0.1170	0.1890
106.0	1.6785	0.1125	0.1613
110.0	1.7317	0.1204	0.1089
114.0	1.4510	0.1092	0.1941
118.0	1.8136	0.1322	0.1464
122.0	1.8225	0.1271	0.1276
126.0	1.7817	0.1504	0.1325
130.0	1.7700	0.1312	0.1613
134.0	1.4876	0.1593	0.3185
138.0	1.6231	0.1696	0.2132
142.0	1.8433	0.2599	0.2551
146.0	1.4337	0.2636	0.1433
150.0	1.1025	0.2401	0.4085
154.0	2.1866	0.5857	0.3323
158.0	1.4880	0.5633	0.2154
162.0	1.4392	0.7206	0.5350
166.0	3.8892	2.8229	0.9892
170.0	0.9020	0.2712	0.2883

Table E.5: The ^{209}Bi(π^-, K^+) inclusive spectrum as a table.

-B$_{\Sigma^-}$ (MeV)	Cross section (μb/sr/MeV)	Statistical errors	Systematic errors
-50.0	0.0317	0.0257	0.0318
-46.0	0.0692	0.0383	0.0120
-42.0	0.0440	0.0260	0.0010
-38.0	0.0262	0.0214	0.0005
-34.0	0.0409	0.0300	0.0002
-30.0	0.0353	0.0195	0.0009
-26.0	0.0817	0.0339	0.0017
-22.0	0.0511	0.0238	0.0129
-18.0	0.0733	0.0295	0.0011
-14.0	0.0787	0.0256	0.0021
-10.0	0.0696	0.0236	0.0291
-6.00	0.0899	0.0317	0.0154
-2.00	0.0698	0.0247	0.0032
2.000	0.0680	0.0243	0.0086
6.000	0.1402	0.0296	0.0030
10.00	0.1323	0.0283	0.0029
14.00	0.1472	0.0292	0.0108
18.00	0.1893	0.0325	0.0033
22.00	0.2246	0.0385	0.0187
26.00	0.2397	0.0381	0.0112
30.00	0.2858	0.0397	0.0050
34.00	0.3895	0.0473	0.0114
38.00	0.4681	0.0538	0.0214
42.00	0.4490	0.0521	0.0250
46.00	0.5479	0.0567	0.0312
50.00	0.5748	0.0595	0.0378
54.00	0.6558	0.0635	0.0258
58.00	0.6803	0.0660	0.0222
62.00	0.9564	0.0791	0.0756
66.00	0.9413	0.0802	0.1025
70.00	1.0287	0.0865	0.0360
74.00	1.0385	0.0868	0.0627
78.00	1.3791	0.1059	0.1103
82.00	1.3769	0.1088	0.1643
86.00	1.4988	0.1157	0.1420
90.00	1.7458	0.1318	0.2109
94.00	1.6178	0.1326	0.2023
98.00	2.1074	0.1728	0.2810
102.0	2.1719	0.1984	0.1371
106.0	2.1885	0.2283	0.3826
110.0	1.6772	0.1956	0.4280
114.0	2.1402	0.1992	0.2697
118.0	2.2187	0.2057	0.0944
122.0	2.1832	0.2111	0.1191
126.0	2.3295	0.2213	0.2073
130.0	2.1486	0.2420	0.4238
134.0	2.7211	0.2151	0.5652
138.0	1.9433	0.3171	0.4770
142.0	2.0725	0.3910	0.3771
146.0	2.0192	0.6665	0.4241
150.0	2.3897	0.8487	0.2567
154.0	1.8168	0.7440	1.4051

Bibliography

[1] T. Hasegawa, Doctor thesis, Univ. of Tokyo (1994)

[2] H. Hotchi, Doctor thesis, Univ. of Tokyo (2000)

[3] K. Tanida Doctor thesis, Univ. of Tokyo (2000)

[4] D.J. Millener, A. Gal and C. B. Dover,
Phys. Rev. C **38** (1998) 2700.

[5] S. Balberg, and A. Gal,
Nucl. Phys. **A 625** (1997) 435.

[6] M. Prakash and J. U. Lattiman
Nucl. Phys. **A 639** (1998) 433c.

[7] W. Brückner *et al.*, Phys. Lett. **79 B** (1978) 157.

[8] R. Bertini *et al.*, Phys. Lett. **83 B** (1979) 306.

[9] R. E. Chrien *et al.*, Phys. Lett. **89 B** (1979) 31.

[10] C. B. Dover and H. Feshbach, Ann. Phys. **198**, 321 (1990)

[11] R. Bertini *et al.*, Phys. Lett. **90 B** (1980) 375.

[12] H. Piekarz *et al.*, Phys. Lett. **110 B** (1982) 428.

[13] R. Bertini *et al.*, Phys. Lett. **136 B** (1984) 29.

[14] A. Gal and C.B. Dover, Phys. Rev. Lett. **47** (1980) 379.

[15] C.B. Dover, D.J. Millener and A. Gal , Physics Reports **184** (1989) 1.

[16] H. Bandō, T. Motoba and J. Žofka,
International Journal of Modern Physics , 5, (1990) 1.

[17] E. Oset *et al.* , Physics Reports **188** (1990) 79.

[18] R. Sawafta *et al.*, Nucl. Phys. **A585**, (1995) 103c.

[19] G. Backenstoss *et al.*, Z. Phys. **A273**, (1975) 137.

136

[20] C.J. Batty *et al.*, Phys. Lett. **74 B** (1978) 27.

[21] R.J. Powers *et al.*, Phys. Rev. **C 47** (1993) 1263.

[22] C. J. Batty, E. Friedman and A. Gal,
Prog. Theor. Phys. Suppl. **117**, 227 (1994)

[23] T. Harada, *Strangeness and Nucleus Workshop in Hakone* (1998)

[24] T. Yamada and Y. Yamamoto, Prog. Theor. Phys. Suppl. **117** (1994) 241.

[25] T. Nagae *et al.*, Phys. Rev. Lett. **80**, (1998) 1605.

[26] R. S. Hayano *et al.*, Phys. Lett. **231 B** (1989) 355.

[27] T. Harada *et al.*, Nucl. Phys. **A507**,(1990) 715.

[28] T. Yamazaki, R. Hayano, O. Morimatsu and K. Yazaki,
Phys. Lett. **207B** 393 (1988)

[29] M. Iwasaki, Doctor thesis, Univ. Tokyo (1987)

[30] H. Outa *et al.*, Prog. Theor. Phys. Suppl. **117** (1994) 117.

[31] T. Koike, private communication (1998)

[32] H. Noumi, KEK-PS Proposal **E438**, 1999.

[33] T. Yamazaki *et al.*, Phys. Lett. **207 B**, (1989) 112.

[34] S. Tadokoro and Y. Akaishi , Phys. Lett. **282 B**, (1992) 19.

[35] O. Morimatsu and K. Yazaki, Nucl. Phys. **A483**, (1988) 493.

[36] H. Bandō, T. Motoba and J. Žofka,
International Journal of Modern Physics A, **5**, (1990) 4032.

[37] T.Fukuda et al., Nucl. Instr. Meth. **A 361** (1995) 485.

[38] T.Shintomi et al., IEEE Trans. on Magnetics, Mag-**27** (1992) 585.

[39] T.Shintomi et al., IEEE Trans. on Magnetics, Mag-**28** (1992) 805.

[40] J.Myrhein and L.Bugge, Nucl. Instr. Meth. **160** (1979) 43.

[41] Praticle Data Booklet (2000)

[42] M. Nakamura, Master Thesis, Univ. of Tokyo (2001)

[43] CERN Program Library Entry W5013, GEANT

[44] M. L. Good and R. R. Kofler, Phys. Rev. **183**, 1148 (1969)

[45] H. Noumi, Private communication (2000)

[46] M. Akei *et al.*, Nucl. Phys. **A534**, (1991) 478.

[47] O. I. Dahl *et al.*, Phys. Rev. **163**, 1430 (1967)

[48] O. Goussu *et al.*, Nuovo Cimento **42**, A 606 (1966)

[49] H. Bandō, T. Motoba and J. Žofka,
International Journal of Modern Physics A, **5**, (1990)

[50] H. Noumi, Private communication (2001)

[51] T. Kobayshi, Master thesis, Univ. of Tokyo (1995)

[52] Y. Hamano, Master thesis, Univ. of Tokyo (1998)

[53] C. B. Dover, L. Ludeking and G. E. Walker,
Phys. Rev. C, **22**, 2073 (1980)

[54] H. DE. VRIES *et al.*, A.D.&N.D.T. **36**, 495 (1987)

[55] T. Motoba *et al.*, Phys. Rev. C **38**, 1322 (1988)